UNIVERSITÀ
degli STUDI
di CATANIA

Dipartimento
di Fisica
e Astronomia
"Ettore Majorana"

PhD programme in physics

Jinbiao Wei

Structure and cooling of (hybrid) neutron stars based on microscopic equations of state

---

PhD thesis

Supervisors:
Prof. V. Greco
Dr. G. F. Burgio
Dr. H.-J. Schulze

---

academic year 2020/2021

Contents

Abstract

Neutron stars (NSs) are the most compact objects in the Universe. The average mass of a NS is about 1.4 solar mass and its radius is about 10 km, hence the inner density can reach about 10 ρ_0, being ρ_0 the nuclear saturation density ($\rho_0 = 2.8 \times 10^{14}\,\mathrm{gcm}^{-3}$). This makes a NS the natural 'laboratory' for studying the four fundamental interactions, especially a unique environment for the study of the strongly interacting components at high densities. The equation of state (EOS) is a key ingredient in the NS study, however, it still suffers from the scarce knowledge of the strong interaction. This leads to the constructions of EOSs which are derived from different theoretical approaches, and being used to analyze many properties of NSs, e.g., the mass-radius relation, the moment of inertia and cooling properties in the evolutionary process. On the other hand, the observation of NSs allows us to constrain the EOS of the dense matter well beyond the densities available in earth laboratories. For example, observations of the NS mass, radius and the tidal deformability can be compared with the theoretical results, and from these the NS EOS can be inferred with some uncertainty. With this purpose, we employ the Brueckner-Hartree-Fock (BHF) theory for nuclear matter and two models (Field correlator and Dyson-Schwinger quark model) for quark matter, to study the properties of NSs, especially for the tidal deformability.

Besides the astrophysical observations, heavy-ion collisions could also give rise to certain constraints on nuclear-matter properties, for instance, the binding energy per baryon at saturation, the symmetry energy and the incompressibility. One may think that there are correlations between

constraints of nuclear matter properties and of a gravitational wave event. Based on this idea, we investigate properties of nuclear matter and examine possible correlations with NS observables for a set of microscopic nuclear EOSs derived within the BHF formalism employing compatible three-body forces. We find good candidates for a realistic nuclear EOS up to high density and confirm strong correlations between NS radius, tidal deformability, and the pressure of beta-stable matter. No correlations are found with the saturation properties of nuclear matter.

Another possible way that could be used in the study of dense matter properties is NS cooling. A NS is born hot ($\sim 10^{11}$ K) in a supernova explosion. Afterwards, it cools through three stages, i.e., thermal relaxation, neutrino cooling stage and photon cooling stage. Most NSs are supposed to be in the neutrino cooling stage since this stage lasts $\sim 10^5$ years. A simulation of NS cooling basically requires more quantities from the EOS, which we hope is able to reveal more facts about the dense matter. Therefore, we study the cooling of NSs and extend the work to the case of hybrid stars. We find that all BHF EOSs feature strong Direct Urca processes which lead to a too fast cooling. Accordingly, the pairing gaps, especially the proton 1S0 gap, are necessary and enough to describe well the current set of cooling data for isolated NSs. In all possible scenarios with and without quark matter, the possibility of a neutron 3P2 gap can be excluded.

Chapter 1

Introduction

1.1 What makes neutron stars so interesting?

A NS is one of the most compact objects in the Universe. In general, the typical mass of a NS is 1.4 solar mass with the radius about 10 km. This makes the mean density of NSs able to reach $2-3$ times saturation density ρ_0 ($= 3\times10^{14}\,\mathrm{gcm^{-3}} \sim 0.17\,\mathrm{fm^{-3}}$), while the average solar density is only about $1.4\,\mathrm{gcm^{-3}}$. At such high density, the matter turns out to be the strongly compressed nuclear matter or deconfined quark matter (or hyperonic matter) at even higher density in the core. These states of matter are currently impossible to reproduce in terrestrial laboratories, which means we have no method to study this dense matter in a experimental way. Furthermore, trying theoretical methods (for instance starting from a QCD calculation) to understand dense matter properties is also extremely difficult since the lack of a precise relativistic many-body theory of strongly interacting particles [1]. Although there are many difficulties in studying NSs, they are popular because of the extreme environments they present.

NSs possess enormous gravitational energy, $GM^2/R \approx 5\times10^{53}\,\mathrm{erg}$ [2], and one has to treat them as relativistic objects. Strong gravity makes the space-time curved within and around them. Accordingly, a spinning NS could be a kind of source of gravitational waves although the signal of a single NS is too dim to be observed. However, the NSs in a binary

NS system are able to emit a strong enough gravitational wave to be observed when they merge with each other. In August 2017, the first gravitational wave from a binary NS merger, GW170817, was detected by Ligo/Virgo [3, 4, 5]. More observations of gravitational waves from binary NSs are announced since the third observational run (O3) of the LIGO/Virgo Collaborations has started [6].

Weak interaction is another important interaction which has significant effects on NSs. They are born with $T \sim 10^{11}$ K from supernova explosions. Then, the stars cool down by emitting neutrinos and this process is going to last about 10^5 years before they enter a photon cooling era. As we know, the main engine of neutrino emission is baryon beta decay and inverse beta decay in the core. Currently, more NSs' surface temperatures can be measured although most cooling data has large uncertainty. A comparison can be make comparisons can be made between theoretical results (from cooling simulations) and observational data. This could be a useful tool to reveal the internal structure of NSs, which is also one important purpose to study the cooling evolution of NSs.

In addition, a NS may have a strong magnetic field on the surface, possibly inherited from the supernova. The surface magnetic field, $B \sim 10^8$ G, is a billion times stronger than the magnetic field surrounding the earth (~ 0.6 G). A magnetar has even more powerful magnetic fields of $\sim 10^{13}$ to 10^{15} G. The origin and evolution of NS magnetic fields is still a complicated problem that needs to be solved. One popular hypothesis suggested that the fields may be inherited from presupernova stars and amplified during the gravitational collapse owing to magnetic flux conservation [1]. Regarding the magnetars, the magnetic field could be simply inherited from stars with unusually high magnetic fields [7, 8]. The advantage of the strong magnetic field is that of making NSs able to be spotted in astronomical observations. In fact, NSs are sources of electromagnetic radiation in all wavelengths, from radio to hardest gamma rays, which show up in the observation as radio pulsar, X-ray pulsar, soft-gamma repeater and so on [2].

Due to the reasons stated, NSs have become good experimental "laboratories" for testing various theories, especially a unique environment for the study of the strongly interacting systems at high density, as we will study in this thesis.

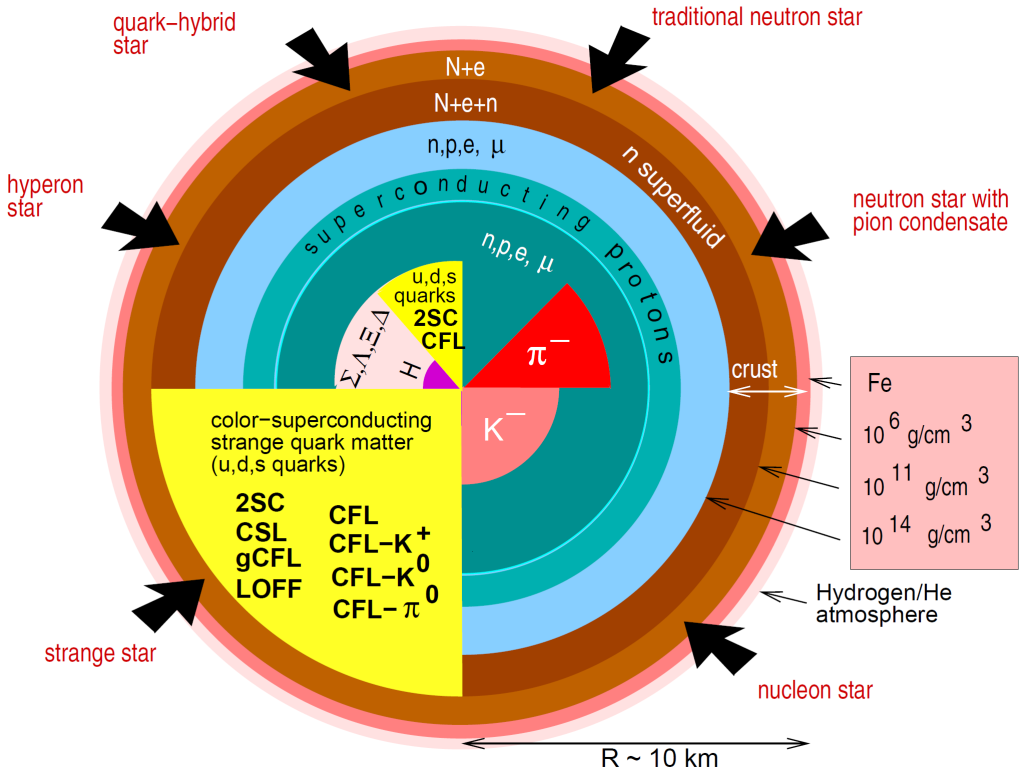

Figure 1.1: The structure of neutron stars and the theoretical predictions of the phases in the core, cited from Ref. [9].

1.2 Structure of neutron stars

A typical NS can be divided into four internal parts: the outer crust, inner crust, outer core and inner core. Otherwise, outside the NS, there is a surrounding atmosphere layer . A sketch of NS structure is shown in the Fig. 1.1.

The atmosphere is a plasma layer about 10 cm thickness. Its ingredients change if accretion happens. The atmosphere could be composed of hydrogen or helium as heavier elements (^{56}Fe) are expected to be destroyed if there is accretion after the NS formation, otherwise, heavy elements are expected [10, 11]. Compared to the internal parts, the contribution of the atmosphere to the mass and radius is completely negligible. However, it is the place where the spectrum of thermal electromagnetic NS radiation

is formed. The spectrum, beaming and polarization of emerging radiation can be determined theoretically by solving the radiation transfer problem in atmospheric layers [1], which is upmost important for the interpretation of X-ray observations. For example, through the analysis of the X-ray spectra of quiescent low-mass X-ray binaries hosted in globular clusters, one could estimate the possible range of the NS radius, $R_{\rm NS} = 9 - 11\,{\rm km}$ [12, 13, 14, 15]. Besides, the radiation from the atmosphere also contains valuable information on the NS masses and the parameters of the surface layer including effective surface temperature, surface gravity, chemical composition, strength and geometry of the surface magnetic field.

The outer crust is the layer with the density range from $10^4\,{\rm gcm}^{-3}$ to neutron drip density $\rho_d \approx 4\times10^{11}\,{\rm gcm}^{-3}$. Its depth is about several hundreds meters. At very low density, Fe nuclei arranged in a lattice is the ground state of matter and thus a iron envelope is formed at the bottom of the atmosphere. As the density increases, the electron Fermi energy increases. At $\rho \gtrsim 8\times10^6\,{\rm gcm}^{-3}$, electrons are energetic enough to be captured by Fe nuclei and then produce neutrinos [16]. This induces that the energy can be lowered by the neutrino emission which makes Fe no longer the ground state. The capture of electrons makes nuclei become more neutron-rich, and eventually at the bottom of the outer crust ($\rho \approx 4\times10^{11}\,{\rm gcm}^{-3}$) the neutrons start to drip out of the nuclei and form a free neutron gas.

The inner crust is thicker than the outer crust, and has a depth of several kilometers. Its density ranges from $\rho = \rho_d$ to about $\rho = 0.5\rho_0$. Besides the neutron-rich nuclei and degenerate electrons, one new ingredient appearing in this layer is the free neutron. As more neutrons drip out from the nuclei, they may form a so-called superfluid.

The outer core and crust are separated by a layer of density $\rho \sim 0.5\rho_0$ where the nuclei entirely melt into neutrons and protons. Accordingly the main difference between core and crust is that nuclei are no longer present in the core. Core matter is comprised of neutrons, protons, electrons and more massive leptons (muons) as the density continues to increase. A superfluid of protons is also supposed to appear in the core. Superfluidity is a phenomenon occurring on the Fermi surface; the order of the corresponding pairing gaps is about several MeV [17], which causes only a slightly effect on the EOS and thus on the mass and radius of NSs.

However, the superfluidity is important for the NS cooling evolution. It can suppress the neutrino emission from the core, for example, the fast neutrino reaction - direct Urca process - can be strongly suppressed by superfluidity of either neutrons or protons [18]. On the other hand, the superfluidity opens new channels for neutrino emission - Cooper pair breaking and formation processes.

The inner core is a region with the density $\rho \gtrsim 2\rho_0$, which is not able to be created at terrestrial laboratories. Its central density can be as high as $10 - 20\rho_0$ [1] and thus provides a high-pressure environment in the core. In such an extreme environment, numerous subatomic particle processes are possible, from the generation of hyperons and baryon resonances ($\Sigma, \Lambda, \Xi, \Delta$) to quark ($u, d, s$) deconfinement to the formation of boson condensates (π^-, K^-, H-matter) [9], which leads to many conjectures about the compositions inside the core. As shown in Fig. 1.1, the main hypotheses are [1, 9, 19]:

i) Firstly, the state of matter in the inner core remains unchanged but contains higher fractions of proton and leptons (e, μ). This triggers a fast neutrino reaction - the Direct Urca process, and causes a very fast cooling of NSs [20, 21].

ii) A hyperon core could appear in the central region. At high density the neutron with large chemical potential μ_n can decay via the weak interactions into Λ hyperons and form a new Fermi sea for this hadronic species with $\mu_\Lambda = \mu_n$ [22]. Other hyperons (for instance Σ) can be formed with similar weak processes. However, the presence of hyperons reduces the system pressure and makes it difficult to achieve $\sim 2M_\odot$ of resulting NSs. This is the so-called "hyperon puzzle" [22, 23, 24]. One straightforward solution is making the hyperonic EOS stiff, i.e., increase the pressure of the hyperon core. With this purpose, the authors of Refs. [25, 26, 27, 28] employed a multi-pomeron-exchange potential model to introduce a universal three-body repulsion in the hyperonic matter. They showed that the hyperonic EOSs can reach a maximum mass which is compatible with the largest currently measured ($\sim 2M_\odot$) NS masses, however, with a higher density threshold for appearance of hyperons. A similar method to introduce an additional repulsion among hyperon by including the vector ϕ meson is proposed in the relativistic mean field (RMF) method [29, 30]. Accordingly, the NS with hyperon core is able to achieve $\sim 2M_\odot$.

iii) The appearance of π condensation was firstly proposed by Bahcall and Wolf [31]. The condensates soften the EOS and thus reduce the maximum mass [20]. In the meanwhile, a new reaction of direct Urca is allowed by pion condensation.

iv) The fourth hypothesis, proposed by Kaplan and Nelson [32], assumes K^- condensation could appear in the NS. Because of the nonzero mass ($\sim 150\,\mathrm{MeV}$) of strange quarks, strange particles are not supposed to be present at low density. When the density is high enough to make the chemical potential of a strange quark greater than its mass, strange particles are possible to appear. In the normal state, there is a possibility of Λ and Σ^- being present [33]. However, as suggested by Kaplan and Nelson, the energy of K^- could be lowered by the interaction with nucleons, therefore favoring K^- condensation in the core.

v) Deconfined quark matter may appear in the center of heavy NSs since the central particle density could reach values larger than $1\,\mathrm{fm}^{-3}$, where in fact quark degrees of freedom are expected to appear at a macroscopic level. This possibility has been extensively studied in many publications, e.g., [9, 34, 35, 36, 37]. According to the analysis of observational data from the NS EXO 0748–676, Özel concluded that quark matter probably does not exist in the centre of NSs [38]. However, as suggested in Ref. [39], this conclusion is based on a limited set of possible equations of state for quark matter. Thus, the authors considered a more comprehensive set of proposed quark matter equations of state from the literature, and concluded that the presence of quark matter in EXO 0748–676 is not ruled out [39]. Another recent study shows the evidence of quark matter appearing in the core of massive NS [40]. In principal, only the light quarks are supposed to appear in the core, while heavy quarks are difficult to form because of their large effective masses.

Moreover, the presence of deconfined quark matter could be another possible solution of the "hyperon puzzle" as suggested in Ref. [41]. However, this requires a early phase transition preventing the presence of hyperons, and in particular a sufficiently stiff quark matter EOS which allows a NS mass $\gtrsim 2M_\odot$. A successful model has been discussed in [42, 43], where the authors considered the lowest-order constrained variational method for hadronic matter and described the quark matter by a nonlocal Nambu-Jona-Lasinio model. The vector interactions are in-

cluded in quark matter so as to stiffen the EOS. As shown in [42, 43, 44], the stiff quark-matter EOS eases the request on the onset of a phase transition to quark matter. It could even happen with hyperons present, which means the NS can be made of hypernuclear matter in the outer core and quark matter in the inner core.

One special kind of star, the so-called strange quark star, is completely comprised of deconfined quark matter covered with a thin iron envelope or without any envelope. The idea originated from Witten's hypothesis that strange quark matter is the true ground state of QCD [45]. Therefore, strange quark matter can be more stable than hadronic matter and thus the entire star will convert to strange quark matter eventually. So far, there is no evidence from observation that strange quark stars exist, while there is also no evidence that could rule out this possibility. It is difficult to distinguish wether a pulsar is a NS or a quark star with iron envelope because they have similar properties (radius, mass and surface magnetic field) [34]. Since quark matter is more dense, strange quark stars have smaller radii than normal NSs with the same gravitational mass, especially the bare quark stars which have no crust structure. If, in the future, a NS with small radius ($\lesssim 10\,\mathrm{km}$) is observed, it could be a (bare) strange quark star.

1.3 Astrophysical observations

In 1934, Baade and Zwicky proposed that NSs are formed in the center of a supernova explosion. Then, Oppenheimer and Volkov assumed that a NS is composed of a high-density ideal neutron gas, and obtained its structural Tolman-Oppenheimer-Volkoff (TOV) equation. But it was neglected by scientists for the next 30 years. The reason is simply the limitation of observational technique. It is difficult to find such celestial bodies whose radii are only around 10 km and meanwhile the nearest one is at least a few dozen light years away. Therefore, the only available optical method to discover NSs at that time, was obviously doomed to failure.

In astronomical observations, NSs are detected as pulsars, which is, NSs with a stable rotating speed. The first pulsar was discovered by Jo-

celyn Bell on August 6, 1967, named PSR B1919+21.2. She found a weak variable radio source but with strictly periodic pulses. The pulse period, 1.3373012s, was accurately measured after four months of its finding and turned out to be wonderfully stable [1]. Gold [46] suggested that the pulsar was a rotating magnetized NS and it turned out that his idea is true. This is already about thirty years after physicists theoretically predicted the existence of such stars.

With the development of observational technique, it has become possible to detect NSs. More than 2800 pulsars have been observed so far [47]. NSs are emitters of electromagnetic emission in all wavelengths, from radio to gamma rays. Thus, pulsars can be characterized by the spectral range where pulsations are observed, for example, the first observed pulsar was a radio pulsar which emitted radio waves. Among the pulsars observed, the most are in fact the radio pulsars ($\sim$ 2700). Since the radio wave has large wavelength and is able to pass through the atmosphere of earth, the observations are conducted with ground-based telescopes such as the Arecibo Radio Telescope, the Five-hundred-meter Aperture Spherical radio Telescope (FAST) and the world's largest and most capable radio telescope (under construction)- the Square Kilometre Array (SKA).

X-rays and gamma-rays are easily absorbed by the atmosphere, thus their observations have to rely on space telescopes. This is more difficult than the detection of radio pulsars, which is also the reason why there are less X-ray/gamma-ray pulsars observed so far. There are already some well-known space observatories such as the Chandra X-ray Observatory (CXO), the XXM-Newtonian satellites, the Athena X-ray Observatory and the Fermi Gamma-ray Space Telescope for the detection of gamma-rays from outer space. With the improvement of technique, more pulsars could be observed, especially when the FAST, SKA and Athena X-ray Observatory will be fully operational. This, accordingly, will cause great progress in understanding NSs, e.g. their mass, radius, frequency and so on.

1.3.1 Frequency

Compared to the other properties of a NS, its rotational frequency is easy to be observed. Based on the frequency (period), pulsars can be divided

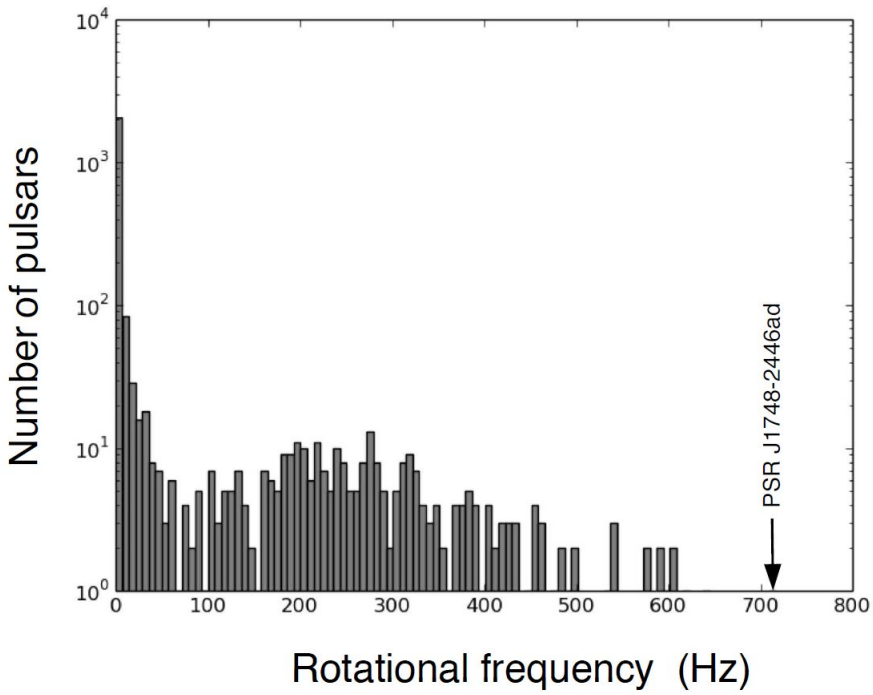

Figure 1.2: Distribution of frequency for 2510 pulsars (from Ref. [48]). All information of pulsars could be found in the Australia Telescope National Facility Pulsar Catalog [47].

into ordinary pulsars, whose rotational period is of the order of a few seconds, and millisecond pulsars, whose rotation period is $p \lesssim 30\,\text{ms}$. A histogram of the rotational frequency of observed pulsars is shown in Fig. 1.2. As shown, most pulsars ($\sim 90\%$) have a low frequency, especially the range of $0 - 10\,\text{Hz}$ with over 2000 pulsars. Currently, the fastest spinning pulsar J1748-2446ad, observed by Hessels on November 10 of 2004, has a frequency of 716 Hz (period of 1.4ms) [49]. It is possible that NSs possess even higher frequency (for instance 1000 Hz) due to their extremely strong gravity. It had been claimed that XTE J1739-285 is the fastest spinning pulsar with the frequency $f = 1122\,\text{Hz}$ [50]. However, this is under doubt since this result could not be reproduced.

1.3.2 Luminosity

The luminosity of NSs, which could be observed, is basically the photon luminosity since the neutrino luminosity is difficult to be detected directly. However, it is difficult to get accurate results of photon luminosities. The data is usually with large error bars caused by the unknown composition of the NS atmosphere, the distance or interstellar absorption. Hence, the same object analysed by different model, e.g., the black body model and H atmosphere model, could have different result varying by a factor of a few [51, 52, 53]. Even so, these data are still important, especially the thermal luminosity of isolated NSs, which could put constraints on the theoretical study of NS cooling. Of course, for that also the ages of NSs need to be known. They can be extracted from the spin period and its time derivative, which determine the characteristic age $t_c = P/2\dot{P}$ [54], or from kinetic properties of the stars (proper motion for instance), that are the kinetic ages $t_{\rm kin}$. As in Ref. [55], the kinetic ages are favoured where possible, and characteristic ages, in most cases, are treated as upper limits. In Table. 1.1 we present the recent collection of cooling data [53], where the characteristic ages t_c, the kinetic ages $t_{\rm kin}$, the redshifted bolometric luminosities L^{∞} and redshifted surface temperatures T^{∞} of 55 NSs are given.

The descriptions of each object listed in the table are shown in Ref. [53]. We just remind here two most extreme objects, XMMU J1731-347 and CXOU J2332327.8+584842 (Cas A NS). XMMU J1731-347 is a compact thermal x-ray source in supernova remnant with a extremely high luminosity, and is indeed supposed to have a carbon atmosphere [51, 56, 57, 58]. Cas A NS is a central compact object in the supernova remnant Cas A. It is a very young NS with $t_{\rm kin} \sim 300$ yr. According to Ref. [10, 59, 60] Cas A experienced a rapid temperature decrease by $\sim 4-5\%$ over 8 years (from 2010 to 2018), which could impose strong constraints on NS cooling. This has been studied in detailed in many publications,.e.g., Refs. [61, 62, 63, 64, 65]. However, Posselt & Pavlov [66, 67] suggested that this rapid cooling caused by instrument effect. They employed a different instrument setup (Chandra ACIS subarray mode) and did not find a statistically significant temperature decrease[67]. This difference has not been explained so far.

Recently the Atacama Large Millimeter Array (ALAM) radio telescope found a the red blob in the remnant of SN1987 which has high possibility to be a NS (NS 1987A). If correct, this NS would be the youngest star observed with 33 years. This provides an unprecedented opportunity to follow its early evolution, especially for the NS cooling behaviour at early stage [68, 69].

Table 1.1: The ages, thermal luminosity and effective temperatures for several isolated NSs. From Ref. [53].

Name	t_c(kyr)	$t_{\rm kin}$(kyr)	$L^\infty(10^{32}\,{\rm erg\,s^{-1}})$	k_BT^∞(eV)
I. Weakly magnetized thermal emitters				
1E 0102.2-7219	-	2.1 ± 0.6	110^{+160}_{-50}	210^{+40}_{-30}
RX J0822.0-4300	2.54×10^5	4.45 ± 0.75	50 ± 11	$276 \pm 15/455 \pm 20$
CXOU J085201.4-461753	-	$2.1 - 5.4$	20 ± 10	90 ± 10
2XMM J104608.7-594306	-	$11 - 30$	$0.8 - 6$	$40 - 70$
1E 1207.4-5209	3.01×10^5	7^{14}_{-5}	$13.1^{+4.9}_{-1.6}$	$90 - 250$
1RXS J141256.0+792204	285	-	$2 - 50$	$65 - 210$
CXOU J160103.1-513353	-	0.8 ± 0.2	58 ± 2	118 ± 1
1WGA J1713.4-3949	-	1.608	$\sim 20 - 120$	138 ± 1
XMMU J172054.5-372652	-	$0.6 - 1.2$	$150 - 270$	161 ± 9
XMMU J1731-347	-	$2 - 6$	174^{+19}_{-39}	153^{+4}_{-2}
CXOU J181852.0-150213	-	$3.4^{+2.6}_{-0.7}$	84^{+68}_{-42}	130 ± 20
CXOU J185238.6+004020	1.92×10^5	$6.0^{+1.8}_{-2.8}$	104^{+24}_{-20}	133 ± 1
CXOU J232327.8+584842	-	$0.320 - 0.338$	$61 - 94$	$123 - 185$
II. Ordinary pulsars				
PSR J0205+6449	5.37	0.819	$1.9^{+1.5}_{-1.1}$	49^{+5}_{-6}
PSR J0357+3205	541	$200 - 1300$	$0.15^{+0.25}_{-0.11}$	36^{+9}_{-6}
PSR J0538+2817	620	40 ± 20	$10.9^{+2.7}_{-4.6}$	91 ± 5
CXOU J061705.3+222127	$10 - 100$	~ 30	2.6 ± 0.1	$58.4^{+0.6}_{-0.4}$
PSR J0633+0632	59.2	-	$1.5^{+2.5}_{-0.9}$	53 ± 4
PSR J0633+1746	342	-	$0.88^{+2.1}_{-0.39}$	42 ± 2
PSR B0656+14	111	-	$6.7^{+2.1}_{-1.5}$	$64 \pm 4/123^{+6}_{-5}$
PSR B0833-45	11.3	$17 - 23$	4.24 ± 0.12	57^{+3}_{-1}
PSR B1055-52	535	-	$1.0^{+1.0}_{-0.7}$	68 ± 3
PSR J1357-6429	7.31	-	3.6 ± 0.7	64 ± 4
PSR B1706-44	17.5	-	$7.1^{+1.6}_{-6.5}$	71^{+140}_{-30}
PSR J1740+1000	114	-	$1.9^{+3.1}_{-1.0}$	67 ± 11
PSR J1741-2054	386	-	$3.1^{+1.4}_{-1.0}$	60 ± 2

Table 1.1: continued

Name	t_c(kyr)	$t_{\rm kin}$(kyr)	$L^{\infty}(10^{32}$ erg s$^{-1})$	k_BT^{∞}(eV)
PSR B1822-09	233	-	$0.26^{+0.12}_{-0.09}$	83 ± 4
PSR B1823-13	21.4	-	4.5 ± 0.9	97^{+4}_{-5}
PSR J1836+5925	1.83[3]	-	$0.014^{+0.016}_{-0.006}$	$15.9^{+3.3}_{-2.2}$
PSR B1951+32	107	64 ± 18	$1.8^{+3.0}_{-1.1}$	130 ± 20
PSR J1957+5033	870	-	$0.012 - 0.11$	$\sim 13 - 25$
PSR J2021+3651	17.2	-	5^{+3}_{-2}	63^{+6}_{-3}
PSR B2334+61	40.6	~ 7.7	0.47 ± 0.35	38^{+6}_{-9}
		III. High-B pulsars		
PSR J0726-2612	186	-	$4.0^{+4.4}_{-1.0}$	74^{+6}_{-11}
PSR J1119-6127	1.61	4.2 – 7.1	19^{+19}_{-8}	$\sim 80 - 210$
PSR B1509-58	1.56	-	90 ± 20	142^{+7}_{-9}
PSR J1718-3718	33.2	-	4^{+5}_{-2}	$57 - 200$
PSR J1819-1458	120	-	30^{+50}_{-22}	138^{+3}_{-25}
		IV. The Magnificent Seven		
RX J0420.0-5022	1.98×10^3	-	0.06 ± 0.02	45.0 ± 2.6
RX J0720.4-3125	1.90×10^3	850 ± 150	$1.9^{+1.3}_{-0.8}$	$90 - 100$
RX J0806.4-4123	3.24×10^3	-	$0.16 - 0.25$	$\sim 90 - 100$
RX J1308.6+2127	1.46×10^3	550 ± 250	$3.3^{+0.5}_{-0.7}$	$\sim 50 - 90$
RX J1605.3+3249	-	440^{+70}_{-60}	$0.07 - 5$	$35 - 120$
RX J1856.5-3754	3.76×10^3	420 ± 80	$0.5 - 0.8$	$36 - 63$
RX J2143.0+0654	3.7×10^3	-	$0.5 - 1.7$	40/100
		V. Upper limits		
PSR J0007+7303	13.9	≈ 9.2	< 0.3	< 200
PSR B0531+21	1.26	0.954	< 300	< 180
PSR B1727-47	80.5	50 ± 10	< 0.35	< 33
PSR J2043+2740	1.20×10^3	-	< 0.4	< 80
PSR B2224+65	1.13×10^3	-	< 1.7	< 110
		VI. Hot spots		
PSR B0114+58	275	-	0.044 ± 0.003	170 ± 20
PSR B0943+10	4.98×10^3	-	$0.001 - 0.005$	$82^{+3}_{-9} - (\sim 220)$
PSR B1133+16	5.04×10^3	-	$0.0003^{+0.0017}_{-0.0002}$	190^{+40}_{-30}
PSR J1154-6250	7.99×10^3	-	0.017 ± 0.05	210 ± 40
PSR B1929+10	3.11×10^3	-	$0.0084^{+0.0034}_{-0.0022}$	300^{+20}_{-30}

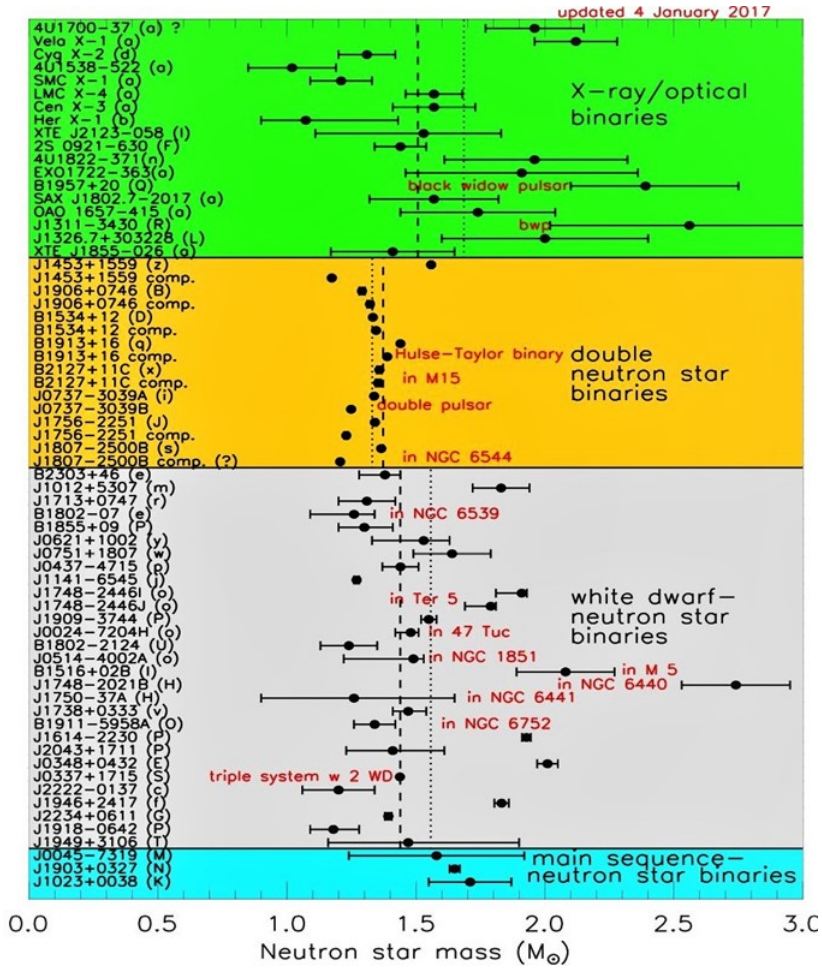

Figure 1.3: Masses measured from pulsar timing. From Ref. [70].

1.3.3 Mass measurements

The precise measurement of a NS mass could be performed using timing of radio pulsars located in binary systems. All current methods rely on precise tracking of orbital motions through the arrival times of the observed pulsations, and allow extremely precise mass measurements [15]. As an example, the mass of the pulsar PSR J1829+2456 was measured to be $1.295 \pm 0.011 M_{\odot}$ with 95% confidence [71].

In a binary system, orbital motions can be described by the Keplerian parameters: the binary orbital period P_b, the projection of the semi-major

axis onto observer's line of sight $x_{\rm PSR} = a_{\rm PSR}\sin i/c$ (where $a_{\rm PSR}$ is the semi-major axis, i is the angle between the orbital plane and observer's line of sight), the eccentricity e, and the time and longitude of periastron, T_0 and ω_0. These parameters are related to the pulsar and companion masses, $M_{\rm PSR}$ and $M_{\rm c}$, through the binary mass function

$$f \equiv \frac{M_c \sin i^3}{{M_T}^2} = \frac{4\pi^2}{T_\odot}\frac{x_{\rm PSR}^3}{P_b^2}, \tag{1.1}$$

where $M_T = M_{\rm PSR} + M_c$ is total mass of the binary system, and the constant $T_\odot = GM_\odot/c^3 = 4.925490947\ \mu s$. Clearly, only Eq. 1.1, which has three unknowns quantities ($i, M_{\rm PSR}$ and M_c), is not enough to determine the masses in the binary system; one needs more information from pulsars. If the observations of pulsar timing (arrival time of pulses) are accurate enough, the measurements of post-Keplerian (PK) parameters, that are, the rate of advance of periastron $\dot{\omega}$, the "Einstein delay" γ, the orbital period decay $\dot{P}_b$ and the range r and the shape s of Shapiro delay, will be allowed. In general relativity, the expressions of the PK parameters are given by [72]

$$\dot{\omega} = 3(\frac{P_b}{2\pi})^{-5/3}(T_\odot M_T)^{2/3}(1-e^2)^{-1}, \tag{1.2}$$

$$\gamma = e(\frac{P_b}{2\pi})^{1/3}{T_\odot}^{2/3}M_T^{-4/3}M_c(M_{\rm PSR}+2M_c), \tag{1.3}$$

$$\dot{P}_b = -\frac{192\pi}{5}(\frac{P_b}{2\pi T_\odot})^{-5/3}(1+\frac{73}{24}e^2+\frac{37}{96}e^4) \times (1-e^2)^{17/2}M_{\rm PSR}M_{\rm c}M_T^{-1/3}, \tag{1.4}$$

$$r = T_\odot M_{\rm c} \tag{1.5}$$

$$s = \sin i = x_{\rm PSR}(\frac{P_b}{2\pi})^{-2/3}T_\odot^{-1/3}M_T^{2/3}M_c^{-1}. \tag{1.6}$$

Thus, combining Eq. 1.1 with any pair of PK parameters could be sufficient to determine the masses of pulsar and companion. As an example, the pulsar PSR J1614-2230 shows a strong Shapiro delay signature and its orbital period and projected semi-major axis are observable, which are $P_b = 8.6866194196(2)$ days and $x_{\rm PSR} = 11.2911975(2)$ light-seconds, respectively. With two additional PK parameters obtained from Shapiro delay,

$s = 0.999894(5)$ and $r/T_\odot = 0.500(6)M_\odot$, the mass of PSR J1614-2230 was calculated to be $1.97 \pm 0.04 M_\odot$, which has only a $\sim 2\%$ error [73].

Fig. 1.3 shows the measured masses of pulsars in different binary systems. The mass measurement in a double NSs binary system may achieve extremely high precision. The masses of NSs distribute over a wide range from $1.17M_\odot$ to $2M_\odot$, although the majority of NSs have a mass $\sim 1.4M_\odot$. The recently observed most massive pulsar J0740+6620 with $M = 2.14^{+0.10}_{-0.09} M_\odot$ [74], which is not yet included in the figure, is slightly heavier than J0348+0432 ($M = 2.01 \pm 0.04 M_\odot$) [75]. The result of J1748-2021B with the mass $M = 2.74 \pm 0.21 M_\odot$ (1σ confidence) [76] is under debate, accordingly one still considers J0740+6620 as the observed most massive NS, which imposes a lower limit on the maximum mass of NSs. Note also that the source of GW190814 has a companion which is supposed to be a black hole or a NS with mass $M = 2.59^{+0.08}_{-0.09} M_\odot$ [77]. There is hardly any realistic EOS that could give static TOV masses of about $2.6M_\odot$ if the companion star is a NS. One possible case suggested in several works [78, 79, 80] is that that object could be a leftover of an extremely fast rotating NS as the fast (Keplerian) rotation increases the maximum mass by about 20% [81, 82].

The masses of isolated NSs, which account for 90% of the known NSs, are currently unable to be observed, since all methods rely on the binary system.

1.3.4 Radius measurements

Radius measurements are more difficult than the one of masses. Nearly all methods that are currently used rely on the detection of thermal emission from the surface of the star either to measure its apparent angular size or detect the effects of NS spacetime on this emission to extract the radius information [15]. And thus the major approaches can be divided into spectroscopic and timing measurements.

The spectroscopic measurements of radius rely on detecting the angular size of the NS,

$$\frac{R_{\rm obs}}{D} = \left(\frac{F_{\rm bol}}{\sigma_B T_{\rm eff}^4}\right)^2, \tag{1.7}$$

where $R_{\rm obs}$ is the observed radius, D is the distance between the source

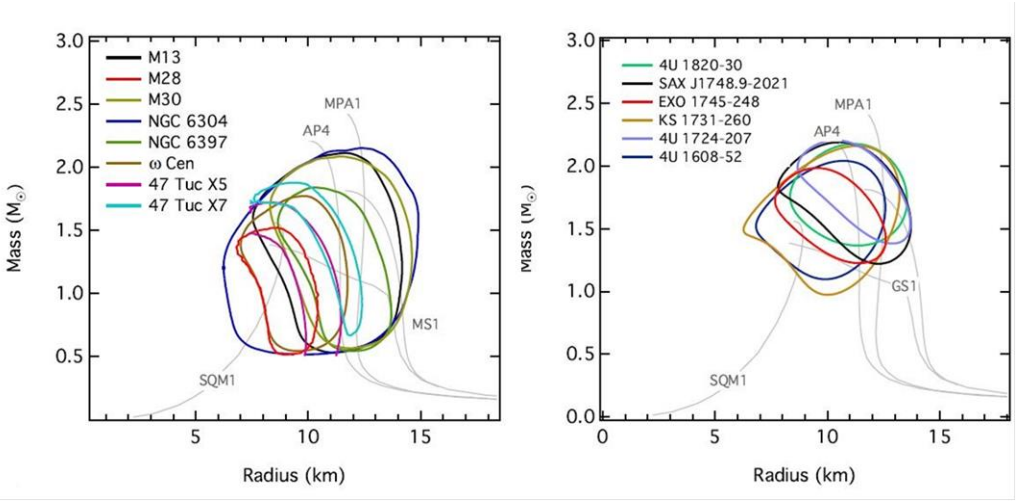

Figure 1.4: The combined constraints at the 66% confidence level on the NS mass and radius obtained from all NSs in low-mass X-ray binaries during quiescence (Left) and all NSs with thermonuclear bursts (Right). From Ref. [15].

and the observer, σ_B is the Stefan-Boltzmann constant, and the bolometric flux $F_{\rm bol}$ and effective temperature $T_{\rm eff}$ can be determined through analysis of the spectra. Since this approach relies on the detection of flux and effective temperature, the same factor could affect the precision of radius measurement, including the composition of atmosphere, the strength of the magnetic field, the distance, no-thermal component and the interstellar absorption. For isolated NSs, these quantities are extremely difficult to determine accurately. Accordingly, radius measurements of isolated NS suffer from a large uncertainty.

Quiescent X-ray transients in low-mass X-ray binaries (QLMXBs) are promising sources for radius determinations. Because in the quiescent phase the accretion of matter from the companion is ceased or strongly reduced and the observations of thermal emission from the stellar surface become possible. Furthermore, the atmosphere is likely to be composed of light elements (H or He) and the magnetic field is low due to the accretion of matter. Regarding the distance D, it could be well known if the objects are located in globular clusters. Fig. 1.4 shows the possible ranges of NS radii by analyzing the spectra of several QLMXBs. The error

of radii is mass-dependent, which arises from $R_{\rm obs} = \sqrt{(1-2GM/R)}R$. Based on the same data, Guillot suggested a small radius of NSs, $R = 9.4 \pm 1.2$km [12, 13].

A phenomenon in LMXBs could be used to determine the radius, which is the so-called thermonuclear X-ray burst. Two observables related to bursts are the apparent surface area A and the Eddington flux $F_{\rm edd}$, defined as

$$A = \frac{R^2}{D^2 f_c^4}(1-\frac{2GM}{R})^{-1}, \tag{1.8}$$

$$F_{\rm edd} = \frac{GM}{k_{\rm es}D^2}(1-\frac{2GM}{R})^{\frac{1}{2}}, \tag{1.9}$$

where $k_{\rm es}$ is the electron scattering opacity in the stellar atmosphere and f_c is the color correction factor that takes into account the distortions in the spectrum due to the stellar atmosphere. A detailed description of these parameters is given in Ref. [83]. Remind that the Eddington flux is evaluated when the photosphere touches the stellar surface. This approach has been applied to several NSs in LMXBs, and the results are shown in the right panel of Fig. 1.4. These results indicate a common range of about $9-11$ km, which is consistent with the results obtained from the analyses of QLMXBs.

Timing measurement (modeling pulse profile) is usually applied to the rotation-powered millisecond pulsars (MSP). The amplitudes and shapes of the pulsations are determined by both the brightness contours on the stellar surface and the degree of strong-field gravitational lensing that photons experience on their paths to the distant observer [84]. Therefore, modeling the pulse profile can probe the stellar spacetime and thus determine the mass and radius. The Neutron Star Interior Composition Explorer (NICER) is able to observe the X-ray pulsation from MSP. Confident observations of X-ray pulsations for 5 MSP observed by NICER are reported in Ref. [85]. In addition, the mass and radius of the pulsar PSR J0030+0451 $M = 1.44^{+0.15}_{-0.14}M_\odot$ and $R = 13.02^{+1.24}_{-1.06}$ km [86], or $M = 1.36^{+0.15}_{-0.16}M_\odot$ and $R = 12.71^{+1.14}_{-1.19}$ km [87], are obtained.

The measurements of radius have progressed with the improvement of techniques. For example, the NICER , ATHENA+ and the Large Observa-

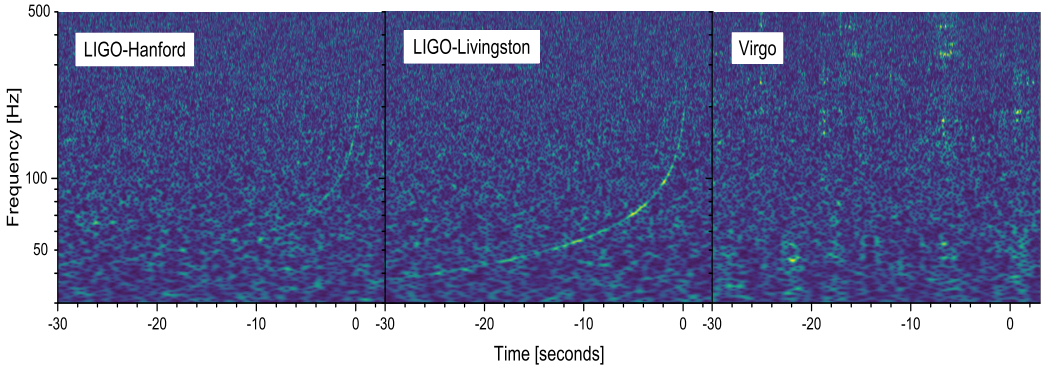

Figure 1.5: Signal of the gravitational-wave event GW170817 from the binary NS spiral, observed by the LIGO-Hanford (left), LIGO-Livingston (middle), and Virgo (right) detectors. Times are shown relative to August 17, 2017 12:41:04 UTC. From Ref. [88].

tory for X-ray Timing (LOFT) high-precision detectors narrow down the possible range of NS radius. Additionally, the detectable gravitational-wave signals from binary NS mergers put a new constraint on the radius. However, the precision of radius measurements is still not high enough and unable to impose a stringent limit on the structure of NSs and thus the EOS inside the core of NSs.

1.3.5 Multimessenger era

On 17th August 2017, the first gravitational wave emitted by a binary NS merger was detected by the Ligo and Virgo observatories. This observation is so special although it is not the first time that gravitational wave effects were observed. The former observations are usually originating from black holes mergers, which are dark and have no electromagnetic counterparts that can be detected. Unlike a binary black hole, the NS merger simultaneously emits gravitational waves and electromagnetic waves, from gamma-ray, X-ray, optical, infrared, to radio, and neutrinos. It is like a candle in the dark which can be seen by many detectors in different bands. Accordingly, the binary NS event GW170817 initiates the multimessenger era which means the study of one object through the various messages and bands by different observations from the same source.

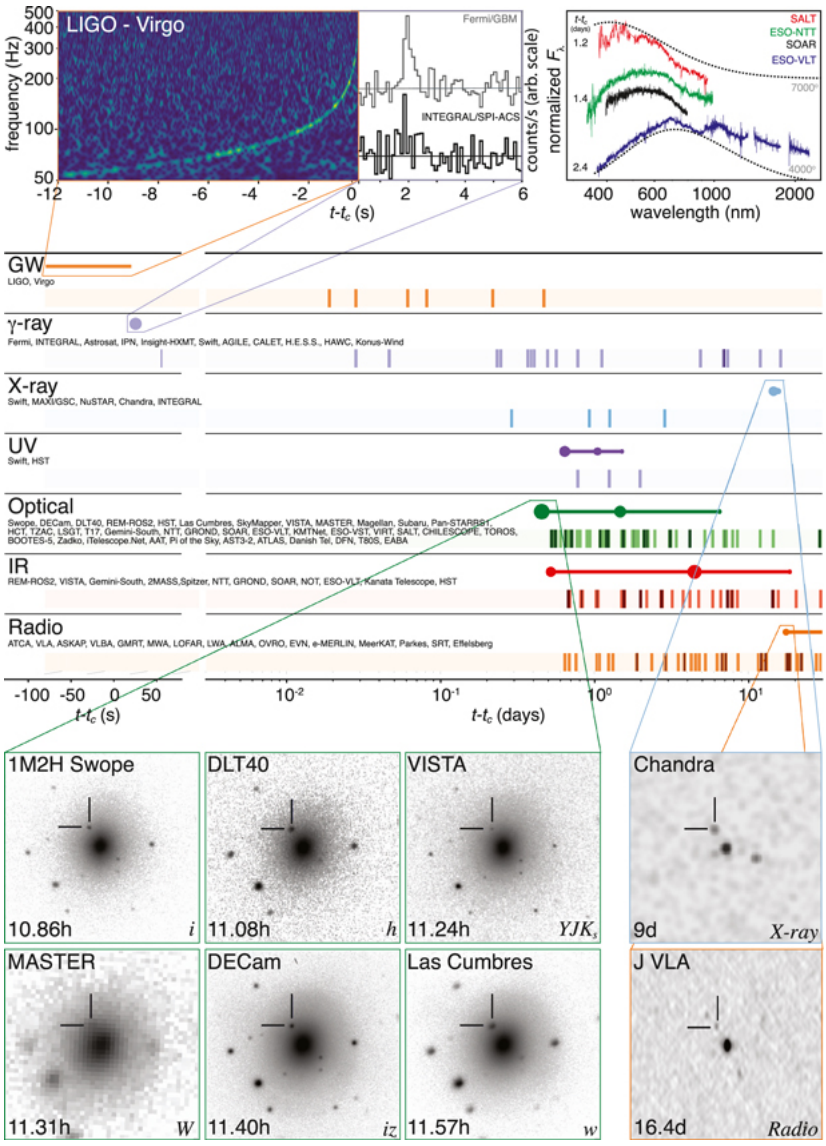

Figure 1.6: Timeline of the discovery of GW170817, GRB 170817A, SSS17a/AT 2017gfo, and the follow-up observations are shown by messenger and wavelength relative to the time of the gravitational-wave event. From Ref. [89].

At 60 s before the merger, the gravitational wave from the inspiraling NSs started to appear in Ligo-Virgo data. At 0 s, 12:41:04 UTC, the two stars merged and an accompanying gamma-ray burst is discovered by the Fermi satellite 1.7 s after merger. Fig. 1.5 shows the time-frequency signal of the gravitational wave GW170817, observed by the Ligo-Hanford, Ligo-Livingston and Virgo detectors. The signal clearly shows in the data of the first two detectors, while it is not visible in the data of Virgo. This is due to the lower binary NS horizon and the direction of the source with respect to the detector's antenna pattern [3].

However, the Virgo data is significant for the localization of the source although it cannot contribute to other parameters of GW170817. Thanks to the invisible signal in Virgo, the sky location of the event quickly mapped to an area of $28\,\mathrm{deg}^2$ from the one of $190\,\mathrm{deg}^2$ with only Ligo data [3]. And this is just 5 hours after the binary NS merger. The fast mapping of the source location allowed the detection of the follow-up electromagnetic counterparts. All telescopes turned to the direction of the gravitational wave event after Ligo-Virgo determined its location. The timeline of discovery of each signal is shown in Fig. 1.6. The first optical detection was reported by the Swope Telescope 11 hours after merger. Five other observatories, including DLT40, VISTA, MASTER, DECam and Las Cumbres, took independent images of the event within an hour after the Swope, as shown in Fig. 1.6. X-ray data from the event have been detected by the Chandra satellite during 9 days and the radio emission was also detected by the Very Large Array observatory during 15 days.

From the gravitational wave signal, one could get the general information of the binary system, assuming the components with low spin. The values of obtained parameters are shown in Table. 1.2. Firstly, the best measured parameter is the chirp mass $M_{\mathrm{chirp}} \equiv (m_1 m_2)^{3/5}(m_1 + m_2)^{-1/5} = 1.188^{+0.004}_{-0.002} M_\odot$. The ranges of the component masses m_1 and m_2 are $m_1 = 1.36 - 1.60 M_\odot$ and $m_2 = 1.17 - 1.36 M_\odot$, respectively. The corresponding mass ratio $q = m_2/m_1$, where $m_1 \geq m_2$, is between 0.7 and 1.0. The total mass of the system is given as $2.74^{+0.004}_{-0.001} M_\odot$. In addition, a particular quantity, tidal deformability, that describes how much a body is deformed by the external gravitational field, can be constrained by the gravitational wave event. Based on the analysis of GW170817, the tidal deformability of a NS with $1.4 M_\odot$, $\Lambda_{1.4}$, is between 70 and 580 [4]. The average tidal

Table 1.2: The source properties of GW170817 with low-spin priors.

Parameter	Value
Chirp mass $M_{\rm chirp}$	$1.188^{+0.004}_{-0.002} M_\odot$ [3]
Primary mass m_1	$1.36 - 1.60 M_\odot$ [3]
Secondary mass m_2	$1.17 - 1.36 M_\odot$ [3]
Mass ratio $q = m_2/m_1$	0.7 – 1.0 [3]
Total mass $m_{\rm tot}$	$2.74^{+0.004}_{-0.001} M_\odot$ [3]
Average tidal deformability$\tilde{\Lambda}$	70 – 720 [5]
Dimensionless tidal deformability $\Lambda_{1.4M_\odot}$	70 – 580 [4]

deformability, defined by

$$\tilde{\Lambda} = \frac{16}{13}\frac{(1+12q)\Lambda_1 + (q+12)\Lambda_2}{(1+q)^5} + (1 \leftrightarrow 2), \tag{1.10}$$

is about 70 – 720 [5]. Also, combining with an analysis of the electromagnetic counterpart with kilonova, a higher lower limit is deduced, $\tilde{\Lambda} > 400$ [90]. Recently, this value was updated to $\tilde{\Lambda} > 300$ [91, 92], although this lower bound has been disputed [93].

1.4 Equation of state of dense matter

The EOS indicating the relation of the thermal quantities, for instance, the equation of pressure and energy density $p(\epsilon)$, is the key ingredient of theoretical study of NSs. By using the TOV equation,

$$\frac{dp}{dr} = -\frac{m\varepsilon}{r^2}\frac{(1+p/\varepsilon)\left(1+4\pi r^3 p/m\right)}{1-2m/r}, \quad \frac{dm}{dr} = 4\pi r^2 \epsilon, \tag{1.11}$$

one can uniquely determine the mass-radius relation of NSs as sketched in the Fig. 1.7. A stiff EOS which means one with higher pressure for a given energy density, causes a higher maximum mass of NSs, since higher pressure is able to overcome the stronger gravity and prevents the massive stars from collapsing to black holes. A soft EOS, accordingly, yields

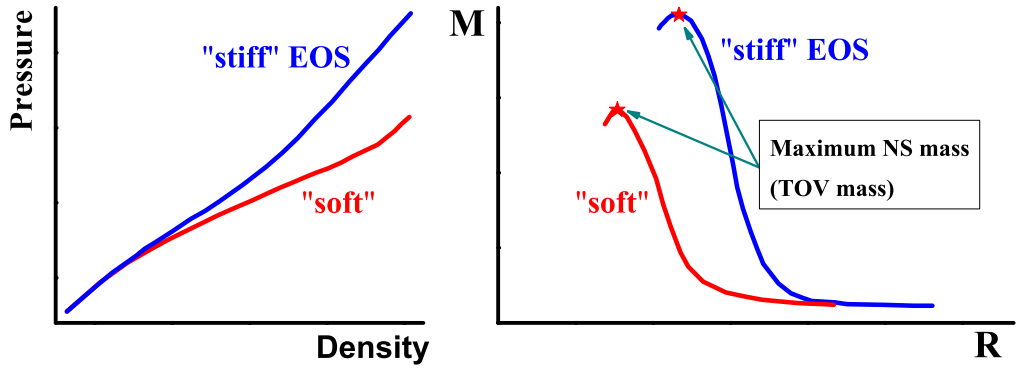

Figure 1.7: Two examples of EOSs of NSs and the corresponding R-M relations. The stiff EOS (blue curve) features a higher pressure P for a given energy density ϵ, and achieves a higher maximum TOV mass of NSs. On the contrary, the soft EOS (red curve) with lower pressure is not able to maintain too massive NSs due to the stronger gravity inside. The small branches after the point of maximum mass represent the unstable NSs which collapse to black holes in the end.

a lower maximum mass compared to the stiff EOS. We are interested in the maximum mass because a low limit on the maximum mass can be determined by the most massive NS observed. This low limit would be a useful constraint on the selection of the EOS.

In principal, there is only one 'true' EOS for NSs, and thus only one unique $M(R)$ relation exists. However, the scarce knowledge of the strong interaction leads to a bunch of EOSs based on various theoretical models. Quantum chromodynamic (QCD), a well-founded theory of the strong interaction, is supposed to determine the 'true' EOS. Within the current experiments and theoretical predictions, one can estimate the possible phases of QCD depending on the temperature T and chemical potential μ (or density). As shown in Fig. 1.8, the white sector is the region of the hadronic phase, while the outside of the sector represents the region of the deconfined quark phase. At high density, accurate calculations of the EOS (for the QGP) are obtained due to the asymptotic freedom of QCD. For the lower-energy area where the chromodynamic is no longer weakly coupled, lattice QCD provides a useful method to calculate the

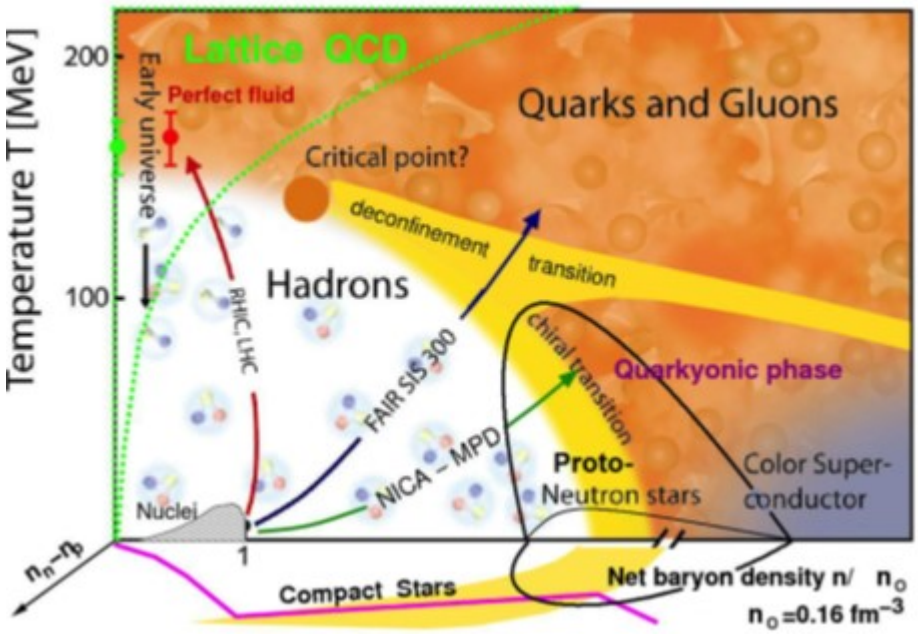

Figure 1.8: QCD phase diagram, cited from Ref. [94].

EOS at nonzero T; however, there are no ab-initio QCD calculations for dense matter available at the finite chemical potential branch (including the region where NSs locate) [95].

With intensive efforts, a large set of possible EOSs have been proposed. For nuclear matter, the approaches can be divided into two categories in general, phenomenological approaches and ab-initio approaches, depending on the choice of the interaction and many-body method.

Phenomenological approaches are based on effective interactions with a small number of parameters (of the order 10) fitted to nuclei properties. For example, the meson-exchange forces in the relativistic mean-field theory models and the Skyme and Gogny forces in the nonrelativistic calculations [95]. The advantage of phenomenological approaches is that they usually have a simple functional form, which may be used in several applications. Ab-initio approaches start from two- and three-body realistic nucleon interaction. Nucleon interactions are fitted to experimental data of nucleon-nucleon (NN) scattering in vacuum and the properties of bound nucleon systems. Because of the large amount of experimental

data, the precision of NN interactions has reached a very high degree.

Regarding the descriptions of quark matter, they presently resort to more or less phenomenological models, such as the MIT bag model [96], Nambu-Jona-Lasino model [97], field correlator method [98, 99] and Dyson-Schwinger quark model [36, 100]. These models inevitably contain several free-adjusted parameters. By adjusting them, almost every quark model could meet the constraints from the current observations of NSs. Furthermore, terrestrial nuclear experiments could put additional constraints on the nuclear EOSs, while there is no such experimental data able to limit quark-matter EOSs. Accordingly, many quark-matter EOSs are allowed and constraints on quark-matter EOSs more rely on the theoretical aspects. Although the quark-matter EOS remains uncertain, it is still interesting to discuss the effects of quark matter on NSs. As more properties of NSs have been observed, for instance, the tidal deformability and the cooling data, firm constraints on the EOS of quark matter could be obtained.

Note that the perturbative QCD is not a very good approach for describing the EOS of quark matter in the core of NSs, although quark matter appears at high density. The highest core density of NSs is around $20\rho_0$, however, the relative uncertainty of perturbative QCD is already $\pm 24\%$ at $\rho = 40\rho_0$ ($\mu_B = 2.6\,\mathrm{GeV}$) [40]. The covered density range inside NSs is in the region where the perturbative QCD is valid.

Chapter 2

Modeling the equation of state

In this chapter, several EOSs used for describing the dense matter inside NSs are introduced. For the description of nuclear matter, we consider the microscopic EOS derived within Brueckner-Hartree-Fock many-body theory with realistic two-body and three-body forces. The possibility of exotic matter, quark matter, is also studied, thus we present two quark models in this chapter, including field correlator model (FCM) and Dyson-Schwinger quark model (DSM).

2.1 Nuclear equation of state

The construction of the hadronic EOS is based on the BHF many-body theory with realistic two-body and three-body nucleonic forces. BHF theory is a widely used method developed by Brueckner and Bethe in the 1950s, aimed to solve many-body problems. In fact, it can be derived from the Brueckner-Bethe-Goldstone hole-line expansion, and the ground-state energy of a many-body system can be evaluated by truncating the expansion at two-hole-line level. An extensive discussion of this method is present in Ref. [101]. Within the BHF theory, the energy per nucleon of nuclear matter is given in terms of the solution of the Bethe-Goldstone

equation for the in-medium interaction $G[W;\rho]$,

$$\frac{B}{A} = \frac{3}{5}\frac{k_F^2}{2m} + \frac{1}{2\rho}\sum_{k,k'<k_F}\langle kk'|G[e(k)+e(k');\rho]|kk'\rangle_A\,, \tag{2.1}$$

where the form of $G[W;\rho]$ is given by

$$G[W;\rho] = V + \sum_{k_a,k_b>k_F} V\frac{|k_a,k_b\rangle Q\langle k_a,k_b|}{W-e(k_a)-e(k_b)}G[W;\rho]\,. \tag{2.2}$$

V is the bare nucleon-nucleon (NN) interaction, ρ is the nucleon number density, and W the starting energy. The single-particle energy

$$e(k) = e(k;\rho) = \frac{k^2}{2m} + U(k;\rho) \tag{2.3}$$

and the Pauli operator Q determine the propagation of intermediate baryon pairs. The BHF approximation for the single-particle potential using the continuous choice is

$$U(k;\rho) = \sum_{k'\le k_F}\langle kk'|G[e(k)+e(k');\rho]|kk'\rangle_A\,. \tag{2.4}$$

Due to the occurrence of $U(k)$ in Eq. (2.3), the above equations constitute a coupled system that has to be solved in a self-consistent manner for several momenta of the particles involved, at the considered densities. The only input quantities of the calculation are the NN two-body potentials, for instance, the Argonne V_{18} [102] potential supplemented with phenomenological Urbana three-body forces.

For the calculation of the energy per nucleon of asymmetric nuclear matter, we use the so-called parabolic approximation [103]

$$\frac{B}{A}(\rho,x) = \frac{B}{A}(\rho,x=0.5) + (1-2x)^2 E_{\rm sym}(\rho)\,, \tag{2.5}$$

where $x = \rho_p/\rho$ is the proton fraction and $E_{\rm sym}(\rho)$ is the symmetry energy, which can be expressed in terms of the difference of the energy per

nucleon of pure neutron matter ($x = 0$) and symmetric matter ($x = 0.5$):

$$E_{\rm sym}(\rho) = \frac{B}{A}(\rho, x = 0) - \frac{B}{A}(\rho, x = 0.5)\,. \tag{2.6}$$

For practical use the results of the energy per nucleon of pure neutron and symmetric matter are fitted by an analytic form with four parameters:

$$\frac{B}{A}(\rho) = a\rho + b\rho^c + d. \tag{2.7}$$

The parameterized results with different interactions can be found in Refs. [104, 105].

Once we obtain the energy per nucleon of asymmetric nuclear matter, then the total energy density of nuclear matter as a function of the density can be written as

$$\varepsilon_{\rm nucl}(\rho, x) = \rho m_N + \rho\frac{B}{A}(\rho, x), \tag{2.8}$$

where m_N is the nucleon mass. Once the energy density is known, the chemical composition of the beta-equilibrated matter can be calculated and finally the EOS,

$$p_{\rm nucl} = \rho^2 \frac{d(B/A)}{d\rho}\bigg|_A\,. \tag{2.9}$$

2.2 Quark matter equation of state

2.2.1 Field correlator theory

The FCM has already been used in the description of hybrid stars with the aim of determining the mass-radius relation of the star, and deducing possible constraints on the parameters of the model [35, 106, 107, 108, 109]. In this approach, discussed in detail in [110], the description of the strong interaction dynamics is performed in terms of Gaussian correlators of color-electric, $D^E(x)$, $D_1^E(x)$, and color-magnetic fields, $D^H(x)$, $D_1^H(x)$. The confinement mechanism is performed through the correlator $D^E(x)$. In this method, the disappearance of $D^E(x)$ indicates the deconfinement phase transition at $T \geq T_c$ [98]. The correlators $D_1^E(x)$, $D^H(x)$ and $D_1^H(x)$ describe the dynamics of the deconfined phase.

Since we are interested in the high-density matter existing in the NS core, the extension of the FCM to finite density (and temperature) is required, which was derived in [98, 99, 111] in the single-line approximation, where the leading contribution is given by the interaction of single quark and gluon lines with the vacuum. The resulting pressure of the quark matter phase,

$$p_{\rm QM} = p_V + p_g + \sum_{q=u,d,s} p_q \,, \tag{2.10}$$

is the sum of the vacuum p_V, gluon p_g and quark p_q contributions, which are reported below.

$$p_q = \frac{T^4}{\pi^2}\left[\phi_\nu\Big(\frac{\mu_q - V_1/2}{T}\Big) + \phi_\nu\Big(-\frac{\mu_q + V_1/2}{T}\Big)\right] \tag{2.11}$$

is the quark pressure, where p_q is intended for each single flavor (considering u, d and s quarks) with bare quark mass m_q ($\nu = m_q/T$) and chemical potential μ_q, V_1 is the large-distance static quark-antiquark potential, and

$$\phi_\nu(a) = \int_0^\infty du \frac{u^4}{\sqrt{u^2+\nu^2}} \frac{1}{\exp\left(\sqrt{u^2+\nu^2} - a\right) + 1} \,. \tag{2.12}$$

The vacuum pressure representing the pressure difference between the vacua in the deconfined and confined phases, is given by

$$p_V = -\frac{(11 - 2N_f/3)}{32}\frac{G_2}{2}, \tag{2.13}$$

where $N_f = 3$ is the number of flavors, G_2 is the gluon condensate which is sharply reduced by half at the transition observed at the critical temperature [112, 113].

Apart from the external parameters μ_q and T (and the quark masses m_q), $p_{\rm QM}$ depends on two parameters that are peculiar to the model, namely V_1 and G_2. The parameter V_1 at zero temperature and density is expressed in terms of an integral of a fundamental QCD correlator [110], but is not directly measured. The gluon condensate G_2 is estimated from QCD sum rules, $G_2 \approx 0.012$ GeV^4, but with an uncertainty of about

50%. In addition, from Eq. (2.13) we notice that G_2 has the same role as the bag constant of the MIT bag model and thus, if one sets $V_1 = 0$, the quark pressure $p_{\rm q}$ becomes the pressure of free quarks and the model reduces to the simplest version of the bag model. Therefore V_1 represents the main correction to the free quarks dynamics inside the bag.

Although there exist some speculations on the temperature dependence of V_1 and G_2 and on their estimates at the critical temperature [35, 98, 99, 107], not much is known about their dependence on the baryonic density, which is certainly relevant for the description of the inner core of NSs. Therefore, for our purpose, it is preferable to avoid specific assumptions about the temperature and density dependence and to treat V_1 and G_2 as free parameters. In this spirit, some indications on the phenomenologically acceptable ranges of V_1 and G_2, that predict maximum hybrid star masses compatible with the observational limits, have been obtained in [108, 109], suggesting large values of the interaction strength, $V_1 \sim 100 - 200$ MeV and rather small values of the gluon condensate, $G_2 \sim 0.002 - 0.006$ GeV^4.

2.2.2 Dyson-Schwinger quark model

The Dyson-Schwinger equation is the equation of motion of QCD, which is rigorously derived from the generating functional under the framework of continuum field theory. In Euclidian space, the generating functional Z reads

$$Z[j] \;=\; \int D\phi \, \exp(-S_E + j_i \phi_i), \tag{2.14}$$

where $\phi_i = q,\ \bar{q},\ A^a_\mu,\ c,\ \bar{c}$ are various fields, $j_i = \bar{\eta},\ \eta,\ J^a_\mu,\ \bar{\omega},\ \omega$ represent external sources,

$$j_i \phi_i = \int d^4x \big[\bar{\eta}(x) q(x) + \bar{q}(x)\eta(x) + J^a_\mu(x) A^{\mu a}(x) + \bar{\omega}(x) c(x) + \bar{c}(x)\omega(x)\big], \tag{2.15}$$

and the action S_E can be written as

$$S_E = \int d^4x(L_0 + L_1), \tag{2.16}$$

$$L_0 = \sum_{f=1}^{N_f} \bar{q}^f(\gamma_\mu \cdot D_\mu + m_0^f)q^f + \frac{1}{4}\int F^a_{\mu\nu}F^a_{\mu\nu}, \tag{2.17}$$

$$L_1 = -\frac{1}{2\xi_0}[\partial_\mu A^a_\mu(x)]^2 + \partial_\mu\bar{\omega}_a(x)[\delta^{ab} - g_0 f^{abc}A^c_\mu(x)]\omega^b(x), \tag{2.18}$$

with $D_\mu = \partial_\mu + igA^a_\mu\frac{\lambda^a}{2}$ and field-strength tensor $F^a_{\mu\nu} = \partial_\mu A^a_\nu - \partial_\nu A^a_\mu + g_0 f^{abc}A^b_\mu A^c_\nu$.

The trivial boundary condition gives

$$0 = \int D\phi\frac{\delta}{\delta\phi_i}\exp(-S_E + j_i\phi_i), \tag{2.19}$$

and starting with Eq. 2.19, one could get the identity related to the quark propagator $S(x, y)$, which is

$$\begin{aligned}&\delta(x-y) = (\gamma\cdot\partial + m_0)S(x,y) \\ &+g^2\gamma_\mu t^a\int d^4z_1d^4z_2d^4z_3D^{a,b}_{\mu\nu}(z_1,x)\Gamma^b_\nu(z_1,z_2,z_3)S(z_2,y)S(x,z_3),\end{aligned} \tag{2.20}$$

where $D^{ab}_{\mu\nu}(x, y)$ is the dressed gluon propagator and Γ^a_μ is the dressed quark-gluon vertex. They are defined as

$$S(x,y) \equiv \frac{\delta^2W[j]}{\delta\eta(y)\delta\bar{\eta}(x)}, \tag{2.21}$$

$$D^{ab}_{\mu\nu}(x,y) \equiv \frac{\delta^2W[j]}{\delta J^b_\mu(y)\delta J^a_\mu(x)}, \tag{2.22}$$

$$-ig\Gamma^a_\mu(z_1,z_2,z_3) \equiv \frac{\delta^3\Gamma[\phi^c]}{\delta A^a_\mu(z_1)\delta q(z_2)\delta\bar{q}(z_3)}, \tag{2.23}$$

with $W[j] = \ln(Z[j])$ and $\Gamma[\phi^c] = -W[j] + \phi^c_i j_i$. By performing a Fourier transform of Eq. 2.20, one can obtain the quark propagator in momentum

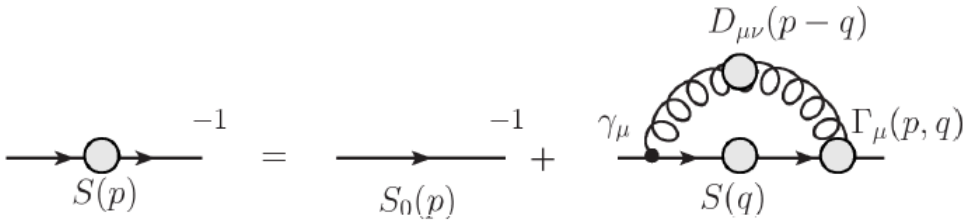

Figure 2.1: Quark propagator.

space

$$S(p)^{-1} = Z_2 i\gamma \cdot p + m_0 + Z_1 \int_q^\Lambda g^2 D_{\rho\sigma}(k) \frac{\lambda^a}{2} \gamma_\rho S(q) \Gamma^a_\sigma(q,p), \tag{2.24}$$

where p is the four momentum, $k = p - q$, and Z_1 and Z_2 are renormalization constants. The complete derivation is shown in Ref. [100].

In general, the Dyson-Schwinger equation of the n-point Green's function contains the Green's function of n+1 points, for instance, Eq. 2.24 is a equation for the 2-point Green's function (quark propagator), which contains a 3-point Green's function (quark-gluon vertex). Its Feynman diagram is shown in Fig. 2.1. Thus, the Dyson-Schwinger equation is a equation coupling Green's functions of all orders. In order to solve the equation, truncations for the quark-gluon vertex and gluon propagator are necessary. For the vertex we use the bare one, i.e., $\Gamma^a_\sigma = \frac{\lambda^a}{2}\gamma_\sigma$. For the dressed gluon propagator, we employ the scheme with an infrared-dominant interaction [36],

$$g^2 D_{\rho\sigma}(k) = 4\pi^2 d \frac{k^2}{\omega^6} e^{-\frac{k^2}{\omega^2}} \left(\delta_{\rho\sigma} - \frac{k_\rho k_\sigma}{k^2}\right). \tag{2.25}$$

The parameters ω and d in this equation are discussed in [114, 115]: ω represents the energy scale in nonperturbative QCD, like $\Lambda_{\rm QCD}$, and d controls the effective coupling strength. Their values as well as the quark masses are obtained by fitting light (π and K) meson properties and the chiral condensate in vacuum [114, 115], and we use the set $\omega = 0.5$ GeV and $d = 1$ GeV^2. Regarding the quark masses, we choose $m_{u,d} = 0$ and $m_s = 115$ MeV.

In order to reduce complexity of calculation, we rewrite the quark propagation in a general form with vector part and scalar part, which is

$$S(p)^{-1} = i\gamma p A(p^2) + B(p^2). \tag{2.26}$$

The calculation of the quark propagator amounts to solving for the two scalar functions $A(p^2)$ and $B(p^2)$. They satisfy

$$A(p^2) = Z_2 + \frac{4}{3p^2}\int^{\Lambda} \frac{d^4q}{(2\pi)^4}\frac{4\pi\mathcal{G}(k^2)}{k^2}\frac{(p\cdot q + 2\frac{p\cdot k q\cdot k}{k^2})A(q^2)}{A^2(q^2)q^2 + B^2(q^2)}, \tag{2.27}$$

$$B(p^2) = Z_4 m + \frac{4}{3}\int^{\Lambda} \frac{d^4q}{(2\pi)^4}\frac{4\pi\mathcal{G}(k^2)}{k^2}\frac{3B(q^2)}{A^2(q^2)q^2 + B^2(q^2)}. \tag{2.28}$$

Note that it is difficult to solve the equations analytically, only numerical results are available.

We are interested in the description of quark matter in the NS core. For this purpose, the extension of the Dyson-Schwinger equation to finite chemical potential μ is made, and reads

$$\begin{aligned} S(p;\mu)^{-1} &= Z_2[i\gamma \boldsymbol{p} + i\gamma_4(p_4 + i\mu) + m_q] \\ &\quad + Z_1\int\frac{d^4q}{(2\pi)^4}g^2(\mu)D_{\rho\sigma}(k;\mu)\frac{\lambda^a}{2}\gamma_\rho S(q;\mu)\Gamma^a_\sigma(q,p;\mu)\,. \end{aligned} \tag{2.29}$$

For solving this equation, one can follow a similar procedure as in the case of zero chemical potential. Note that the gluon propagator is also extended to finite chemical potential,

$$g^2(\mu)D_{\rho\sigma}(k,\mu) = 4\pi^2 d\frac{k^2}{\omega^6}e^{-\frac{\alpha\mu^2}{\omega^2}}e^{-\frac{k^2}{\omega^2}}\left(\delta_{\rho\sigma} - \frac{k_\rho k_\sigma}{k^2}\right). \tag{2.30}$$

In order to model the reduction rate of the effective interaction with increasing chemical potential, a phenomenological parameter α was introduced. Obviously, $\alpha = \infty$ corresponds to a noninteracting system at finite chemical potential, i.e., a simple version of the MIT bag model. Larger α corresponds to a stiffer quark-matter EOS.

Once the quark propagator is obtained, the thermal quantities are easy to be derived. Assuming there is no interaction between different flavors

of quarks, the quark $q = u, d, s$ momentum distribution function is obtained as

$$f_q(|\boldsymbol{p}|;\mu) = \frac{1}{4\pi}\int_{-\infty}^{\infty} dp_4\, \mathrm{tr_D}\big[-\gamma_4 S_q(p;\mu)\big]\,, \tag{2.31}$$

and the number density and pressure can be calculated as follows

$$n_q(\mu) = 6\int \frac{d^3\boldsymbol{p}}{(2\pi)^3}\, f_q(|\boldsymbol{p}|;\mu)\,, \tag{2.32}$$

$$p(\mu_u,\mu_d,\mu_s) = -B_{\mathrm{DS}} + \sum_{q=u,d,s}\int_{\mu_q^0}^{\mu_q} d\mu\, n_q(\mu)\,, \tag{2.33}$$

where the bag constant B_{DS} is another important parameter in our model. As discussed in [36, 116], $B_{\mathrm{DS}} \approx 90\ \mathrm{MeV\,fm^{-3}}$ can be obtained from the vacuum pressure in the massless two-flavor quark-matter (2QM) case in our model, but there are ambiguities when including strange quarks. In this work we treat it as a further phenomenological parameter like the reduction rate α. We notice that B_{DS} cannot be arbitrarily low, as one has to ensure that the pressure (energy density) of 2QM should be lower (larger) than that of symmetric nuclear matter at low density [1, 116].

2.3 EOS of dense matter in beta equilibrium

The dense matter in the core of NSs is supposed to be under beta equilibrium and charge neutrality. Starting with nuclear matter, the component particles are nucleons (n, p) and leptons (e, μ). Neutrinos escape fast from the core of NSs, so the condition of beta equilibrium can be written as

$$\mu_e = \mu_n - \mu_p = \mu_\mu, \tag{2.34}$$

where μ_i denote the chemical potential of the particle species $i = n, p, e, \mu$. Taking into account the parabolic approximation of the energy per nucleon of asymmetric nuclear matter, one has

$$\mu_e = -\frac{\partial B/A}{x}\bigg|_\rho = 4E_{\mathrm{sym}}(\rho)(1-2x), \tag{2.35}$$

which is dependent on the proton fraction and the nuclear symmetry energy. Combining with the charge neutrality ($\rho_p = \rho_e + \rho_\mu$), one can determine the composition of nuclear matter with a given baryon density ρ. Thus, the total pressure and the total energy density are given by

$$p = p_{\rm nucl} + p_{\rm lep}, \tag{2.36}$$

$$\varepsilon = \varepsilon_{\rm nucl} + \varepsilon_{\rm lep} = \rho\frac{B}{A} + \rho m_N + \varepsilon_{\rm lep}, \tag{2.37}$$

where m_N is the nucleon mass, $p_{\rm lep}$ and $\varepsilon_{\rm lep}$ are the leptonic contributions to the total pressure and energy density. The leptons here are treated as free particles.

Similarly, the fractions of each particle species (u, d, s, e, μ) in quark matter can be determined by the conditions of beta-stability and charge neutrality,

$$\mu_u + \mu_e = \mu_u + \mu_\mu = \mu_d = \mu_s\,, \tag{2.38}$$

$$\frac{2\rho_u - \rho_d - \rho_s}{3} - \rho_e - \rho_\mu = 0\,. \tag{2.39}$$

Then the total pressure and energy density are the sum of the contributions of all particle species.

The phase transition from hadronic matter to quark matter is expected at high density. However, the mechanism of phase transition remains uncertain, which could be a first-order phase transition or a crossover like the phase transition at high temperature [117]. One phenomenological method to construct the phase transition through interpolation, is the so-called three-windows modeling [118, 119, 120, 121]. The EOS at $\rho_B < \rho_0$ is described as nuclear-matter EOS, while at $\rho_B > 5\rho_0$ it is described as quark-matter EOS. The baryon density from $2\rho_0$ to $5\rho_0$ is the crossover regime where the EOS is constructed by interpolation. More dedicated phase transitions have been studied in Refs. [122, 123, 124, 125, 126], assuming a first-order phase transition between hadronic matter and quark matter; also a finite-size effects (for instance the surface and Coulomb energies) are taken into account. This results in a mixed phase with a pasta structure between hadronic and quark phases.

The Maxwell and Gibbs constructions correspond to the two extreme

cases of infinite and zero surface tension, respectively. In the Maxwell construction, hadronic matter and quark matter are separated and satisfy local charge neutrality due to the infinite surface tension. The pressure remains constant when the phase transition proceeds, thus a mixed phase is forbidden inside NSs. This also produces a jump in energy density, which often leads to an unstable branch in the mass-radius diagram. For a soft quark-matter EOS, there could be no stable hybrid-star branch or only a tiny one [36, 37, 97, 109].

In this work we consider another extreme case, the Gibbs construction, which disregards the finite-size effects. The basic idea of the Gibbs construction is that both nuclear and quark matter coexist in a mixed phase with local beta equilibrium and global charge neutrality (both phases are charged separately) [127]. These conditions can be expressed as

$$\mu_u + \mu_e = \mu_u + \mu_\mu = \mu_d = \mu_s\,, \tag{2.40}$$

$$\mu_p + \mu_e = \mu_n = \mu_u + 2\mu_d\,, \tag{2.41}$$

$$\chi\rho_c^Q + (1-\chi)\rho_c^H = 0\,, \tag{2.42}$$

where ρ_c^Q and ρ_c^H are the charge densities of the quark and nuclear phases and χ indicates the volume fraction occupied by quark matter in the mixed phase. In addition, the mechanical balance between nuclear matter and quark matter in the mixed phase gives

$$p_H = p_Q = p_M, \tag{2.43}$$

where p_H (p_Q) is the pressure of nuclear (quark) matter, which is also equal to the pressure of the mixed phase. Then the total baryon density and total energy density of the mixed phase are given as

$$\rho_M = \chi\rho_Q + (1-\chi)\rho_H\,, \tag{2.44}$$

$$\varepsilon_M = \chi\varepsilon_Q + (1-\chi)\varepsilon_H\,. \tag{2.45}$$

In Fig. 2.2 we present the numerical results of some EOSs for the cases discussed. More precisely, for nuclear matter (left panel), we show several BHF EOSs based on different nucleon-nucleon potentials, the Argonne V_{18}

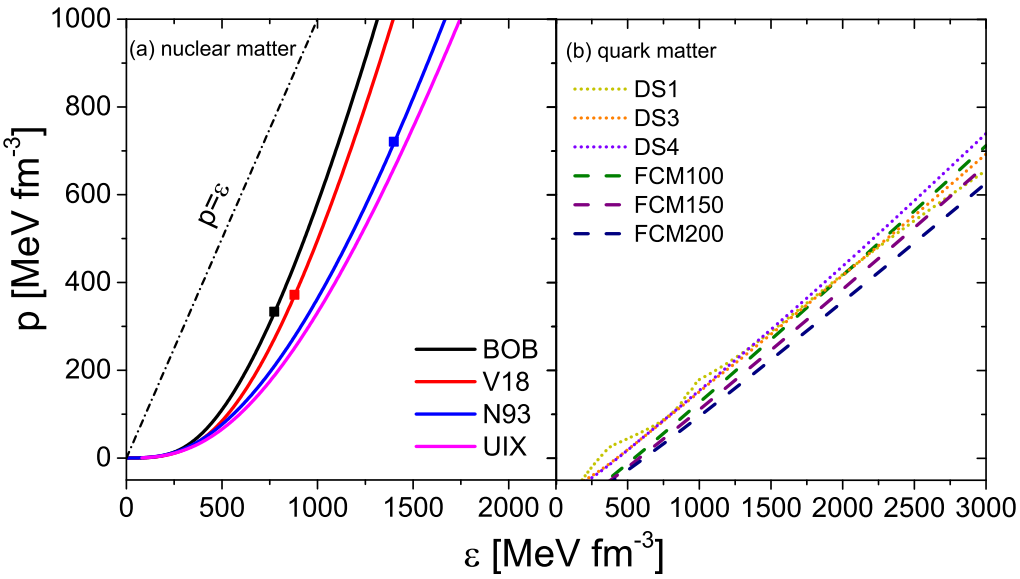

Figure 2.2: Pressure as a function of energy density for nuclear matter (left panel) and quark matter (right panel) under β equilibrium. The dotted curves are plotted for the DSM, dashed curves for the FCM approach. The solid squares indicate the points where the speed of sound becomes larger than the speed of light.

[102], the Bonn B (BOB) [128, 129], and the Nijmegen 93 (N93) [130, 131], and compatible three-nucleon forces as input. The BOB and N93 are supplemented with microscopic three-body forces employing the same meson-exchange parameters as the two-body potentials [132, 133, 134], whereas V_{18} is combined either with a microscopic or a phenomenological three-body force, the latter consisting of an attractive term due to two-pion exchange with excitation of an intermediate Δ resonance, and a repulsive phenomenological central term [135, 136, 137]. They are labelled as V18 and UIX, respectively. EOS BOB is the stiffest among these results, and is supposed to achieve higher maximum mass of NSs. However, at large density it breaks the causality condition, which means that the speed of sound, $c_s = \sqrt{dp/d\epsilon}$, is higher than the speed of light. The other three EOSs also show a superluminar speed of sound at very large energy density, as discussed in Ref. [138].

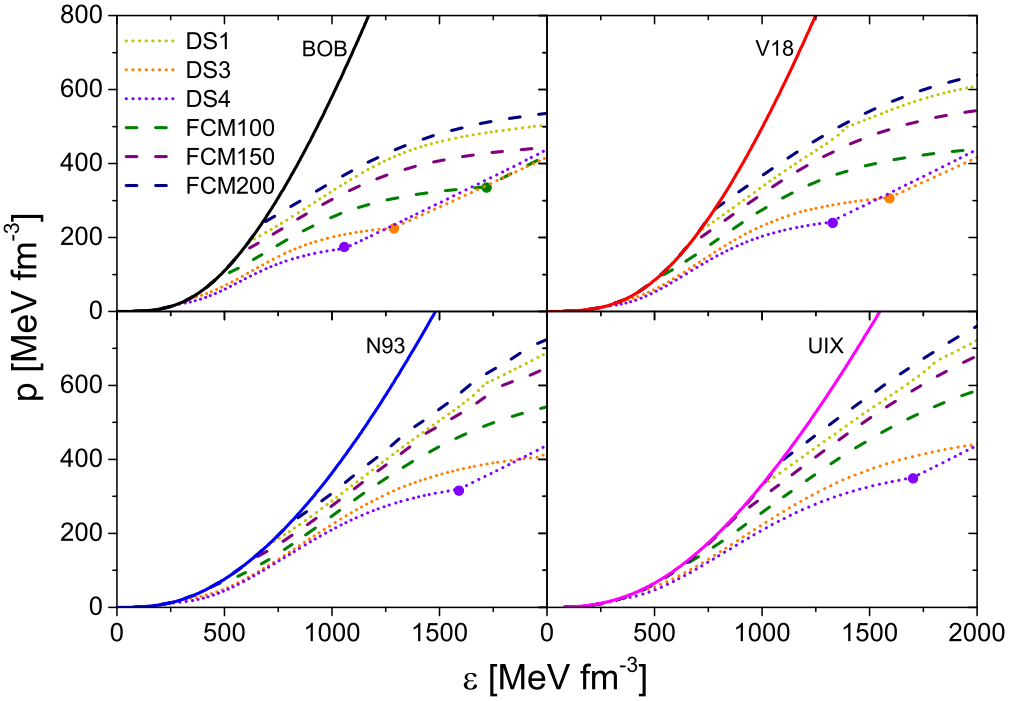

Figure 2.3: Pressure vs energy density of hybrid star matter under the Gibbs phase transition for the different models. The solid circles indicate the onset of pure quark matter.

The EOSs of quark matter within FCM and DSM approaches are shown in the right panel of Fig. 2.2. In the FCM, we fix the value of $G_2 = 0.006\,\mathrm{GeV}^4$ and choose parameter values $V_1 = 100, 150, 200\,\mathrm{MeV}$ (labeled as FCM100, FCM150, FCM200). Similarly, we describe the quark phase in the DSM with a parameter $\alpha = 1, 3, 4$ and fixed $B_{\mathrm{DS}} = 90\,\mathrm{MeVfm}^{-3}$. As we can see, most quark-matter EOSs show a good linear relation between pressure and energy density, except EOS DS1 having an exotic behavior at lower energy density. Actually this is due to the appearance of s quarks. For the DS1, the threshold chemical potential is about $\mu_s = 500\,\mathrm{MeV}$ [36]. This nonlinear region indicates the conversion of two-flavor quark matter to three-flavor quark matter. A common conclusion that can be obtained from both DSM and FCM is that the quark-matter EOS becomes stiff when the system tends to be noninteracting. Remind that in the FCM

(DSM), the parameter $V_1 = 0$ ($\alpha = \infty$) corresponds to a noninteracting system.

In Fig. 2.3, we present the hybrid-star EOSs constructed under the Gibbs phase construction. The solid dots indicate the onset of pure quark matter. It is clear that the appearance of quark matter softens the EOS. However, the soft quark-matter EOS does not result in a soft hybrid-star EOS. In fact, a stiff quark-matter EOS has a lower phase transition point, which reduces the fraction of nuclear matter and makes the overall EOS soft. For example, FCM100 is the stiffest one among the three FCM EOSs, but the corresponding hybrid-star EOS is the most soft one.

Chapter 3

Constraints on the equation of state

EOSs can be constrained by different observables, for instance, the observations from NSs. Currently, the main constraints originate from three aspects [95]: observations in astronomy, laboratory measurements of nuclear properties and reactions and theoretical ab-initio calculations. In this chapter, we discuss these constraints on the EOSs introduced in Chapter 2. We first discuss the constraints from NSs, in particular the constraints from GW170817, on the EOSs for both nuclear matter and quark matter. Regarding the EOSs of nuclear matter, additional constraints can be obtained from the properties of nuclear matter at saturation density. In the last section, we investigate the correlations between NS and nuclear-matter observables.

This chapter is a modified version of the following articles:

[1] G. F. Burgio, A. Drago, G. Pagliara, H.-J. Schulze, and J. -B. Wei, *Are Small Radii of Compact Stars Ruled out by GW170817/AT2017gfo?*, Astrophys. J . 860, 139 (2018).

[2] J. -B. Wei, J.-J. Lu, G. F. Burgio, Z. H. Li, and H.-J. Schulze, *Are nuclear matter properties correlated to neutron star observables?*, Eur. Phys. J. A 56, 63 (2019).

3.1 Constraints from neutron star systems

3.1.1 M-R relations and tidal deformability

The tidal deformability λ, or equivalently the tidal Love number k_2 of a NS [139, 140, 141], has recently been acknowledged to provide valuable information and constraints on the related EOS. In general relativity, it can be calculated along with the TOV equations for pressure p and enclosed mass m of a static NS configuration. The only input required is the EOS. More specifically, the Love number can be obtained by solving the equations

$$\begin{aligned} k_2 &= \frac{3}{2}\frac{\lambda}{R^5} = \frac{3}{2}\beta^5\lambda = \frac{8}{5}\frac{\beta^5 z}{F}\,, \\ & z \equiv (1-2\beta)^2[2 - y_R + 2\beta(y_R - 1)]\,, \\ & F \equiv 6\beta(2-y_R) + 6\beta^2(5y_R - 8) + 4\beta^3(13 - 11y_R) \\ & \quad + 4\beta^4(3y_R - 2) + 8\beta^5(1 + y_R) + 3z\ln(1-2\beta)\,, \end{aligned} \tag{3.1}$$

(with $\Lambda \equiv \lambda/M^5$ and $\beta \equiv M/R$ being the compactness) along with a system of three coupled first-order differential equations [142], namely

$$\frac{dp}{dr} = -\frac{m\varepsilon}{r^2}\frac{(1+p/\varepsilon)\left(1+4\pi r^3 p/m\right)}{1-2m/r}\,, \tag{3.2}$$

$$\frac{dm}{dr} = 4\pi r^2\varepsilon\,, \tag{3.3}$$

$$\begin{aligned} \frac{dy}{dr} &= -\frac{y^2}{r} - \frac{y-6}{r-2m} - rQ\,, \\ & Q \equiv 4\pi\frac{(5-y)\varepsilon + (9+y)p + (\varepsilon+p)/c_s^2}{1-2m/r} - \left[\frac{2(m+4\pi r^3 p)}{r(r-2m)}\right]^2, \end{aligned} \tag{3.4}$$

with the EOS $\varepsilon(p)$ as input, and boundary conditions given by

$$[p, m, y](r=0) = [p_c, 0, 2]\,, \tag{3.5}$$

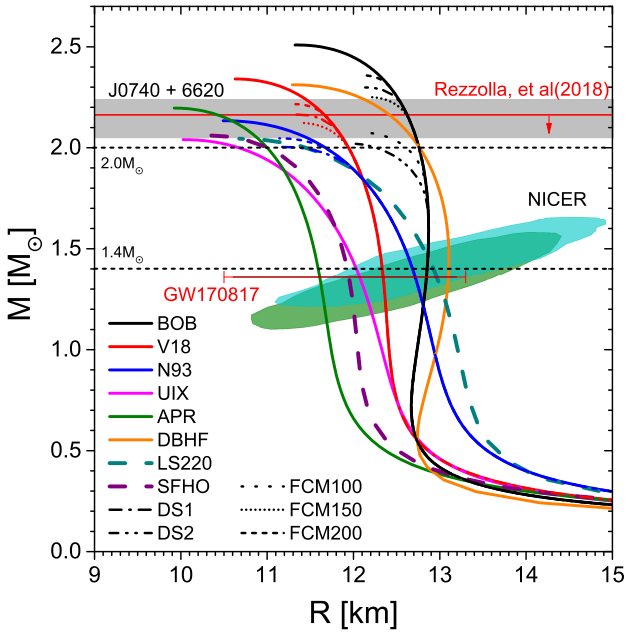

Figure 3.1: Mass-radius relations for different EOSs. Solid (dashed) curves are plotted for microscopic (phenomenological) EOSs. The thin curves indicate hybrid stars in the DSM and FCM approaches. Some experimental constraints from NICER (blue area [86] or green area [87]), GW170817 (red bar) [4] and currently observed maximum mass (grey area) [74] are also shown. The red horizontal line indicates the predicted upper limit of $M_{\rm max} < 2.16\,M_\odot$ [82]. The additional constraints from GW170817 on radius, $R_{1.6} > 10.8$km [143] and $R_{1.4} < 13.5$ km [144] (updated to 13 km), are not shown.

being $y_R \equiv y(R)$, and the mass-radius relation $M(R)$ provided by the condition $p(R) = 0$ for varying p_c.

In Table 3.1, the properties of the various NS configurations constructed with the considered EOSs are listed, including the value of the maximum mass, the corresponding radius, the radius of the $1.4M_\odot$ configuration and its tidal deformability $\Lambda_{1.4}$.

In addition to the BHF EOSs discussed for nuclear matter, we also compare with the often-used results of the Dirac-BHF method (DBHF) [151, 152, 148], which employs the Bonn A potential, and the APR EOS based on the variational method [147, 153] and the V_{18} potential. The

Table 3.1: Properties of NSs listed according to the considered EOSs. See text for details. From Ref. [145].

EOS	$M_{\max}[M_\odot]$	$R_{M_{\max}}$ [km]	$R_{1.4}$ [km]	$\Lambda_{1.4}$	Type	Ref.
BOB	2.51	11.32	12.85	584	nucleonic	[104]
BOB+DS1	2.30	12.13	12.85	584	hybrid	[36]
BOB+DS2	2.02	11.95	12.85	584	hybrid	[36]
BOB+DS3	1.79	11.72	12.75	539	hybrid	[36]
BOB+DS4	1.60	11.38	12.12	346	hybrid	[36]
BOB+FCM100	2.08	12.09	12.85	584	hybrid	[109]
BOB+FCM150	2.25	12.17	12.85	584	hybrid	[109]
BOB+FCM200	2.36	12.10	12.85	584	hybrid	[109]
V18	2.34	10.63	12.33	419	nucleonic	[104]
V18+DS1	2.16	11.34	12.33	419	hybrid	[36]
V18+DS2	1.93	11.15	12.33	419	hybrid	[36]
V18+DS3	1.75	10.95	11.96	320	hybrid	[36]
V18+DS4	1.61	10.74	11.36	215	hybrid	[36]
V18+FCM100	1.98	11.28	12.33	419	hybrid	[109]
V18+FCM150	2.12	11.38	12.33	419	hybrid	[109]
V18+FCM200	2.22	11.32	12.33	419	hybrid	[109]
N93	2.13	10.49	12.68	474	nucleonic	[104]
N93+DS1	2.00	11.17	12.68	474	hybrid	[36]
N93+DS2	1.80	10.76	12.64	459	hybrid	[36]
N93+DS3	1.67	10.48	11.76	250	hybrid	[36]
N93+DS4	1.58	10.31	11.05	162	hybrid	[36]
N93+FCM100	1.84	10.89	12.68	474	hybrid	[109]
N93+FCM150	1.96	11.13	12.68	474	hybrid	[109]
N93+FCM200	2.05	11.14	12.68	474	hybrid	[109]
UIX	2.04	10.02	12.03	340	nucleonic	[146]
UIX+DS1	1.98	10.59	12.03	340	hybrid	[36]
UIX+DS2	1.82	10.63	12.03	340	hybrid	[36]
UIX+DS3	1.69	10.44	11.81	10	hybrid	[36]
UIX+DS4	1.59	10.30	11.22	6	hybrid	[36]
UIX+FCM100	1.84	10.53	12.03	340	hybrid	[109]
UIX+FCM150	1.93	10.48	12.03	340	hybrid	[109]
UIX+FCM200	1.99	10.35	12.03	340	hybrid	[109]
APR	2.20	9.92	11.59	274	nucleonic	[147]
DBHF	2.31	11.29	13.10	681	nucleonic	[148]
LS220	2.04	10.67	12.94	542	nucleonic	[149]
SFHO	2.06	10.31	11.93	334	nucleonic	[150]
V18(N+Y)	1.65	9.00	11.92	302	hyperonic	[23]
BOB(N+Y)	1.37	11.07	–	–	hyperonic	[36]

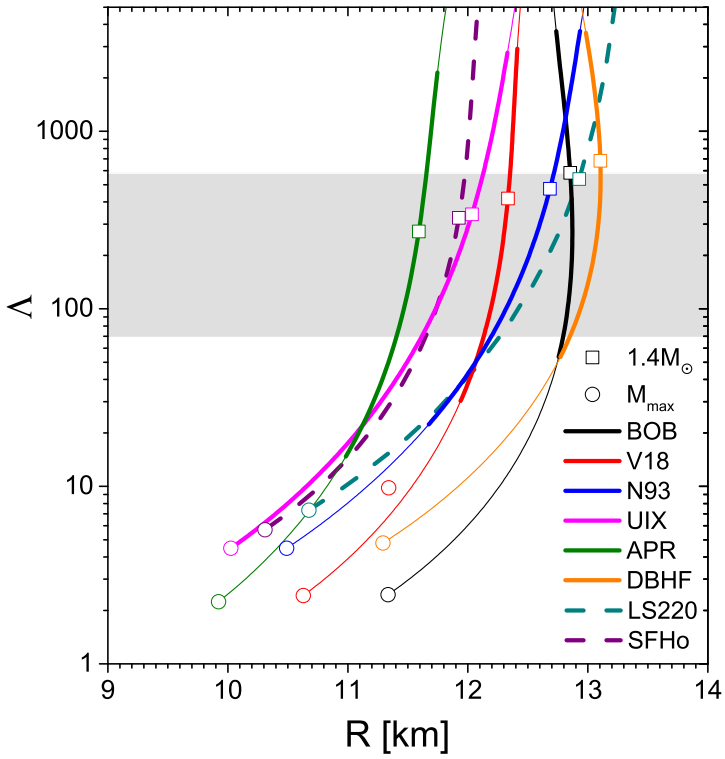

Figure 3.2: Tidal deformability vs radius for different EOSs. Solid (dashed) curves are plotted for microscopic (phenomenological) EOSs. The open circles and squares indicate configurations of $M = M_{\rm max}$ and $M = 1.4M_\odot$, respectively. The grey band represents the constraint on $\Lambda_{1.4}$ [4].

LS220 [149] and SFHo [150] phenomenological RMF EOSs are also used for comparison. Two hyperonic EOSs obtained within the BHF approach are also included, which are labeled as BOB(N+Y) [154, 155, 156] and V18(N+Y) [23].

Regarding the hybrid stars, we have chosen the interaction parameter $\alpha = 1, 2, 3, 4$ in the DSM and matched with each BHF EOSs under the Gibbs construction, see Sec. 2.3. This yields 16 different EOSs (BOB, V18, UIX, N93) $\otimes$ (DS1, DS2, DS3, DS4) for hybrid stars. The same construction is made for the one of FCM, but with the parameter $V_1 = 100, 150, 200$ MeV. We remind that the gluon condensate parameter

G_2 is set to $G_2 = 0.006\,\mathrm{GeV}^4$ for all choices of V_1.

We observe that most models give values of the maximum mass larger than 2 $M_\odot$, and therefore are compatible with current observational data [73, 74, 157, 158]. Hybrid stars can achieve 2 $M_\odot$ by adjusting models parameters, i.e. α in DSM and V_1 in FCM. However, no firm conclusions can be drawn on quark models since the hybrid star EOS also depends on the nucleonic EOS. For example, the hybrid star EOS constructed with BOB is able to give an upper limit of the parameter $\alpha \lesssim 2$ due to the 2 $M_\odot$ constraint, while there is no value of α allowed if we adapt UIX for describing the nuclear matter in the hybrid star. Furthermore, the two hyperonic EOSs do not fulfill the observational limit. We nevertheless include them in our analysis in order to see whether they reveal irregular features elsewhere. Some recent analyses of the GW170817 event indicate an upper limit of the maximum mass of about 2.2 $M_\odot$ [159, 160, 82], with which several of the microscopic EOSs would be compatible.

We now turn to discuss the mass-radius relations of the different EOSs we consider. They are shown in Fig. 3.1, where results obtained with microscopic (phenomenological) EOSs are displayed as thick solid (dashed) curves. Moreover we consider the nine EOSs for hybrid stars with $M_{\mathrm{max}} > 2\,M_\odot$ in Table 3.1, obtained by performing a Gibbs phase transition between the BOB, V18, or N93 hadronic EOS and the DSM (FCM) EOS characterized by different values of $\alpha = 1, 2$ ($V_1 = 100, 150, 200\,\mathrm{MeV}$). They are displayed as thin broken curves.

According to Fig. 3.1 (see also Table 3.1), the predicted radii for a $M = 1.4\ M_\odot$ NS span a range $11.6 \lesssim R_{1.4} \lesssim 13.1\,\mathrm{km}$. Those values are in agreement with the ones reported in Ref. [144], where an analysis of the results of GW170817 was performed by using a general polytropic parametrization of the EOS compatible with perturbative QCD at very high density. In Ref. [144] it has been shown that the tidal deformability limit of a $1.4M_\odot$ NS, $\Lambda_{1.4} < 800$, as found in GW170817, implies a radius $R_{1.4} < 13.6\,\mathrm{km}$. This has been updated to $R_{1.4} < 13\,\mathrm{km}$ with a new constraint of $\Lambda_{1.4} < 580$ [4].

For a better illustration, we present the tidal deformability Λ for the considered EOSs as a function of radius in Fig. 3.2. The grey band represents the constraints of $\Lambda_{1.4}$ as discussed. The bold curve segments indicate the NS mass interval of $1 < M/M_\odot < 2$. We also point out the

configurations at $1.4M_\odot$ with open squares. As shown, we may exclude the EOSs BOB and DBHF due to the condition $72 < \Lambda_{1.4} < 580$. This improves the prediction of $R_{1.4}$ to $11.6 \lesssim R_{1.4} \lesssim 12.9\,\mathrm{km}$. Note that hybrid stars are not shown here simply because the hybrid branches set in at high mass, above $1.7M_\odot$.

Interpretation of the GW170817 event also allowed to establish lower limits on the NS radius: The condition of (meta)stability of the produced hypermassive star after merger allowed to exclude very soft EOSs [159] and to set thus a lower limit on the radius, $R_{1.6} > 10.7\,\mathrm{km}$ [143], confirmed by similar recent analyses [161, 162] in which $R_{1.4} > (11.5 - 12)\,\mathrm{km}$. An even higher lower limit $R_{1.4} > 12.55\,\mathrm{km}$ [163] has been deduced from the measurement of the neutron skin of ^{208}Pb in the PREX experiment [164]. Simulations with several different EOSs set also a lower limit on the effective deformability Eq. (1.10), $\tilde{\Lambda}_{1.4} > 400$ [90], related to the black hole formation time and the accretion disk mass of material left out of the black hole. The latter was constrained from optical/infrared observations of the remnant AT2017gfo [165, 166, 167, 168, 169]. Small values of $\Lambda_{1.4}$ and therefore small values of R imply very fast black hole formation and little material left in the disk, which is incompatible with observation. A correlated lower limit $R_{1.4} \gtrsim 12\,\mathrm{km}$ is obtained in this way.

On the other hand, as discussed in Sec. 1.3.4, smaller radii than these lower limits were deduced from observations of thermal emission from accreting NSs in quiescent LMXBs. By analyzing their X-ray spectra, the observations seem to suggest for stars of mass about $(1.4 - 1.5)\,M_\odot$ a radius in the range $(9.9 - 11.2)\,\mathrm{km}$ [15]. Those results have been criticized in [170, 171, 172]: in particular the estimates of the radii are affected by the uncertainties of the composition of the atmosphere. If the atmosphere contains He, significantly larger radii are extracted. More recently [173] it was shown that when allowing for the occurrence of a first-order phase transition in dense matter (Model C), $R_{1.4}$ is smaller than 12 km to 95% confidence. However, $R_{1.4}$ could be larger if NSs have uneven temperature distributions. Clearly, no firm conclusions can yet be reached and we need to wait for new data such as the ones collected by the NICER mission, in order to obtain independent and precise information on NS radii.

We remark that this clash between large radii from GW170817 and

small radii from quiescent LMXBs (if confirmed) could be resolved in the two-families or twin-star scenarios, which we discuss in the following.

3.1.2 Modeling binary neutron star systems

In the case of an asymmetric binary system, $(M, R)_1 + (M, R)_2$, with mass asymmetry $q = M_2/M_1$, and known chirp mass

$$M_c = \frac{(M_1 M_2)^{3/5}}{(M_1 + M_2)^{1/5}}, \tag{3.6}$$

the effective deformability is given by

$$\tilde{\Lambda} = \frac{16}{13}\frac{(1+12q)\Lambda_1 + (q+12)\Lambda_2}{(1+q)^5} + (1 \leftrightarrow 2) \tag{3.7}$$

with

$$\frac{[M_1, M_2]}{M_c} = \frac{297}{250}(1+q)^{1/5}[q^{-3/5}, q^{2/5}]\,. \tag{3.8}$$

We remind that the analysis of the GW170817 event [3] provided the data $M_c/M_\odot = 1.188^{+0.004}_{-0.002}$ (corresponding to $M_1 = M_2 = 1.365\,M_\odot$ for a symmetric binary system), $q = M_2/M_1 = 0.7 - 1$ [corresponding to maximum asymmetry $(M_1, M_2) = (1.64, 1.15)\,M_\odot$], and $\Lambda_{1.4} < 580$, being discussed before, from the phase-shift analysis of the observed signal. The limit on $\tilde{\Lambda}$ was recently updated to $70 < \tilde{\Lambda} < 720$ [5]. A higher lower limit can be deduced, $\tilde{\Lambda} > 400$, combining with an analysis of the electromagnetic counterpart with kilonova [90]. In order to constrain EOSs with these observational data we model binary systems with the considered EOSs. The modeling of binary systems can be carried out in three different scenarios, that are one-family, two-families and twin-stars scenarios, based on the different types of component stars, see Table 3.2.

Let us start by constructing the standard one-family scenario assuming both NSs in the binary system are hadronic stars. We choose the same set of EOSs as shown in Fig. 3.2, i.e. BOB, V18, N93, UIX, DBHF, APR, LS220 and SFHO.

For the two-families scenario, the massive component star (M_1) is a strange-quark star, while the hadronic star is assumed to be the one with

Table 3.2: Three different scenarios for constructing a binary NS system. The considered EOSs for each type of star are shown.

Scenario	Heavy component M_1	Light component M_2
One family	Hadronic star (BOB, V18, N93, UIX, DBHF, APR, LS220, SFHO)	
Two families	Quark star (QS, QS2)	Hyperonic star (SFHO+HD,SFHO+HD2)
Twin stars	Hybrid star (DBHF+CS,DBHF+CS2)	Hadronic star (DBHF)

lower mass (M_2). In fact, here we consider the hadronic star as hyperonic NS, using the SFHO EOS with inclusion of delta resonances and hyperons (SFHO+HD) [174]. In particular, we consider two parameterizations corresponding to two different values for the coupling of the delta resonances with the sigma meson: $x_{\sigma\delta} = 1.15$ (SFHO+HD) and $x_{\sigma\delta} = 1$ (SFHO+HD2), while we set the couplings with the omega and the rho meson to $x_{\omega\delta} = x_{\rho\delta} = 1$. Concerning the quark matter EOS for the quark stars, we adopt a simple parametrization of a strange-quark-matter EOS (SQM) encoding both the non-perturbative phenomenon of confinement and the perturbative quark interactions [175]. Two parameter sets are considered: the set QS with $B_{\rm eff}^{1/4} = 137.5$ MeV and $a_4 = 0.7$ whose maximum mass is $M_{\rm max} = 2.1\,M_\odot$, and the set QS2 with $B_{\rm eff}^{1/4} = 142$ MeV and $a_4 = 0.9$ whose maximum mass is also $M_{\rm max} = 2.1\,M_\odot$

In the twin-star scenario, a constant-speed-of-sound EOS (DBHF+CS), which is characterised by the speed of sound c_s, the pressure $p_{\rm trans}$ and the discontinuity in energy density $\Delta\epsilon$ at the transition, has been applied to model hybrid stars. Here we take the results of [108] for the DBHF nucleonic EOS and we set $(p_{\rm trans}/\epsilon_{\rm trans},\ \Delta\epsilon/\epsilon_{\rm trans},\ c_s^2)$ =(0.1, 1, 1) and (0.095, 0.0, 2/3) for the comparison. One needs to choose a speed of sound saturating the causal limit, because with more normal values it is impossible to obtain $M_{\rm max} \geq 2\,M_\odot$ and $R_{1.4} \leq 12\,$km. Still a strong fine-tuning of the parameters is needed in order to satisfy all constraints.

In Fig. 3.3 we display the mass-radius relations for the EOSs here

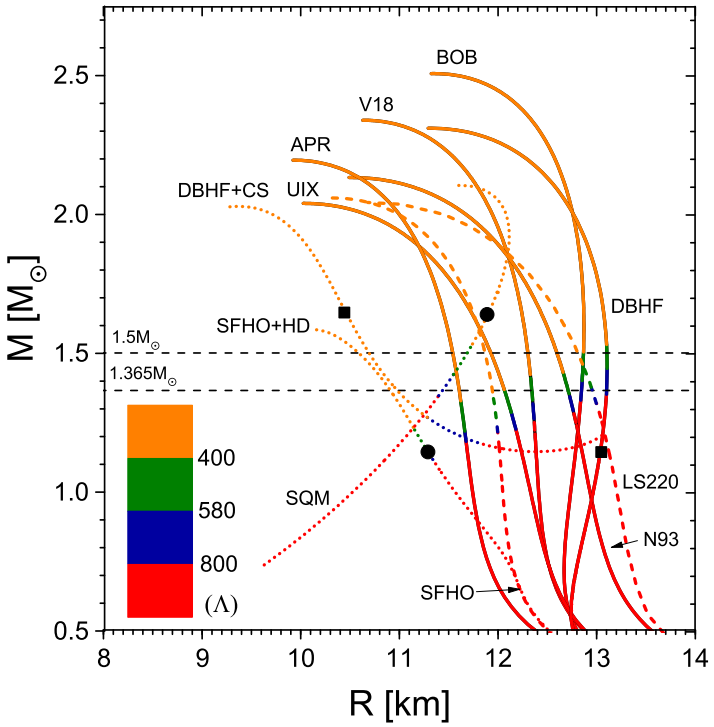

Figure 3.3: Mass-radius relations for different EOS, indicating also values of the tidal deformability Λ. Solid (dashed) curves for microscopic (phenomenological) EOS, see text. Markers indicate the $q = 0.7$ configurations for the two-families (●) and twin-star (▪) scenarios. From Ref. [176].

adopted and we encode also the information on the tidal deformabilities. Assuming that GW170817 was a symmetric system, one can convert the constraint of $400 < \tilde{\Lambda} < 720$ [5] into $400 < \Lambda_{1.365} < 720$, which predicts $12\,\mathrm{km} \lesssim R_{1.5} \lesssim 13\,\mathrm{km}$, in agreement with the analysis of [144].

Note that the chosen hyperonic EOSs do not satisfy the two-solar-mass limit, in particular SFHO-HD with a small maximum mass $M_{\mathrm{max}} \approx 1.6\,M_{\odot}$ and a compact configuration, $R_{1.5} < 11\,\mathrm{km}$. Such EOSs would be excluded within the standard one-family scenario in which all compact stars belong to the same family: in that scenario there is a one-to-one correspondence between the mass-radius relation and the EOS. However, they are allowed if one adopts the two-families scenario in which the heaviest stars

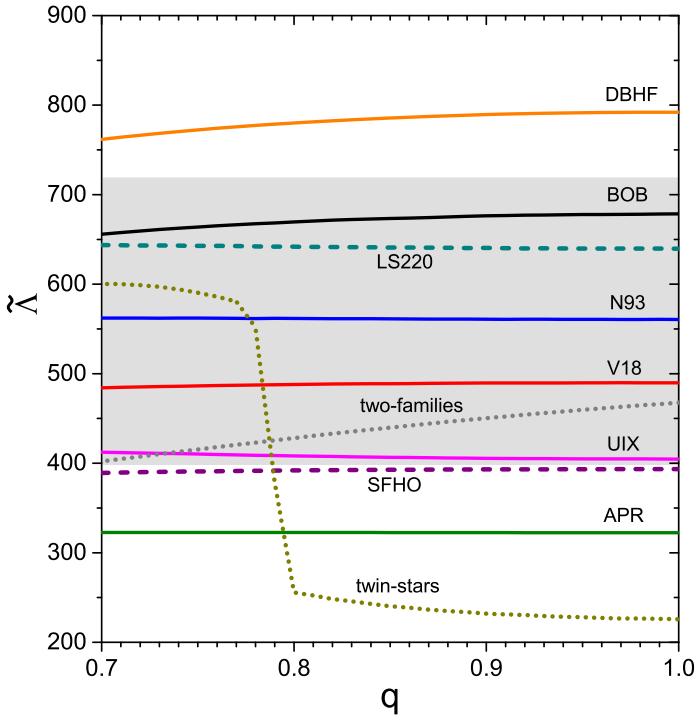

Figure 3.4: Effective deformability $\tilde{\Lambda}$, Eq. (3.7), vs. mass asymmetry $q = M_2/M_1$ for a binary NS system with fixed chirp mass $M_c = 1.188 M_\odot$ for different EOS. The shaded area is constrained by the GW170817 event interpretation [5]. From Ref. [176].

are interpreted as quark stars, whereas the lighter and smaller stars are hadronic stars [177, 178, 179, 180].

To constrain the EOS by the data of the event GW170817, we fix now the chirp mass $M_c = 1.188\, M_\odot$ and compute $\tilde{\Lambda}$, Eq. (3.7), as a function of mass asymmetry $q = M_2/M_1$ ($q = 0.7 - 1$), corresponding to a maximum asymmetry $(M_1, M_2) = (1.64, 1.15) M_\odot$. The results are displayed in Fig. 3.4. The one-family EOSs predict an effective deformability nearly independent of asymmetry q, while there is a strong dependence for the radii-asymmetric two-families and twin-star constructions. We remind that when calculating $\tilde{\Lambda}$ within the two-families scenario, we assume that the binary system is a mixed system with a light hyperonic star and a

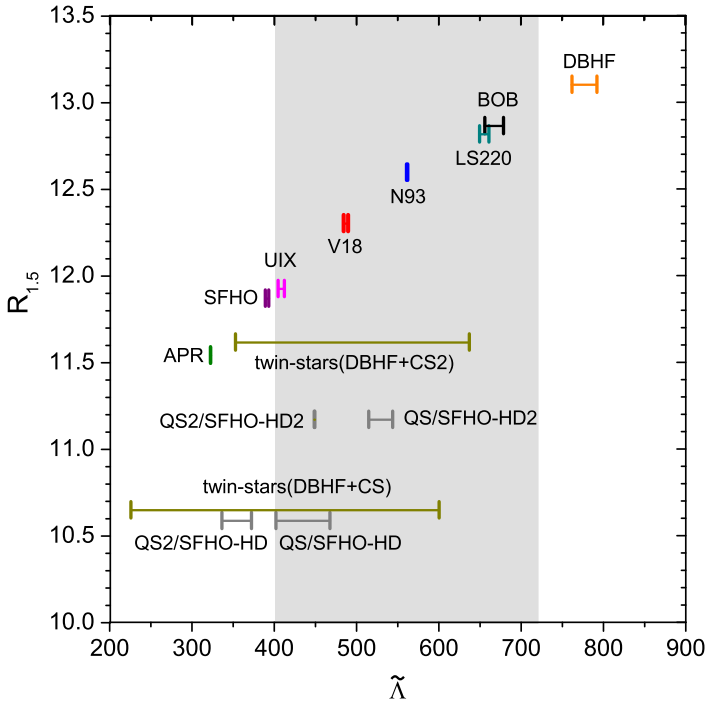

Figure 3.5: Smaller $R_{1.5}$ radius of an asymmetric binary NS system and possible range of $\tilde{\Lambda}$ with fixed chirp mass $M_c = 1.188 M_\odot$ and varying $q = 0.7 - 1$ for different EOS. From Ref. [176].

heavy quark star. Similarly, within the twin-stars scenario we assume that the most massive star is the hybrid star, see Table 3.2. The configurations corresponding to maximum asymmetry $q = 0.7$ are indicated by markers in Fig. 3.3 for both scenarios. In particular the twin-star configuration features a very large radial asymmetry in this case: $(R_1, R_2) = (10.7, 13.0)$ km, which allows to achieve concurrently a very small radius R_1 and a sufficiently large $\Lambda_{1.4} \approx 600$. Notice that in both of these scenarios, a non-negligible dependence of Λ on q is found.

In Fig. 3.5, we display for the different EOSs here adopted the correlation between the possible values of $\tilde{\Lambda}$ (for fixed $M_c = 1.188 M_\odot$ and varying q in the range $0.7 - 1$) and $R_{1.5}$. In the case of the two-families or twin-stars scenarios $R_{1.5}$ denotes the radius of the most compact component. Within

the one-family scenario, one observes a very tight correlation between $R_{1.5}$ and $\tilde{\Lambda}_{1.4}$, where all the EOSs which fulfill the constraint $\tilde{\Lambda}_{1.4} > 400$ from [90] lead to $R_{1.5} > 11.8\,\mathrm{km}$. This feature is violated if a second branch of compact stars exists, as in the case of the two families or of the twin stars. Moreover, for some choice of the parameters, it is possible to satisfy $\tilde{\Lambda}_{1.4} > 400$ and obtain stellar configurations with $R_{1.5}$ significantly smaller than 12 km.

Within the twin-stars scenario, an extremely detailed parametric analysis was already performed in [108] by using the nucleonic EOSs DBHF and BHF [138]. There, it was stressed that to obtain $R_{1.5}$ smaller than 12 km, c_s^2 must be significantly larger than one third. In Fig. 3.5, we have implemented an example (DBHF+CS2) for which $R_{1.5} = 11.6\,\mathrm{km}$, obtained by fixing $c_s^2 = 2/3$. To reach smaller values of $R_{1.5}$, even larger sound speeds should be assumed. In the causal limit, $c_s^2 = 1$, one obtains $R_{1.5} = 10.7\,\mathrm{km}$. We have considered here only the nucleonic EOS DBHF because BHF is a rather soft EOS, and it would not be possible to satisfy the limit $\tilde{\Lambda} > 400$. In conclusion, the twin-stars scenario allows one to reach radii smaller than 12 km while satisfying the limit on $\tilde{\Lambda}$, only for a very small parameter space.

Conversely, for the two-families scenario, the parameter space is larger. We can fulfill the limit $\tilde{\Lambda} > 400$ with both the hadronic EOSs SFHO+HD and SFHO+HD2, which lead to $R_{1.5} = 10.6\,\mathrm{km}$ and to $R_{1.5} = 11.2\,\mathrm{km}$, respectively. Only when combining the soft hadronic EOS SFHO+HD with the soft quark EOS QS2, the limit on $\tilde{\Lambda}$ is not satisfied. Notice that in both quark EOSs $c_s^2 \sim 1/3$.

Let us now compare the two-families and twin-stars scenarios. In the two families, the low-mass objects are made of hadrons and the presence of delta resonances and/or hyperons allows one to reach small radii (and very small values of Λ) for masses in the range $(1.4\text{–}1.5)M_\odot$. The more massive stars are instead quark stars and their radii are not extremely small (their Λ has an intermediate value). In the twin-stars scenario, the low-mass objects are made of nucleons and have large radii and large Λ, while the most massive stars are hybrid stars with a very large quark content and small radii and Λ. Note how in both these scenarios the GW170817 event needs to be interpreted as a "mixed case", in which one of the objects is made only of hadrons and the other contains de-

confined quarks. While these two scenarios are both able to interpret the GW170817 event and to have very small values for $R_{1.5}$, the differences in their mass–radius relation and composition will provide different and testable outcomes for the three cases of mergers they are able to produce: hyperonic star - hyperonic star, hyperonic star - quark star, and quark star - quark star in the case of the two-families and hadronic star-hadronic star, hadronic star-hybrid star, and hybrid star-hybrid star in the case of the twin-stars. For instance, in the case of a merger of two light compact stars, e.g., $1.2M_\odot + 1.2M_\odot$, the twin-stars scenario predicts very large values of $\tilde{\Lambda}$, while for the two-families scenario, $\tilde{\Lambda}$ is significantly smaller. This difference can easily be tested both through the GW signal and through the kilonova.

3.2 Hints from the nuclear symmetry energy

It is very important that any property of the adopted EOS can be tested at the saturation density $\rho_0 \approx 0.17\,\mathrm{fm}^3$ of symmetric nuclear matter (SNM) [$N = Z$, being $N(Z)$ the neutron (proton) number], where information from laboratory data on finite nuclei is available. In general, in the vicinity of the saturation point the binding energy per nucleon can be expressed in terms of the density parameter $x \equiv (\rho - \rho_0)/3\rho_0$ and the asymmetry parameter $\delta \equiv (N - Z)/(N + Z)$ as

$$E(\rho, \delta) = E_{\mathrm{SNM}}(\rho) + E_{\mathrm{sym}}(\rho)\delta^2, \tag{3.9}$$

$$E_{\mathrm{SNM}}(\rho) = E_0 + \frac{K_0}{2}x^2, \tag{3.10}$$

$$E_{\mathrm{sym}}(\rho) = S_0 + Lx + \frac{K_{\mathrm{sym}}}{2}x^2, \tag{3.11}$$

where K_0 is the incompressibility, $S_0 \equiv E_{\mathrm{sym}}(\rho_0)$ is the symmetry energy coefficient at saturation, and the parameters L and K_{sym} characterize the density dependence of the symmetry energy around saturation. The incompressibility K_0 gives the curvature of $E(\rho)$ at $\rho = \rho_0$, whereas S_0 determines the increase of the energy per nucleon due to a small asymmetry δ. These parameters are defined as

$$K_0 \equiv 9\rho_0^2 \frac{d^2 E_{\rm SNM}}{d\rho^2}(\rho_0)\,, \tag{3.12}$$

$$S_0 \equiv \frac{1}{2}\frac{\partial^2 E}{\partial \delta^2}(\rho_0, 0) \approx E_{\rm PNM}(\rho_0) - E_{\rm SNM}(\rho_0)\,, \tag{3.13}$$

$$L \equiv 3\rho_0 \frac{dE_{\rm sym}}{d\rho}(\rho_0)\,, \tag{3.14}$$

$$K_{\rm sym} \equiv 9\rho_0^2 \frac{d^2 E_{sym}}{d\rho^2}(\rho_0)\,. \tag{3.15}$$

Properties of the various considered EOSs are listed in Table 3.3, namely, the value of the saturation density ρ_0, the binding energy per particle E_0, the incompressibility K_0, the symmetry energy S_0 [note that we use the second definition involving the energy of pure neutron matter (PNM) for the values in the table], and its derivative L at ρ_0. The curvature of the symmetry energy $K_{\rm sym}$ is only loosely known to be in the range of $-400\,{\rm MeV} \lesssim K_{\rm sym} \lesssim 100\,{\rm MeV}$ [181, 182], and therefore will not be examined in the following. In Table 3.3 we have also included the experimental ranges for the nuclear parameters and the data available so far from astrophysical observations.

We notice that all the adopted EOSs agree fairly well with the empirical values. Marginal cases are the slightly too low E_0 and K_0 for V18, too small/large S_0 for LS220/N93, and too low K_0 for UIX and FSS2GC. The L parameter does not exclude any of the EOSs.

An important test for the EOS has to do with the symmetry energy, for which the experimental constraints are abundant at saturation density (see, e.g., [187, 188, 189]). We show in Fig. 3.6 a set of different experimental constraints together with the values of (S_0, L) predicted by the various theoretical models considered in this paper. More in detail,
– the label “HIC" (blue region) corresponds to the constraints inferred from the study of isospin diffusion in heavy ion collisions (HICs) [190];
– the label “Polarizability" (violet region) represents the constraints on the electric dipole polarizability deduced in [191];
– the label “Sn neutron skin" (grey region) indicates the constraints deduced from the analysis of neutron skin thickness in Sn isotopes [192];

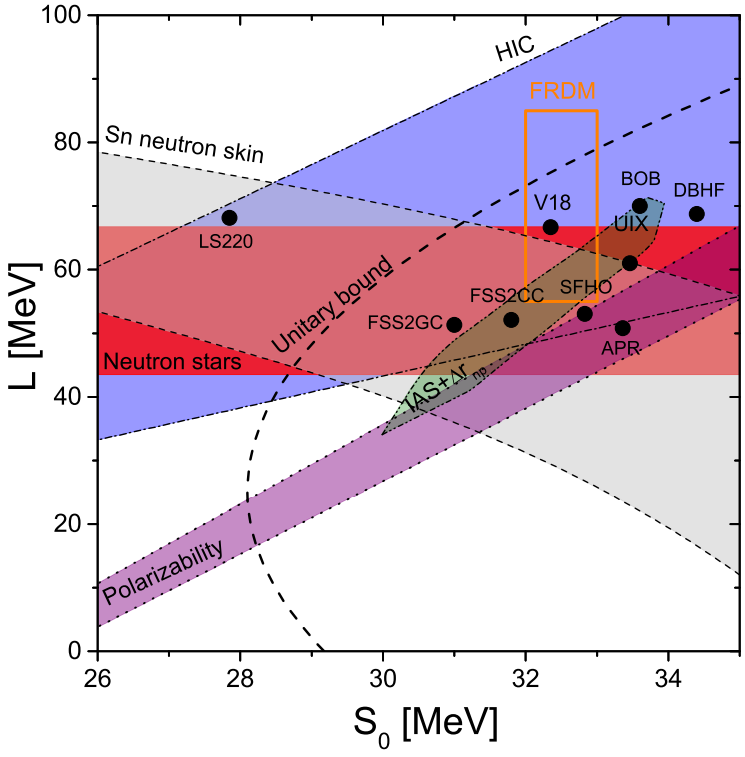

Figure 3.6: Correlations between symmetry energy S_0 and its slope L at the saturation density. The markers represent the predictions of the considered EOSs. See text for details on the various constraints. From Ref. [105].

– the label "FRDM" (rectangle) corresponds to the values of S_0 and L inferred from finite-range droplet mass model calculations [193];
– the label "IAS $+\Delta r_{\rm np}$" (green diagonal region) indicates the isobaric-analog-state (IAS) phenomenology combined with the skin-width data, and represents simultaneous constraints by Skyrme-Hartree-Fock calculations of the IAS and the ^{208}Pb neutron-skin thickness [194];
– the horizontal band (in red color) labeled "Neutron stars" is obtained from a Bayesian analysis of mass and radius measurements of NSs by considering the 68% confidence values for L [195];
– the dashed curve is the unitary gas bound on symmetry energy parameters derived in Ref. [181]: only values of (S_0, L) to the right of the curve

Table 3.3: Saturation properties and NS observables predicted by the considered EOSs. See text for details. From [105].

EOS	$\rho_0[\mathrm{fm}^3]$	$-E_0$[MeV]	K_0[MeV]	S_0[MeV]	L[MeV]
BOB	0.170	15.4	238	33.7	70
V18	0.178	13.9	207	32.3	67
N93	0.185	16.1	229	36.5	77
UIX	0.171	14.9	171	33.5	61
FSS2CC	0.157	16.3	219	31.8	52
FSS2GC	0.170	15.6	185	31.0	51
DBHF	0.181	16.2	218	34.4	69
APR	0.159	15.9	233	33.4	51
LS220	0.155	15.8	219	27.8	68
SFHO	0.157	16.2	244	32.8	53
Exp.	$\sim$ 0.14–0.17	$\sim$ 15–16	220–260	28.5–34.9	30–87
Ref.	[183]	[183]	[184, 185]	[95, 186]	[95, 186]

are permitted.

All considered constraints are not simultaneously fulfilled in any area of the parameter space, and this is probably due to the model dependencies that influence the derivation of constraints from the raw data, besides the current uncertainties in the experimental measurements. Given this situation, at the moment no definitive conclusion can be drawn and, except for models predicting values of the symmetry energy parameters outside the limits given in Table 3.3 (like the LS220 or the N93 EOS), no theoretical models can be ruled out a priori on this basis.

A further crucial point in the understanding of the nuclear symmetry energy is its high-density behavior, which is among the most uncertain properties of dense neutron-rich matter. Its accurate determination has significant consequences in understanding not only the reaction dynamics of heavy-ion reactions, but also many interesting phenomena in astrophysics, such as the explosion mechanism of supernovae and the properties of NSs. In fact several aspects of the NS structure and dynamics depend crucially on the symmetry energy, e.g., the composition and the

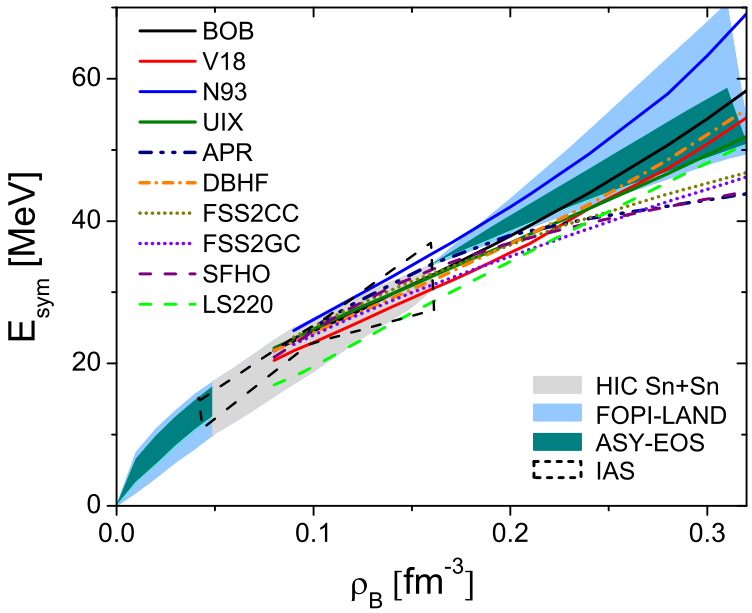

Figure 3.7: Symmetry energy vs. baryon density for all considered EOSs. The blue, green, and grey bands, as well as the dashed box, represent experimental data as described in the text. From Ref. [105].

onset of the direct Urca cooling reaction, which is a threshold process dependent on the proton fraction controlled by the symmetry energy. This will be discussed in Sec. 5.1.1.

A big experimental effort has been devoted during the last few years to constrain the high-density symmetry energy using various probes in HICs at relativistic energies. Fig. 3.7 displays some constraints deduced for the density dependence of the symmetry energy from the ASY-EOS data [196] (green band) and the FOPI-LAND result [197] (blue band) as a function of the density. The results of Ref. [190] are reported in the grey area (HIC Sn+Sn), whereas the dashed contour labeled by IAS shows the results of Ref. [194]. We observe that the experimental results exhibit a monotonically increasing behavior with increasing density, and that several microscopic EOSs turn out to be compatible with experiments, except LS220 around saturation density, whereas N93, FSS2CC, and FSS2GC above the saturation density are only marginally compatible with the data.

3.3 Correlations between neutron-star and nuclear-matter observables

The extraction of the gross properties of the nuclear EOS from HICs data has been one of the main objectives in terrestrial nuclear experiments in the last two decades. In fact HICs at energies ranging from few tens to several hundreds MeV per nucleon produce heavily compressed nuclear matter with subsequent emission of nucleons and fragments of different sizes. The experimental analysis has been performed using the transverse flow as an observable, since it strongly depends on the pressure developed in the interaction zone of the colliding nuclei at the moment of maximum compression. The fireball density reached during the collision can also be probed by subthreshold K^+ production, since this depends on its incompressibility, as shown by the data collected by the KaoS collaboration [198]. A combined flow and kaon production analysis was presented in Ref. [199], where a region in the pressure vs. density plane was identified, through which a compatible EOS should pass.

That analysis is displayed in Fig. 3.8 (left panels) as a grey box for the flow data by the FOPI collaboration [201], and as a brown box for the KaoS collaboration [198]. Those results point in the direction of a soft EOS, with values of the incompressibility in the range $180 \leq K \leq 250$ MeV close to the saturation density. We observe that almost all considered EOSs are compatible with the experimental data, except the BOB, V18, and DBHF EOS, which are too stiff at large density, where the analysis could however be less reliable due to the possible appearance of other degrees of freedom besides nucleons. Such densities are actually never reached in HICs. For completeness, we display in the central panels (b) the pressure for the PNM case.

The EOS governs also the dynamics of NS mergers. In fact, the possible scenarios of a prompt or delayed collapse to a black hole or a single NS, following the merger, do depend on the EOS, as well as the amount of ejected matter which undergoes nucleosynthesis of heavy elements. During the inspiral phase, the EOS strongly affects the tidal polarizability Λ, Eq. (3.1). The first GW170817 analysis for a 1.4 $M_\odot$ NS [3] gave an upper limit of $\Lambda_{1.4} < 800$, which was later improved to $\Lambda_{1.4} = 190^{+390}_{-120}$

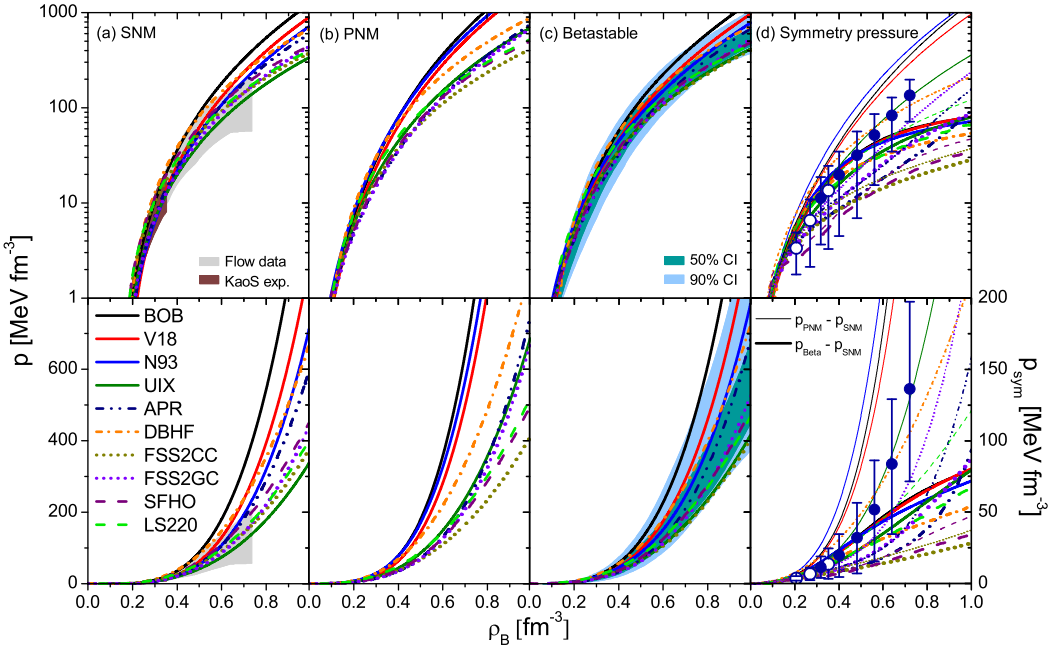

Figure 3.8: Pressure vs. baryon density for the considered EOSs on a logarithmic (upper row) or linear (lower row) scale for (a) symmetric matter, (b) pure neutron matter, (c) beta-stable matter, and (d) the symmetry pressure. In (a) constraints derived from HICs data are reported as brown band (KaoS experiment) and grey band (Flow data). In (c) the GW170817 constraints [4] are reported. The markers in (d) are from the data analysis of Ref. [200]. The thick curves represent the compatible quantity $p_\beta - p_{\rm SNM}$, whereas the actual symmetry pressure $p_{\rm PNM} - p_{\rm SNM}$ is shown by thin curves. See text for more details. From Ref. [105].

by assuming that both NSs feature the same EOS [4]. In this new analysis, the values of the pressure as a function of density were extracted, and those are displayed as colored areas in Fig. 3.8(c), in which the blue (green) shaded region corresponds to the 90% (50%) posterior confidence level. We notice that almost all EOSs turn out to be compatible with the GW170817 data at density $\rho > 2\rho_0$, with BOB in marginal agreement at large density. This constraint combined with the recent observation of the new maximum mass $M = 2.14^{+0.10}_{-0.09}\, M_\odot$ of PSR J0740+6620 [74] represents at the moment the strongest test for any EOS model. In our case, the V18 EOS appears the most compatible with both data sets. This point has also

been discussed in the framework of phenomenological EOSs [202], where the combined data help to constrain the range of values of the stiffness of isospin-symmetric nuclear matter. A further comparison of HIC data with GW observations can be found in Ref. [203].

Another interesting quantity to consider is the so-called symmetry pressure,

$$p_{\rm sym}(\rho) = \rho^2 \frac{dE_{\rm sym}(\rho)}{d\rho} \approx p_{\rm PNM}(\rho) - p_{\rm SNM}(\rho)\,, \tag{3.16}$$

[the last equation is valid in the case of the quadratic approximation Eq. 3.9], which adds to the pressure of an isospin-symmetric system with $N = Z$. Its contribution is very important because it is related to the poorly known symmetry energy at large density, and plays a big role in the determination of the proton fraction, for instance, crucial for NS cooling simulations. More precisely, the pressure of beta-stable matter (including electrons) with asymmetry $\delta(\rho) = (\rho_n - \rho_e)/\rho$ is given by [202, 204, 205]

$$p_\beta(\rho) = p_{\rm SNM}(\rho) + \delta^2 p_{\rm sym}(\rho) + \frac{\delta(1-\delta)}{2}\rho E_{\rm sym}(\rho)\,. \tag{3.17}$$

For small electron fractions one has $\delta \approx 1$ and

$$p_{\rm sym} \approx p_\beta - p_{\rm SNM}\,. \tag{3.18}$$

This quantity is displayed in Fig. 3.8(d) using thick curves. The markers with error bars are the corresponding results of the analysis performed in Ref. [200], where a subtraction procedure has been proposed between the kaon data (white dots) and flow data (blue dots) for SNM, both displayed in panel (a), and the GW170817 event constraints shown in panel (c), assuming matter in beta-stable condition. We see that the symmetry pressure increases rapidly with the baryon density, as many microscopic EOSs predict, except at densities above $\rho \gtrsim 0.7\,{\rm fm}^3$, where most EOSs show a saturating behavior and thus a different trend with respect to the analysis of the (Flow) data. However, such high densities are never actually reached in HICs.

We also point out that the true symmetry pressure $p_{\rm sym} \approx p_{\rm PNM} - p_{\rm SNM}$ [thin curves in Fig. 3.8(d)] can be substantially larger than the approxi-

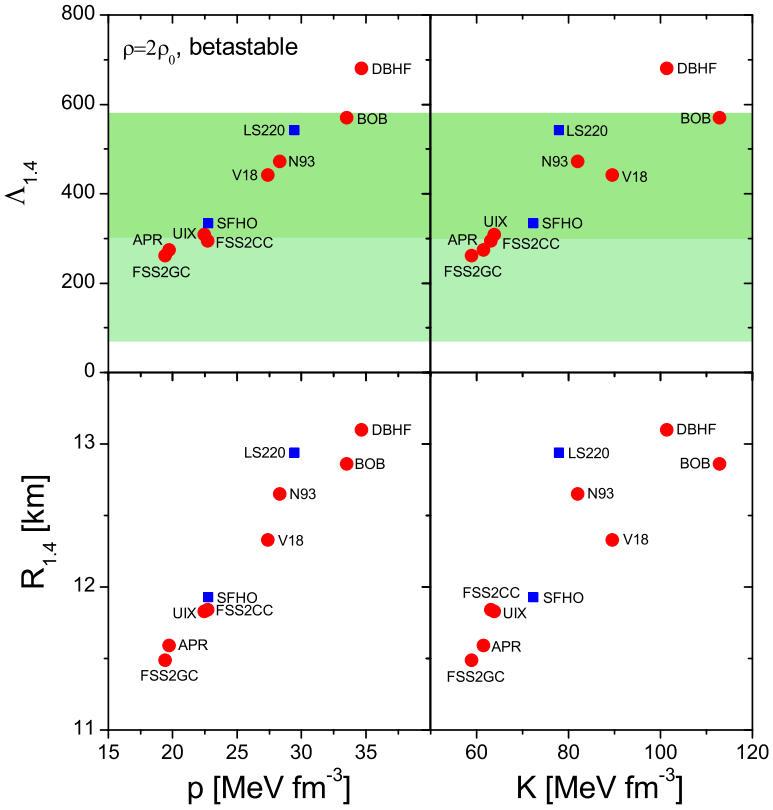

Figure 3.9: Tidal deformability (upper panels) and radius (lower panels) of a 1.4 $M_\odot$ NS vs. the pressure (left panels) and the incompressibility K (right panels) of beta-stable matter at twice the saturation density. The light and dark shaded bands in the upper row represent the limits derived in [4, 91], respectively. From Ref. [105].

mation Eq. (3.18), if one takes properly into account the EOS for PNM, which is significantly stiffer than the beta-stable EOS for most considered models, compare Figs. 3.8(b) and (c).

We just discussed both nuclear matter and neutron-star observables constraints on the pressure of symmetric nuclear matter and of beta-stale matter, respectively, and the connection of these two pressures. In order to better understand the properties of nuclear matter, it would be very interesting to find correlations between GW170817 observations on NS properties and microscopic constraints from nuclear measurements, as the ones just discussed. For this purpose, the limits derived for the tidal deformability could be very valuable.

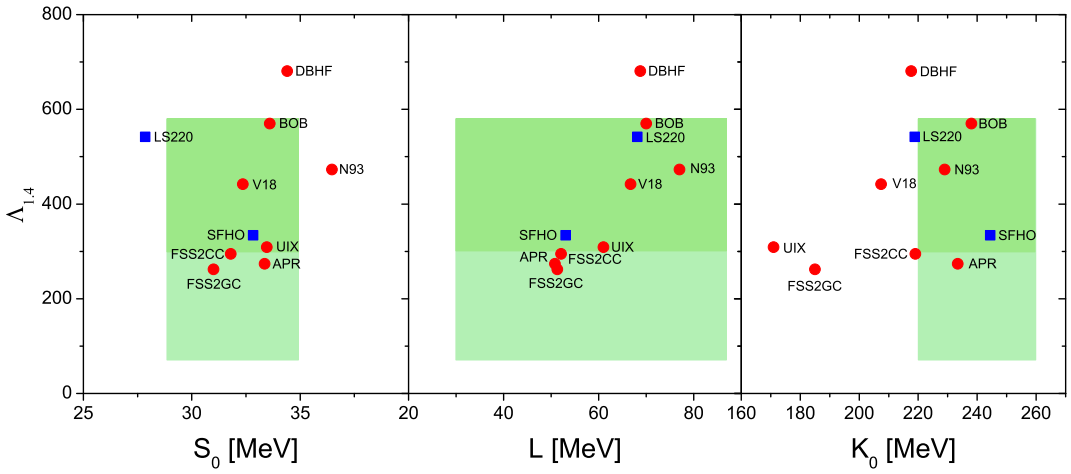

Figure 3.10: The tidal deformability of a 1.4 $M_\odot$ NS as a function of the symmetry energy S_0 (left panel), its derivative L (middle panel), and the incompressibility K_0 at saturation density ρ_0 for all the considered EOSs. The shaded areas represent the limits listed in Table 3.3. From Ref. [105].

We now turn to the discussion of our results. In Ref. [204] it was found that for a wide choice of nuclear EOSs the NS radius is strongly correlated with the pressure of beta-stable matter $p = \rho^2 dE_\beta/d\rho$ at a density $\rho \approx 2\rho_0$. According to the previous discussion this correlation is then also valid between $\Lambda_{1.4}$ and pressure. This is also confirmed for our set of EOSs as shown in Fig. 3.9 (left panels), whereas weaker correlations appear with the incompressibility $K = 9\rho^2 d^2E_\beta/d\rho^2$ under the same conditions, displayed in the right panels.

For completeness, we have calculated the correlation factors

$$r(x,y) = \frac{1}{n-1}\frac{\sum_x \sum_y (x-\bar{x})(y-\bar{y})}{s_x s_y}, \tag{3.19}$$

where n is the number of data pairs, $\bar{x}$ and $\bar{y}$ are the sample means of all the x and y values, respectively; and s_x and s_y are their standard deviations. In our case the results are

$$r(p,\Lambda_{1.4}) = 0.982\,, \qquad r(p,R_{1.4}) = 0.971\,, \tag{3.20}$$

$$r(K,\Lambda_{1.4}) = 0.885\,, \qquad r(K,R_{1.4}) = 0.846\,, \tag{3.21}$$

which confirm the above statements, i.e., stronger (weaker) correlations among pressure p, $\Lambda_{1.4}$, and $R_{1.4}$ (K, $\Lambda_{1.4}$, and $R_{1.4}$).

The green bands displayed in the upper panels represent the limits on $\Lambda_{1.4}$ derived in [4, 91]; in particular the lower limits, i.e., $\Lambda_{1.4} = 190^{+390}_{-120}$ [4] (light green) and $\Lambda_{1.4} > 300$ [91, 92] (dark green), are important for the determination of the radius, which corresponds to $R_{1.4} = 11.9^{+1.4}_{-1.4}$ km in the former case, and $R_{1.4} = 12.2^{+1.0}_{-0.8} \pm 0.2$ km in the latter one. For completeness, we have checked whether this correlation applies also to NS masses different from 1.4 $M_\odot$, but it becomes slightly weaker with increasing NS masses. Thus the determination of the tidal deformability or the NS radius could put constraints on the pressure and the symmetry pressure at twice the saturation density [204, 142], or vice versa. The current limits exclude only the DBHF EOS due to its too high $\Lambda_{1.4}$ value.

Following the same method, we have tried to find correlations between NS observables and properties of SNM around saturation density. Results are displayed in Fig. 3.10 (the green bands display the same conditions as in Fig. 3.9), where the tidal deformability of a 1.4 $M_\odot$ NS is reported as a function of the symmetry energy S_0 (left panel), its slope L (middle panel), and the incompressibility K_0 (right panel), all taken at saturation density. Apparently no evident correlations between the tidal deformability and S_0 and K_0 do exist, whereas some degree of correlation is found with L, as confirmed by the corresponding correlation factors

$$r([S_0, K_0, L], \Lambda_{1.4}) = [0.128, 0.300, 0.808] \,. \tag{3.22}$$

Similar results were found also in Refs. [206, 207, 208, 209], with several EOSs based on the RMF model and the Skyrme-Hartree-Fock approach.

Chapter 4

The essential physics of neutron star cooling

As introduced in Chapter 1, the study of the cooling behavior of NSs is a possible way to constrain the EOS. In the following of this thesis, we study the cooling evolution of NS applying the microscopic EOSs, which have been tested in the previous chapter by various constraints from astrophysical observations and terrestrial nuclear experiments, and discuss the constraints from the cooling observations on EOSs. While computing mass, radius and tidal deformability of NSs requires only a known relation between total pressure and total energy density, the simulation of NS cooling depends on a detailed description of interior composition which determines the heat transport and amount of neutrino emission. Furthermore, the possible presence of a superfluid, which barely affects the structure of NS, is important to the NS cooling.

In this chapter, we briefly introduce the simulation of the cooling evolution, which is dominated by the thermal balance equation and thermal transport equation, and some key ingredients in cooling simulations such as neutrino emission and the presence of pairing gaps. The NSCOOL code [210], employed for performing cooling simulation, is introduced in the last section.

4.1 Equations of thermal evolution

The cooling evolution of a spherically symmetric NS can be characterized by two equations: the equation of thermal balance and the equation of thermal transport.

For a spherical shell in the star, the change of thermal energy is caused by the neutrino emission, heat flux passing through the surface and the possible heating sources, for example, by converting magnetic or rotational energy into thermal energy [21]. This gives the thermal balance equation

$$\frac{1}{4\pi r^2 e^{2\Phi}}\sqrt{1-\frac{2Gm}{r}}\frac{\partial}{\partial r}(e^{2\Phi}L_r) = -Q_\nu + Q_h - \frac{C_v}{e^{\Phi}}\frac{\partial T}{\partial t}, \tag{4.1}$$

where Φ is the metric function, m is the gravitational mass enclosed inside the sphere of radius r, Q_ν and C_v are the neutrino emissivity and the specific heat capacity, the term Q_h stands for all heating sources. The local luminosity L_r is defined as the non-neutrino heat flux passing through the surface of a spherical shell, as shown in Fig. 4.1. Since the heat flux is transported through thermal conduction, one can write the equation of thermal transport as

$$\frac{L_r}{4\pi\kappa r^2} = -\sqrt{1-\frac{2Gm}{r}}e^{-\Phi}\frac{\partial}{\partial r}(Te^{\Phi}), \tag{4.2}$$

where κ is the thermal conductivity. Obviously, Eqs. 4.1 and 4.2 are partial differential equations for luminosity L_r and temperature T. Both L_r and T depend on the radial coordinate r and time t. One has to solve these two equations in order to obtain $L(r,t)$ and $T(r,t)$. On the surface, luminosity and temperature can be connected by the Planck law $L_\gamma = L_r(R,t) = 4\pi\sigma_B R^2 T_s^4(t)$, where L_γ and T_s are photon luminosity and effective temperature, respectively. From astrophysical observation, observable quantities are apparent photon luminosity L_γ^∞ and apparent effective surface temperature T_s^∞, defined as

$$L_\gamma^\infty = L_\gamma(1-2GM/R) = 4\pi\sigma(T_s^\infty)^4 R_\infty^2, \tag{4.3}$$

$$T_s^\infty = T_s\sqrt{1-2GM/R}, \tag{4.4}$$

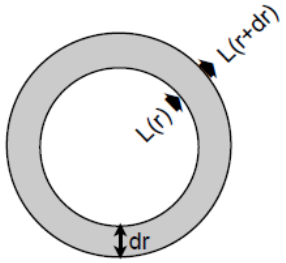

Figure 4.1: Schematic diagram of heat transport in the spherically symmetric star.

where $R_\infty = R/\sqrt{1-2GM/R}$ is the apparent radius. Hence, by solving Eqs. 4.1 and 4.2, one can obtain the dependence of the apparent photon luminosity L_γ^∞ (or of T_s^∞) on the stellar age t. This is the main goal of the cooling theory.

4.2 Neutrino emissivity

NSs are born with about 10^{11} K and cool down via neutrino emission from the core. This process will last several thousand years before the photon emission dominates the cooling where the NSs are already hard to be observed. So the possible channels of neutrino processes in the NS core are important to the cooling of NSs.

The most powerful process in nuclear matter (composed of n, p and e) is the Direct Urca (DU) process,

$$n \to p + e^- + \bar{\nu}_e \qquad \text{and} \qquad p + e^- \to n + \nu_e, \tag{4.5}$$

which is actually the neutron β decay and inverse reaction in thermal equilibrium. The derivation of the emission rate Q^{DU} of the DU process has been carried out in Ref. [2], and the result is given as

$$\begin{aligned} Q^{(DU)} &= \frac{457\pi}{10080} G_F^2 \cos^2\theta_C (1+3g_A^2) \frac{m_n^* m_p^* m_e^*}{\bar{h}^{10} c^3} (k_B T)^6 \Theta_{npe} \\ &\approx 4.0\times 10^{27} (\frac{n_e}{n_0})^{1/3} \frac{m_n^* m_p^*}{m_n^2} T_9^6 \Theta_{npe}\, \mathrm{erg cm^{-3} s^{-1}}, \end{aligned} \tag{4.6}$$

where G_F is the weak coupling constant, θ_c is the Cabibbo angle ($\cos\theta_c^2 \approx 0.948$), m_i^* $(i = n, p, e)$ is the effective particle mass, m_n the bare neutron mass, n_e electron number density, n_0 is the saturation number density, T_9^6 is the temperature in the unit of 10^9 K and Θ_{npe} is the step function, equals to 1 if the momentum conservation law is satisfied for the reactions, and $\Theta_{npe} = 0$ otherwise. This requires the proton fraction to be larger than $\sim 13\%$. The threshold value would be slightly higher if the muon appears also.

We notice that the effective nucleon mass, in principle, should be calculated from the same microphysical interaction as employed for the EOS. In the BHF approach, the effective masses can be expressed self-consistently in terms of the s.p. energy $e(k)$,

$$\frac{m^*}{m} = \frac{k}{m}\Big[\frac{de(k)}{dk}\Big]^{-1}. \tag{4.7}$$

The influence of the effective mass on neutrino emission rates has been evaluated in Ref. [211]. However, as suggested in Ref. [61], the effect can be absorbed into a rescaling factor of the pairing gaps that we also considered in cooling simulation, and therefore we simply use the bare nucleon mass here.

When the DU process is forbidden, due to a too low proton fraction or the presence of superfluidity, the main contribution to the cooling comes from less efficient neutrino processes such as modified Urca process (MU), the bremsstrahlung (BS) and the Cooper pair formation process (PBF) appearing in a superfluid. The emissivities of these processes are summarized in Table 4.1. A detailed description of these reactions, including the emissivity and its derivation, can be found in Ref. [2].

Similar to nuclear matter, the most powerful neutrino emission from quark matter is also the DU process via the direct and inverse β decay [212, 2, 20]. As quark matter consists of deconfined u, d, s quarks with an admixture of leptons, there are three possible branches of quark DU

reactions of interest for neutrino emission:

$$d \to u + e^- + \bar{\nu}_e \qquad \text{and} \qquad u + e^- \to d + \nu_e\,, \tag{4.8}$$

$$s \to u + e^- + \bar{\nu}_e \qquad \text{and} \qquad u + e^- \to s + \nu_e\,, \tag{4.9}$$

$$s \to d + e^- + \bar{\nu}_e \qquad \text{and} \qquad d + e^- \to s + \nu_e\,. \tag{4.10}$$

However, the sd branch is prohibited by the mechanism proposed by Glashow [212], and only the ud and us branches give contributions to the neutrino emission.

Let us start with reactions of the ud branch. u and d quarks are relativistic particles so that their mass can be neglected. If we treat these quarks as free particles, one would immediately obtain $p_{F_d} = p_{F_u} + p_{F_e}$ in terms of the beta-stable conditions, $\mu_d = \mu_s = \mu_u + \mu_e$. This basically suppresses the reactions of the ud branch because they would be allowed only if u and e were emitted in the same direction. Accordingly, it is necessary to take into account interactions between quarks. In fact, deconfined quarks are not completely free but coupled in the core of NS. Since u and d are relativistic particles, the correction for the chemical potential, to the lowest order in $\alpha_s = g^2/16\pi$ (g being the quark-gluon coupling constant), is given by

$$\mu_i = (1 + \frac{8}{3\pi}\alpha_s) p_F(i),\ i = u, d. \tag{4.11}$$

Hence, the Fermi momenta of u, d and e do not need to be collinear in order to activate β decay of d quarks. The calculation of emissivity is performed in Ref. [212] and gives

$$\epsilon_Q^{(d)} = \frac{914}{315}\alpha_s (G_F \cos\theta_c)^2 k_F^{(d)} k_F^{(u)} k_F^{(e)} T^6\,. \tag{4.12}$$

Due to the moderate mass of s quarks, the calculation of emissivity of the us branch does not rely on interactions. Finite mass takes the role of α_s and in this case the chemical potential can be written as

$$\mu_s = \sqrt{p_{F_s}^2 + m_s^2}, \tag{4.13}$$

which enables the β decay of s quarks to proceed. The resulting neutrino

Table 4.1: Various neutrino processes and the corresponding emission rates [21]. The q denotes any flavor of quarks and R are reduction factors induced by the pairing gaps. DU is the fast neutrino emission process, while the others are the neutrino processes with low emitting efficiency. The cooling of NSs is dominated by DU processes once they are active.

Name	Process	Emissivity (erg cm^{-3}s^{-1})
	I. Nuclear matter	
Direct Urca	$n \to p + e^- + \bar{\nu}_e$ $p + e^- \to n + \nu_e$	$\sim 10^{27} RT_9^6$
Modified Urca (n branch)	$n + n \to n + p + e^- + \bar{\nu}_e$ $n + p + e^- \to n + n + \nu_e$	$\sim 2 \times 10^{21} RT_9^8$
Modified Urca (p branch)	$p + n \to p + p + e^- + \bar{\nu}_e$ $p + p + e^- \to p + n + \nu_e$	$\sim 10^{21} RT_9^8$
Bremsstrahlung	$n + n \to n + n + \nu + \bar{\nu}$ $n + p \to n + p + \nu + \bar{\nu}$ $p + p \to p + p + \nu + \bar{\nu}$	$\sim 10^{19} RT_9^8$
Cooper pair formation	$n + n \to [nn] + \nu + \bar{\nu}$ $p + p \to [pp] + \nu + \bar{\nu}$	$\sim 5 \times 10^{21} RT_9^7$ $\sim 5 \times 10^{19} RT_9^7$
	II. Quark matter	
Direct Urca (ud branch)	$u + e^- \to d + \nu_e$ $d \to u + e^- + \bar{\nu}_e$	$\sim 10^{26} RT_9^6$
Direct Urca (us branch)	$u + e^- \to s + \nu_e$ $s \to u + e^- + \bar{\nu}_e$	$\sim 10^{25} RT_9^6$
Modified Urca (ud branch)	$q + u + e^- \to q + d + \nu_e$ $q + d \to q + u + e^- + \bar{\nu}_e$	$\sim 10^{21} RT_9^8$
Modified Urca (us branch)	$q + u + e^- \to q + s + \nu_e$ $q + s \to q + u + e^- + \bar{\nu}_e$	$\sim 10^{20} RT_9^8$

emissivity is also given in Ref. [212],

$$\epsilon_Q^{(s)} = \frac{457\pi}{840}(1-\cos\theta_{34})(G_F \sin\theta_c)^2 \mu_s k_F^{(u)} k_F^{(e)} T^6 , \tag{4.14}$$

where θ_{34} comes from the decay kinematics and $k_F^{(i)} (i = u, e)$ is the Fermi momentum of each particle. The absence of the strong coupling constant in Eq. (4.14) also indicates that the beta decay of the d quark is due to the strong interaction, whereas the one of the s quark is triggered by the finite quark mass [212]. This results in somewhat different neutrino emission rates. In general, the s quark DU process gives a smaller emissivity [2, 212], but above a certain density it could be the most prominent emission.

Comparing to the nucleonic DU process, which requires a threshold density [213], the quark DU process switches on immediately at the onset of quark matter since the electron fraction is high enough. In fact, if the density is large, the quark DU reactions could be completely switched off because of the too small electron fraction not fulfilling the Fermi momentum conservation [214].

In addition to the DU processes, there are also quark MU processes, which are much weaker than DU processes. Since the quark DU processes do not have a threshold density, the quark MU processes are negligible unless the quark pairing is taken into account. Note that quark DU processes are suppressed due to small fraction of electrons, while the quark MU remain active. However, this happens at extremely high density beyond the ones in NSs. The various neutrino reactions are summarized in Table 4.1.

4.3 Pairing

NS cooling is affected not only by the dense matter composition, but also by the neutron and proton superfluidity, as predicted by many microscopic theories [2]. These superfluids are produced by the pp and nn Cooper pairs formation due to the attractive part of the NN potential, and are characterized by a critical temperature T_c. The dominant channels of the neutron and proton superfluidity are the 1S0 and the coupled 3PF2 channels. The nn interaction in the 1S0 state is repulsive at supernuclear

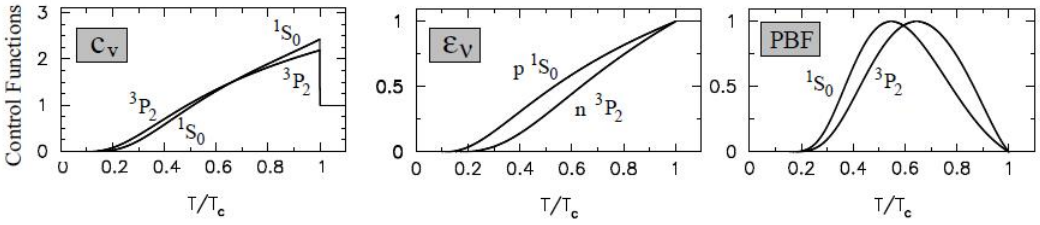

Figure 4.2: Examples of control functions for C_ν (left panel), Q_ν for MU processes (central panel) and the PBF process (right panel). From Ref.[21].

density, thus the neutron 1S0 gap (n1S0) only appears in the crust and neutron superfluidity at high density is caused by the 3P2 state which remains attractive. The interactions of protons in both 1S0 state and 3P2 state are attractive and can result in the proton superfluidity, however, the proton 3P2 gap remains uncertain at extreme density and is disregarded in our work.

The presence of superfluid gaps in the nucleon energy spectrum reduces the neutrino reaction rates and specific heat. The reduced results can be simply characterized by the unpaired results including control functions [21],

$$Q(T) \rightarrow Q_\nu^{\rm paired}(T) = R_\nu(T/T_c) \times Q_\nu^{\rm normal}, \tag{4.15}$$

$$C_\nu(T) \rightarrow C_\nu^{\rm paired}(T) = R_c(T/T_c) \times C_\nu^{\rm normal}, \tag{4.16}$$

where R_ν's for many processes can be found in Ref. [2], R_c is the control function for the specific heat being calculated in Ref. [18] for both 1S0 and 3P2 gaps. Some examples of control functions for neutrino emissivity are shown in Fig. 4.2. The neutrino emissivity is exponentially reduced, together with the specific heat. However, the pairing gaps of each component only affect the reactions involving it. For instance, the proton superfluidity does not affect the neutron-neutron bremsstrahlung, but strongly suppresses both Urca processes.

On the other hand, the baryon superfluidity initiates a specific neutrino emission due to Cooper pairing of nucleons, called the pair breaking and formation (PBF) processes. These processes take place only in

the presence of superfluidity, with the energy released in the form of a neutrino-antineutrino pair when a Cooper pair of baryons is formed. As an example, the PBF of neutron n3P2 has the emissivity

$$Q_\nu^{\rm n3P2} = 8.6\times10^{21}(\frac{n_b}{n_0})^{1/3}(\frac{m_n^*}{m_n})\times R_{\rm n3P2}(T/T_c)T_9^7 \tag{4.17}$$

where $R_{\rm n3P2}$ is the control function shown in right panel of Fig. 4.2. As we can see, when the temperature descends to T_c of a given type of baryons, the PBF process sets in and becomes maximally efficient when $T \approx 0.8\,T_c$, and then is exponentially suppressed for $T \ll T_c$ [2].

4.4 NSCOOL code

In this work, we use the widely used NSCOOL code [210] which is able to carry out the cooling simulations of NSs, hybrid stars and strange quark stars. The code adopts an implicit scheme (Henyey-type scheme) and solves the partial differential equations (Eqs. 4.1 and 4.2) on a grid of spherical shells. The inner boundary condition is taken at $r = 0$ with $L_r(r = 0) = 0$. Since the outer envelope, the so-called heat-blanketing envelope, contains a large temperature gradient and possible changes of the mass and composition due to accretion for instance, the outer boundary is cut at a radius $r = r_b$. In numerical simulation, the r_b is chosen that corresponds to the point where $L(r_b) \equiv L_\gamma$, and typical this point is taken as $\rho_b = 10^{10}$g cm^{-3} [21]. Hence the outer boundary condition becomes

$$L(r_b) = 4\pi R^2\sigma[T_e(T_b)]^4, \tag{4.18}$$

where T_b is the temperature at $r = r_b$, and the relation between T_e and T_b is determined by the envelope models.

Each simulation starts with a constant initial temperature profile,$\tilde{T} = Te^{\Phi} = 10^{10}K$, and no heat transport, $L_r = 0$. It was found that the cooling curves are not sensitive to the initial temperature profile. We notice that beneath the heat-blanketing envelope the star's structure, including mass, radius and composition, is assumed to be unchanged throughout the entire cooling simulation.

Regarding the most important ingredient - neutrino emissivity, this code comprises all relevant cooling reactions as introduced in Sec. 4.2: nucleonic DU, MU, PBF and BS in the nuclear matter; and quark DU and MU in the quark matter. The modifications of neutrino emissivity due to the pairing gaps are also included. In order to reflect the uncertainty of the gap, the scaling factors of each gap are introduced in this code.

Moreover, various processes in the crust are included, such as the most important electron-nucleus bremsstrahlung, plasmon decay, electron-ion bremsstrahlung, etc. A detailed introduction of these processes can be found in Ref. [2].

Chapter 5

Thermal evolution of neutron stars

In this chapter, we study NS cooling with several microscopic nuclear EOS based on different nucleon-nucleon interactions and three-body forces, and compatible with the recent GW170817 NS merger event as tested in Chapter 3. They all feature strong DU processes. We find that all models are able to describe well the current set of cooling data for isolated NSs, provided that large and extended proton 1S0 (p1S0) gaps and no neutron 3P2 gaps are active in the stellar matter. We then analyze the NS mass distributions predicted by the different models and single out the preferred ones.

Furthermore, we model and quantize in the same way the cooling of hybrid NSs combining a microscopic nuclear EOS in the BHF approach with different quark models. We find that also in this scenario the possibility of neutron p-wave pairing can be excluded.

This chapter is a modified version of the following articles:

[1] J.-B. Wei, G. F. Burgio and H.-J. Schulze, *Neutron star cooling with microscopic equations of state*, MNRAS 484, 5162 (2019).

[2] J.-B. Wei, G. F. Burgio, H.-J. Schulze and D. Zappalà, *Cooling of hybrid neutron stars with microscopic equations of state*, MNRAS 498, 344 (2020).

5.1 Cooling of nucleonic stars

5.1.1 Structure and composition

During the cooling simulation, some quantities such as mass, radius and internal profile of the NS remain unchanged. Thus we are able to determine when the DU process is active from the known EOS and NS structure.

For the different EOSs used in this work, the DU process sets in at slightly different values of the proton fraction x_p due to the presence of muons, as shown in Fig. 5.1. The threshold values $x_{\rm DU}$ are calculated starting from Eq. (4.5), in which the momentum conservation imposes the triangle rule, i.e.,

$$k_F^{(n)} < k_F^{(p)} + k_F^{(e)} \,. \tag{5.1}$$

This is indicated by the vertical dotted lines in Fig. 5.1 for the different EOSs, and $x_{\rm DU}$ is comprised in the range $0.133 < x_{\rm DU} < 0.136$. It is important to determine at which corresponding value $\rho_{\rm DU}$ of the nucleon density of beta-stable and charge-neutral matter the DU process sets in, because compact stars characterized by central densities larger than $\rho_{\rm DU}$ will cool down very rapidly. This is also displayed in Fig. 5.1 and occurs in a density range between 0.30 and 0.45 fm^{-3} depending on the EOS. In the lower panel we display the NS mass-central density relations obtained by solving the TOV equations for hydrostatic equilibrium. The NS masses $M_{\rm DU}$ corresponding to the central densities $\rho_{\rm DU}$ span a range between 0.82 $M_\odot$ (N93) and 1.56 $M_\odot$ (BOB), above which the DU process can potentially operate. As discussed in Chapter 3, in all cases (marginally for the UIX) the value of the maximum mass $M_{\rm max}$ is larger than the current observational lower limits [73, 158, 216].

The main results for $x_{\rm DU}$, $\rho_{\rm DU}$, $M_{\rm DU}$, and $M_{\rm max}$ are also listed in Table 5.1. We conclude that in all cases there is a wide range of NS masses where the DU process is operative, practically for all NSs with the V18 and N93 EOSs, while only for the BOB EOS the threshold $M_{\rm DU} = 1.56\ M_\odot$ is high, but in this case also $M_{\rm max} = 2.51\ M_\odot$ is very large.

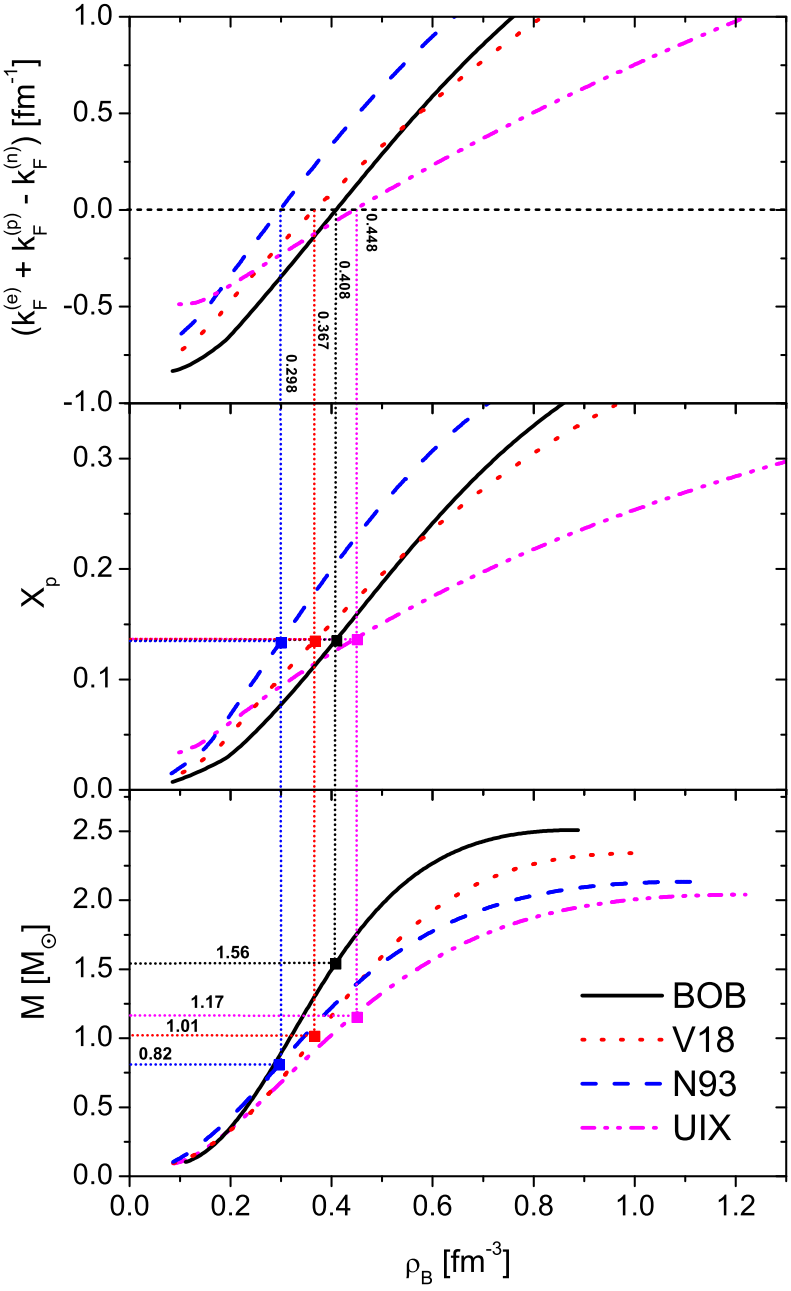

Figure 5.1: DU onset condition (upper panel), proton fraction (central panel), and NS mass (lower panel) vs. the (central) baryon density for the different EOSs. The vertical dotted lines indicate the threshold density for the DU process. From Ref. [215].

Table 5.1: Characteristic properties of several EOSs: DU onset proton fraction $x_{\rm DU}$, density $\rho_{\rm DU}$, and corresponding NS mass with that central density $M_{\rm DU}$. Upper limit of the range of p1S0 pairing ρ_{1S0} and NS mass with that central density M_{1S0}. Maximum NS mass $M_{\rm max}$. Densities are given in fm^{-3} and masses in $M_\odot$. From Ref. [215].

EOS	$x_{\rm DU}$	$\rho_{\rm DU}$	$M_{\rm DU}$	ρ_{1S0}	M_{1S0}	$M_{\rm max}$
BOB	0.1357	0.41	1.56	0.59	2.23	2.51
V18	0.1348	0.37	1.01	0.60	1.92	2.34
N93	0.1331	0.30	0.82	0.52	1.59	2.13
UIX	0.1363	0.45	1.17	0.70	1.70	2.04

5.1.2 Cooling diagrams of non-superfluid stars

For a better understanding, we begin by discussing the simulations obtained with different EOSs without including any superfluidity. Results are displayed in Fig. 5.2, where the luminosity vs. age is plotted for several NS masses in the range $1.0, 1.1, ..., M_{\rm max}$ (solid black curves). The dashed green curves mark the NS mass $M_{\rm DU} + 0.01\,M_\odot$ at which the DU process has just set in, whereas the dotted green curves correspond to the maximum mass $M_{\rm max}$.

Our set of observational cooling data comprises the (age, temperature/luminosity) information of the 19 isolated NS sources listed in [51], where it was also pointed out that in many cases the distance to the object, the composition of its atmosphere, thus its luminosity, and its age are rather estimated than measured. Thus in these cases, we use large ad-hoc error bars (a factor 0.5 and 2) to reflect this uncertainty.

The results are clearly unrealistic, as observed NSs would essentially be divided into very hot ones and very cold ones by the DU threshold $M_{\rm DU}$, with very few stars in between: In a NS with $M < M_{\rm DU}$, the DU process is turned off and therefore the total neutrino emissivity is orders of magnitude smaller than for a NS with a mass above the DU threshold. Consequently the former has at a given age ($t \gtrsim 300\,$yr) a much higher luminosity than the latter. All NSs with $M < M_{\rm DU}$ have a small neutrino

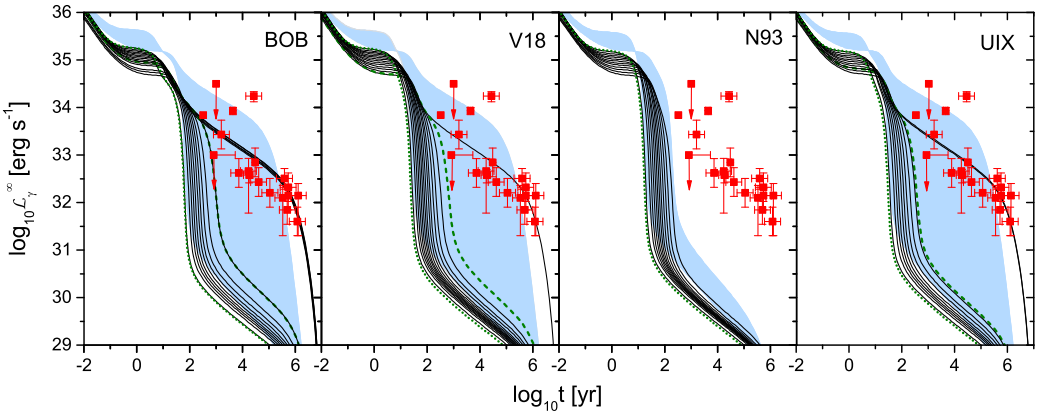

Figure 5.2: Cooling curves for different EOSs without any pairing for different NS masses $M/M_\odot = 1.0, 1.1, \ldots, M_{\rm max}$ (decreasing curves). The dashed green curves mark the NS mass $M_{\rm DU} + 0.01\ M_\odot$ at which the DU process has just set in, and the dotted green curves correspond to $M_{\rm max}$ for each EOS. The black curves are obtained with a Fe atmosphere and the shaded areas cover the same results obtained with a light-elements ($\eta = 10^{-7}$) atmosphere. The data points are from [51]. See text for more details. From Ref. [215].

emissivity, hence their cooling curves are nearly indistinguishable on the scale of Fig. 5.2, while for objects with $M > M_{\rm DU}$, the larger is the mass and thus the bigger is the central region of the star where the DU process operates, the lower is the luminosity and the cooling curves are no longer superimposed.

This feature depends on the EOS as explained in Sect. 5.1.1. For example, in the N93 case the DU onset takes place at a very small value of the density and the related gravitational mass $M_{\rm DU} = 0.82\ M_\odot$, and therefore all NS masses undergo DU processes. In the V18 case, the DU process starts for a $1.01\ M_\odot$ NS, and therefore only the first upper curve is influenced by MU alone, whereas the remaining ones are determined by DU cooling. The other EOSs have higher threshold values of $M_{\rm DU}/M_\odot = 1.17, 1.56$ for the UIX and BOB, respectively.

5.1.3 Cooling diagrams of superfluid stars

We now discuss the effect of pairing gaps on the cooling evolution. The pairing gaps we employed are computed with the V18 NN interaction, and using TBF and effective masses derived from the corresponding EOS, thus performing a completely consistent description [17]. We remind that the pairing gaps were computed on the BCS level by solving the (angle-averaged) gap equation in the $T = 1$ and $S = 0$, $L = 0$ (1S0) or $S = 1$, $L = 1, 3$ (3PF2) channels [217, 218, 219, 220, 221, 222]. The relation between (angle-averaged) pairing gap at zero temperature $\Delta \equiv \sqrt{\Delta_L^2(k_F) + \Delta_{L'}^2(k_F)}$ obtained in this way and the critical temperature of superfluidity is then $T_c \approx 0.567\Delta$. For further details concerning the formalism, one can refer to the above quoted references.

For a better understanding, we display in Fig. 5.3 the BCS pairing gaps and critical temperatures as a function of baryonic density of beta-stable matter for the different EOSs. In this way one can easily identify which range of gaps is active in different stars, whose central densities are shown by vertical dotted lines for given NS masses. A n1S0 gap exists only in the crust, while the n3P2 gap with lower strength covers almost the entire density range of NSs for all EOSs. However, the n3P2 gap could be completely suppressed due to polarization correction [223]. Regarding the p1S0 pairing, an important information is the density ρ_{1S0} at which the BCS gap disappears, and the corresponding NS mass M_{1S0} with that central density. The DU process can only be completely blocked for NSs with $M < M_{1S0}$, whereas for heavier stars it is active and unblocked in a certain domain of the core, which leads to extremely fast cooling of these objects. The value of M_{1S0} is also listed in Table 5.1 and together with $M_{\rm DU}$ determines the ranges of blocked and unblocked DU cooling. We observe that for the BOB, V18, UIX, N93 EOS the DU blocking terminates at $M/M_\odot = 2.23, 1.92, 1.70, 1.59$, respectively, which implies very rapid cooling for heavier stars, reflected in the following cooling diagrams. The regions of blocked DU cooling are represented by shading in Fig. 5.3.

We now discuss the cooling curves when the n1S0 and p1S0 gaps are switched on, as shown in Fig. 5.4 (upper panels). For the gaps used in this work, the main effect of superfluidity on NSs with $M > M_{\rm DU}$ (dashed green curves, partially covered) is the strong quenching of the

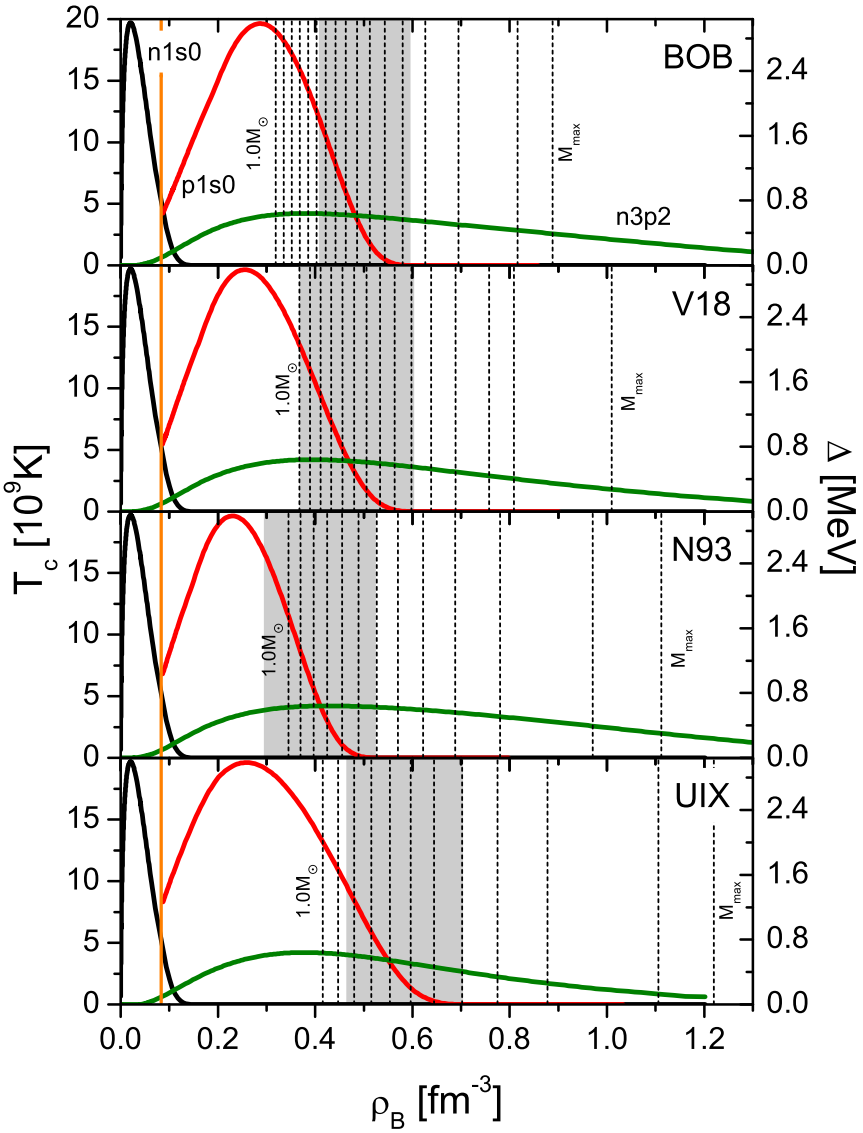

Figure 5.3: BCS gaps in the n1S0, p1S0, and n3P2 channels in NS matter for the different EOSs. The vertical dotted lines indicate the central density of NSs with different masses $M/M_\odot = 1.0, 1.1, \ldots$, up to the maximum mass value. The shaded areas indicate the region between DU onset density $\rho_{\rm DU}$ and vanishing of the p1S0 gap at ρ_{1S0} (listed in Table 5.1), i.e., where the DU process is blocked by pairing. The orange vertical line represents the crust-core boundary. From Ref. [215].

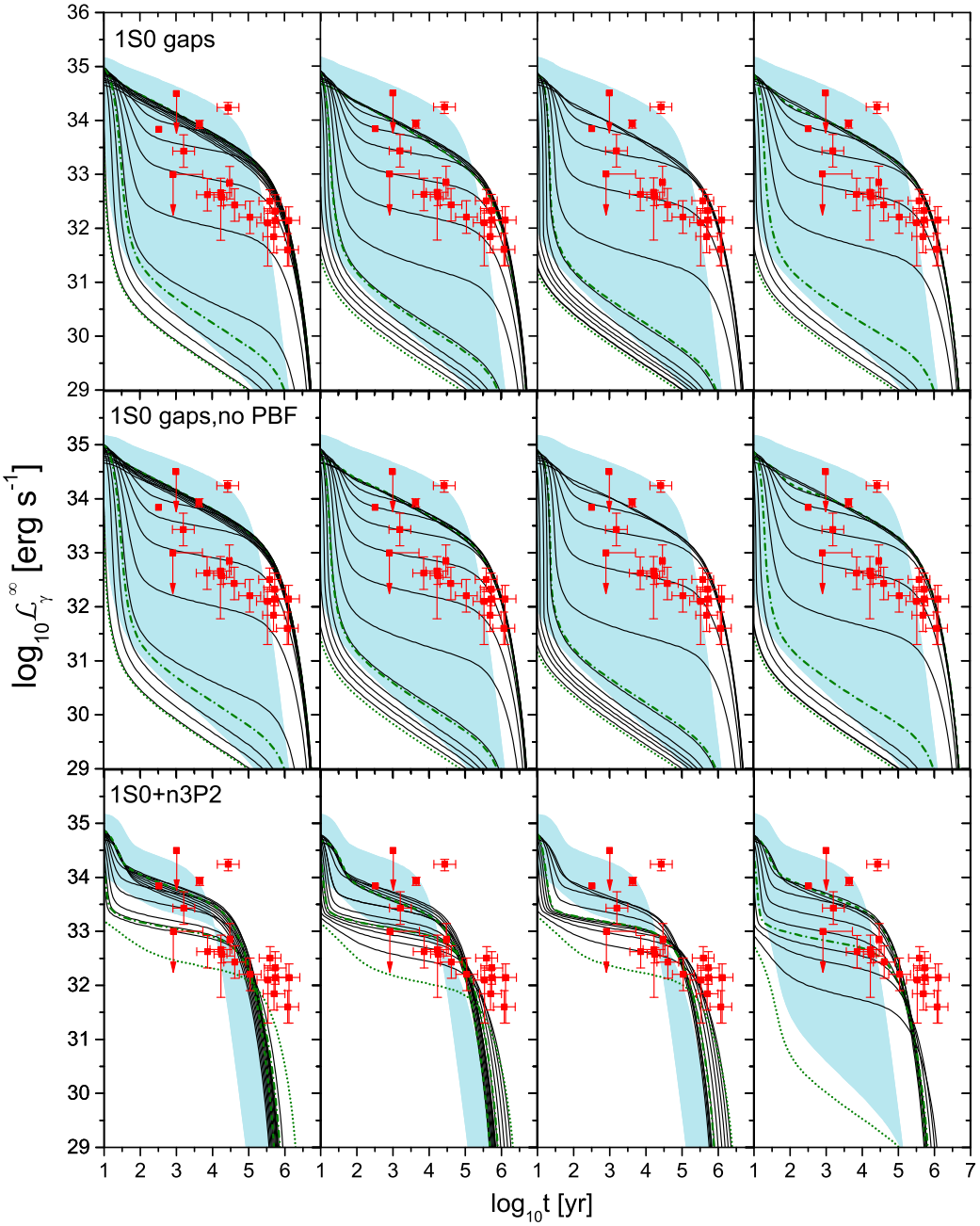

Figure 5.4: Same as Fig. 5.2 but with the inclusion of n1S0 and p1S0 BCS gaps (upper panels), and excluding the PBF processes in the latter case (central panels) for different NS masses. Lower panels show the case including all three BCS gaps (n1S0, p1S0, n3P2). The dashed green curves mark the NS mass $M_{\rm DU} + 0.01\ M_\odot$ at which the DU process has just set in, and the dash-dotted green curves mark the NS mass M_{1S0} for which the p1S0 gap vanishes in the center of the star. From Ref. [215].

DU process, and thus a substantial reduction of the total neutrino emissivity. Hence those stars have a higher luminosity compared to the non-superfluid case. On the other hand, if $M > M_{1S0}$ (dash-dotted green curves), the complete blocking of the DU process disappears and the star cools very rapidly again. One observes results in line with these features in the figure, namely between $M_{\rm DU}$ and M_{1S0} there is now a smooth dependence of the luminosity on the NS mass for a given age. The effect is qualitatively the same for all EOSs, just the distribution of NS masses in the cooling diagram depends on the EOS, which will be analyzed in the next section.

Regarding the effect of the atmosphere models, we note that by assuming a proper atmosphere for any given data point, all current cooling data could potentially be explained in the present scenario, by assigning a Fe atmosphere (black curves) to the oldest objects and an accreted light-elements atmosphere (shaded area) to the hottest ones. The currently known most extreme (very hot) object, XMMU J1731-347, ($\log_{10} t \approx 4.4$, $\log_{10} L_\gamma^\infty \approx 34.2$), is indeed supposed to have a carbon atmosphere, see the discussions in [51, 56, 57, 58].

Although in general the presence of superfluidity is slowing down the cooling, the PBF processes might prevail in certain situations and provide an accelerated cooling of some stellar configurations [61, 224, 225, 226]. It is therefore of interest to show in Fig. 5.4 (middle panels) also results where the 1S0 PBF processes have been switched off by hand. It can be seen, however, that the effect of PBF cooling in the 1S0 channels is practically negligible.

For completeness, we present the cooling curves in Fig. 5.4 (lower panel), taking into account both 1S0 gap and n3P2 gap. It is clear that the results including the n3P2 gap are incompatible with observations. This is consistent with Refs. [51, 56, 57, 62, 63, 227, 228]. In Ref. [227], for instance, the author employed the "nuclear medium cooling" scenario with both gaps [62, 63, 228]. As shown in their paper, the inclusion of the n3P2 gap results in too efficient PBF processes and a too fast cooling, which makes the "nuclear medium cooling" scenario fail to explain at least several of the cooling data. One requires thus a strong suppression of the n3P2 gap. We remind that in the "nuclear medium cooling" the in-medium effects (in particular on the pion propagator) might strongly enhance the

emissivities of modified Urca processes by a factor of $10^2 - 10^3$, and also the PBF processes [229, 230, 231]. This conclusion regarding the n3P2 gap remains valid even without the in-medium effect [51, 56, 57, 58, 61].

In our results, as seen in the lower panel of Fig. 5.4, the cooling curves of NSs distribute in a narrow area and are not able to match all the data points. This is due to that the very effective n3P2 PBF process is enabled, which leads to too fast cooling for the stars with medium mass. In addition, the n3P2 gap extends to large density and suppresses the DU processes even for the most massive NSs, which exhibit a fast cooling evolution with only 1S0 gaps considered.

We conclude that a successful consistent modeling of all cooling data (in particular XMMU J1731-347) requires an extended p1S0 gap and a very small or vanishing n3P2 gap, which is consistent with the results of Refs. [51, 56, 57, 62, 63, 227, 228]. Furthermore, the BCS p1S0 gap alone is able to suppress sufficiently the DU cooling and to yield realistic cooling curves, provided that it extends over a large enough density/mass range. This is the case for all our considered EOSs, which yield however different mass profiles in the luminosity vs. age plane. This illustrates the necessity of precise information on the masses of the NSs in the cooling diagram, without which no theoretical cooling model can be verified. We study this issue in some detail in the following.

5.1.4 Neutron star mass distributions

The extraction of the NS mass distribution from the cooling curves in the $T - t$ diagram was first proposed in Refs. [234, 235], by counting the number of cooling data from the binning in the mass intervals, which could be used to compare with the theoretical mass distribution in the Universe, from population synthesis for example [236, 237]. As suggested in [234, 235], the deduced mass distributions are very sensitive to the chosen cooling models (for instance with different gaps) and of course the EOSs including the hadronic and hybrid stars. Hence, the deduced mass distribution could be another constraint on cooling simulations.

Here, we follow this idea and discuss the constraint of the deduced NS mass distribution on the considered microscopic EOSs, assuming that the currently observed set of isolated NSs in the cooling diagrams of

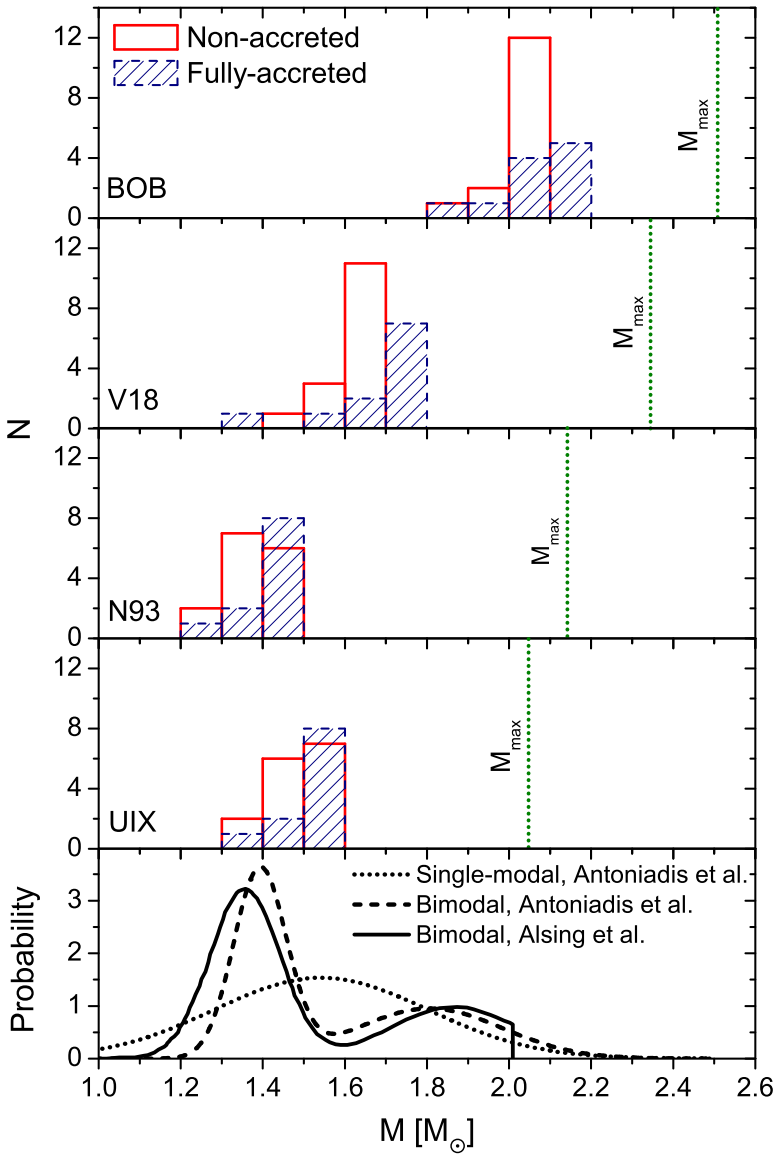

Figure 5.5: Deduced NS mass distributions from the cooling diagrams in Fig. 5.4 (upper panels) for the different EOSs. Maximum masses are also indicated. The lowest panel shows some recent theoretical results [232, 233]. From Ref. [215].

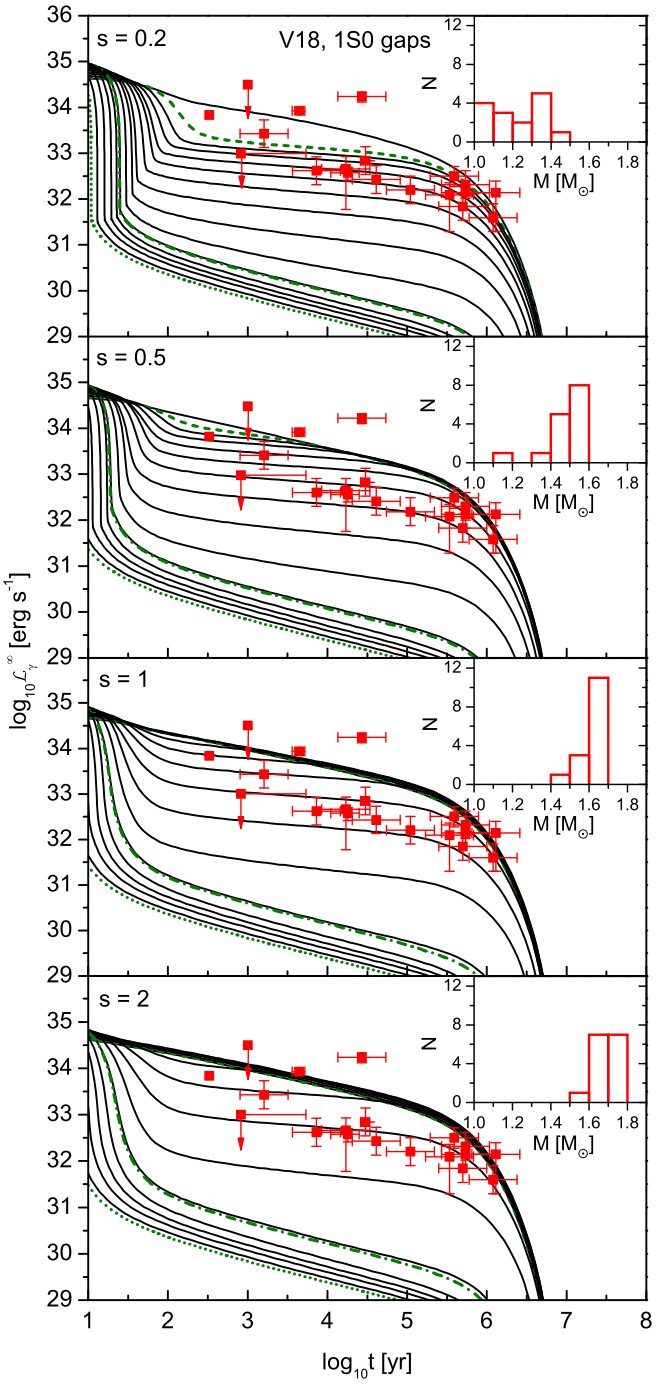

Figure 5.6: Cooling curves obtained with the V18 EOS, Fe atmosphere, and 1S0 BCS gaps scaled by factors $s = 0.2, 0.5, 1.0, 2.0$. The insets show the derived mass distributions. From Ref. [215].

Fig. 5.4 reflects the unbiased mass distribution of NSs in the Universe (which is highly unlikely due to strong selection effects; for example, very old and massive NSs are too faint to be observed and would therefore never appear in the cooling diagrams. Also, the mass distribution of isolated NSs could be very different from those in binary systems, etc.) For simplicity we disregard the error bars in this analysis. The results are shown as histograms in Fig. 5.5, obtained directly from the binning in mass intervals in Fig. 5.4. One observes clear differences between the four EOSs, with surprisingly small dependence on the atmosphere model. The lowest panel provides for comparison a compilation of recent theoretical results for the NS mass distribution [232, 233, 238, 239]. We stress again, however, that there is no good reason that the mass distribution extracted from the cooling data in this way should be similar to the overall mass distribution of NSs in the Universe or even to that of isolated NSs only.

Due to this problem and the scarcity of data, no firm conclusions can be drawn for the moment, apart from perhaps excluding the BOB model, which does not predict any data point even close to the NS canonical value of about 1.4 $M_\odot$. This model features also a very large $M_{\rm max}$ = 2.51 $M_\odot$, which seems to be in conflict with recent upper limits on $M_{\rm max}$ derived from analysis of the NS merger event [159, 160, 82]. On the other hand, the $M_{\rm max}$ = 2.04 $M_\odot$ of the UIX EOS appears too small, which leaves as most realistic models either N93 or V18. Clearly more data points, ideally with assigned known masses, would be required for a more profound analysis of this kind.

To emphasize even more the value of data with well-assigned masses, we point out that the mass distributions do not only depend on the EOS, but also on the pairing gaps. For that purpose we plot in Fig. 5.6 the results obtained with the V18 model and applying different scaling factors $s = 0.2, 0.5, 1.0, 2.0$ to the 1S0 BCS gaps, which could be motivated by the polarization effects. One sees that while the overall coverage of the luminosity vs. age plane remains nearly unaffected, the deduced NS mass distributions (shown as insets) depend sensitively on the gap scaling factor. In the specific case, one would be able to exclude very large scaling factors, which is indeed physically reasonable. Of course, modifying also the density domain of the pairing, similar variations would be obtained in line with the considerations in Sec. 5.1.3 [240]. But we think

it is premature to try to resolve this issue with the present set of cooling data.

5.2 Cooling of hybrid stars

5.2.1 Structure and composition

We now extend our study to hybrid stars, combining the hadronic V18 EOS and various quark EOSs as introduced in Chapter 2. The parameters of all quark models have been adjusted in such a way as to decrease the maximum mass from the value $M_{\rm max} = 2.34\,M_\odot$ of the purely hadronic V18 EOS down to the same value $M_{\rm max} = 2.10\,M_\odot$ in all hybrid star cases, so as to be compatible with the current constraint [74]. For this purpose, we choose the values $B_{\rm DS} = 138$ MeV fm^{-3} and 42 MeV fm^{-3} for $\alpha = 1.5$ and $\alpha = 1.0$, respectively, in the DSM. This condition imposes a smaller $B_{\rm DS}$ for $\alpha = 1.0$. The effect of smaller $B_{\rm DS}$ makes the EOS of quark matter stiffer, but at the same time it lowers the hadron-quark phase transition point and makes the total EOS of the hybrid star softer. This results in a reduction of the maximum mass. As reminded in Chapter 2, $B_{\rm DS}$ cannot be arbitrarily low. Here, the DS1.0 model is an extreme choice close to the lower limit in order to enforce a quark matter onset density $\rho_{\rm QM}$ as low as possible. Regarding the FCM, we have used $V_1 = 142$ MeV and $G_2 = 0.006$ GeV^4, so as to fix the hybrid star maximum mass to 2.1 $M_\odot$, as for the DSM.

The selected EOSs and the resulting NS structures are shown in Fig. 5.7 and Fig. 5.8, respectively. For the comparison, we include results of a hybrid star using the MIT bag model for quark matter. As shown, the appearance of quark matter leads to a strong softening of the EOS, and induces a decrease of the NS maximum mass. Also, the limit on the maximum mass requires fairly large quark-matter threshold densities $\rho_{\rm QM}$ and associated masses $M_{\rm QM}$, see Table 5.2. The biggest quark-matter content is achieved by the DS1.0 model with $\rho_{\rm QM} \approx 0.5$ fm^{-3} and $M_{\rm QM} \approx 1.6\,M_\odot$. Lowering further the values of $\rho_{\rm QM}$ leads to too low maximum masses of the hybrid models. In the same table we also list the density ρ_{1S0} at which the p1S0 gap vanishes and the corresponding gravitational mass, which

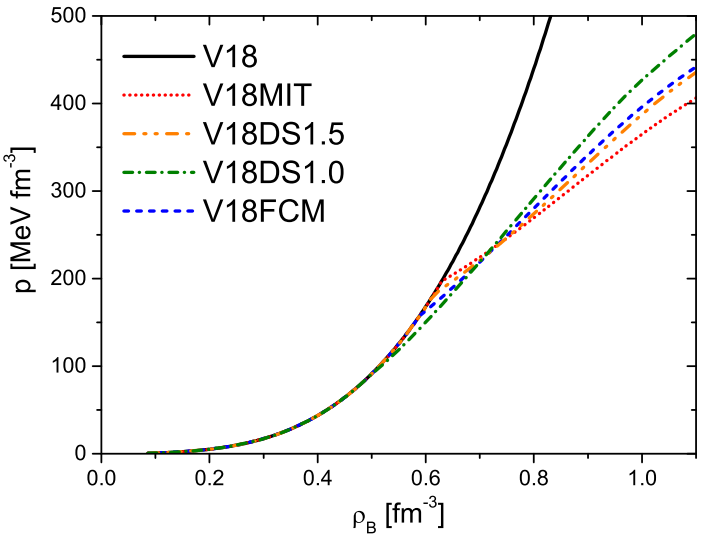

Figure 5.7: The EOS for the different models. The solid black curve represents the purely hadronic case, whereas the broken colored curves are the hybrid EOSs. From Ref. [241].

will be important for the forthcoming discussion. For completeness, the values of the central densities of the maximum-mass configuration are also reported.

In Fig. 5.9 we compare the particle fractions of all models. In the upper panel results are displayed for the purely nucleonic case, whereas in the other panels the populations of the hybrid models are plotted. The vertical dashed lines represent the values of the baryon density at which the nucleonic DU process starts and the corresponding mass $M_{\rm DU}$, the values of the quark-matter onset density for the mixed phase and its mass $M_{\rm QM}$, and finally the central density of the maximum-mass configuration $M_{\rm max}$. We notice that in all cases the onset of the DU process takes place at a smaller density than the one of the mixed phase, which depends on the adopted model for the quark phase. In all cases, the maximum-mass configurations contain still more than 50% of nucleonic matter in their center, while pure quark matter is only reached at extreme densities, not present in hybrid stars. The DS1.0 model features the biggest quark matter content, and in this case the p1S0 gap extends into the mixed

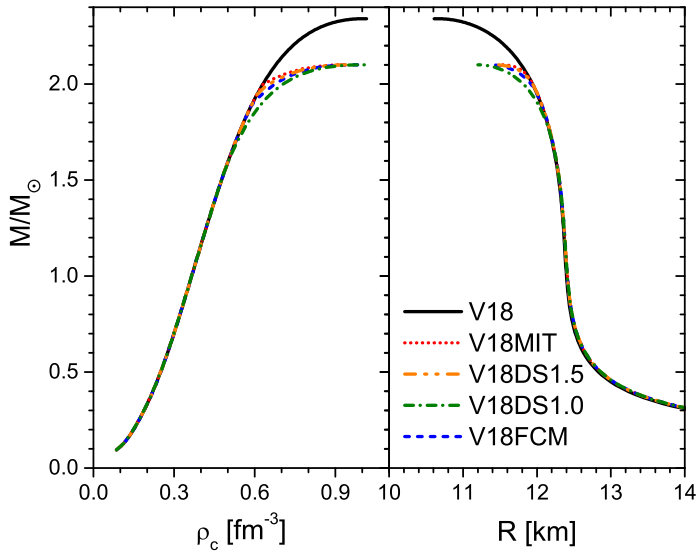

Figure 5.8: Gravitational mass vs. central density (left panel) and radius (right panel) for the different models. The maximum mass for all hybrid EOSs is, by construction, $M_{\rm max} = 2.1\,M_\odot$. From Ref. [215].

phase. A similar behavior is slightly present also in the FCM, whereas in the MIT and DS1.5 models the p1S0 gap is active only in the pure nucleonic phase.

5.2.2 Cooling reactions in a hybrid star

In addition to the cooling reactions in nuclear matter, hybrid stars also feature quark DU (QDU) and quark MU (QMU) processes. The role played by the different processes is illustrated in detail in Fig. 5.10 for a V18+FCM hybrid star with (maximum) mass $M = 2.1\,M_\odot$. The upper panel displays the nucleonic, leptonic and quark populations (curves) together with the p1S0 and n3P2 critical temperatures (shaded areas) vs. the radial distance, whereas the lower panels show the various neutrino emissivities at a temperature $T = 10^8$ K (corresponding roughly to an age of 10y or 0.1y with/out n3P2 pairing) for the different cooling channels. The central panel employs only 1S0 pairing, whereas the lower panel includes

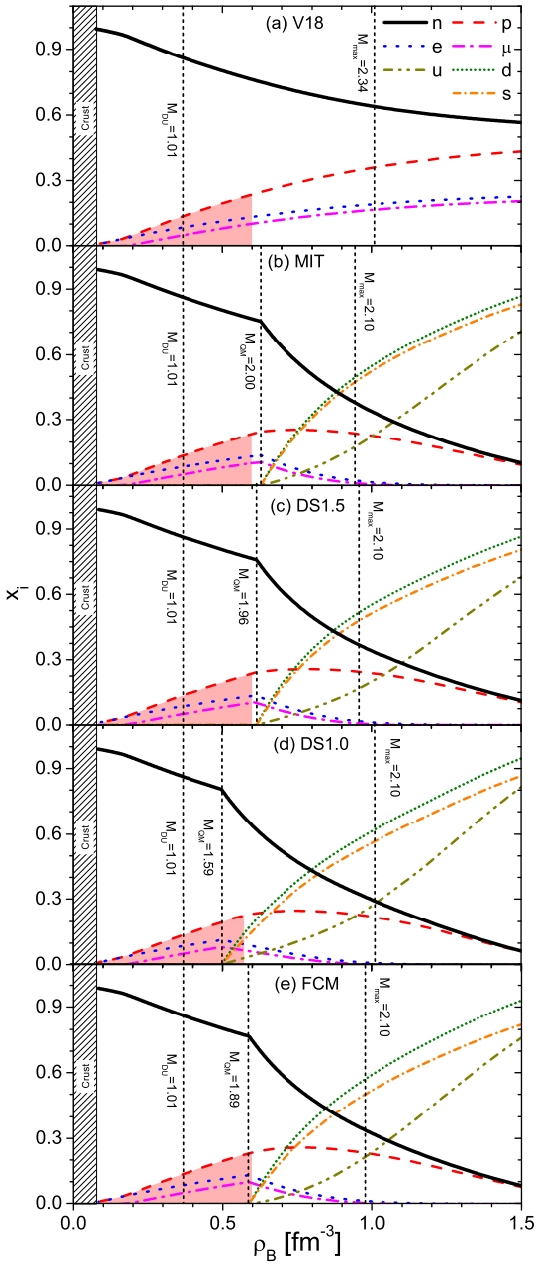

Figure 5.9: Composition of beta-stable stellar matter with the Gibbs construction for different quark models. Vertical lines indicate the onset of nucleonic DU cooling, the onset of the quark-matter mixed phase, and the maximum central density. Corresponding mass values of NSs with those central densities are given. The shaded areas indicate the range over which the p1S0 gap is active. From Ref. [215].

Table 5.2: Characteristic properties of several EOSs: densities ρ (in fm^{-3}) and corresponding NS masses M (in $M_\odot$) with that central density characterising the nucleonic DU cooling onset, quark-matter onset, the vanishing of the p1S0 gap, and maximum-mass configuration. From Ref. [241].

EOS	$\rho_{\rm DU}$	$M_{\rm DU}$	$\rho_{\rm QM}$	$M_{\rm QM}$	ρ_{1S0}	M_{1S0}	$\rho_{\rm max}$	$M_{\rm max}$
V18	0.37	1.01	-	-	0.599	1.92	1.010	2.34
MIT	0.37	1.01	0.629	2.00	0.599	1.92	0.944	2.10
DS1.5	0.37	1.01	0.614	1.96	0.599	1.92	0.960	2.10
DS1.0	0.37	1.01	0.498	1.59	0.576	1.80	1.009	2.10
FCM	0.37	1.01	0.588	1.89	0.599	1.91	0.977	2.10

also the n3P2 gap.

We observe that in the mixed phase in the core (containing up to about 50% quark matter), the main contribution to the cooling comes from the QMU, and in the case without n3P2 gap (central panel) also from the nucleonic DU (NDU) reaction. All other reactions are weaker by several orders of magnitude.

At about $r \approx 6$ km quark matter vanishes and the cooling is regulated by the nucleonic processes only: the dominant NDU is active up to $r \approx 9$ km, where the proton fraction becomes too small. For this model, the p1S0 gap happens to vanish close to the onset of the mixed phase, and therefore NDU cooling is undamped inside the mixed phase (central panel) *unless* the n3P2 gap is present (lower panel). The nucleonic MU (NMU) and QMU reactions play only minor roles, together with nucleonic BS (NBS), which is the only relevant cooling process in the outer part of the star when only p1S0 pairing is active (central panel).

The PBF processes merit a separate discussion: Due to their nature, they only provide significant and even dominant contributions when the local critical temperature (either p1S0 or n3P2) is slightly above the value of the actual temperature. Under the conditions chosen for Fig. 5.10 (see the values of T_c in the upper panel), this occurs around $r \approx 6-7$ km for the p1S0 channel, and $r \approx 10-11$ km for the n3P2 gap when present. In the latter case, due to the concurrent suppression of the NDU process, the PBF reactions become the most efficient nucleonic cooling process, which

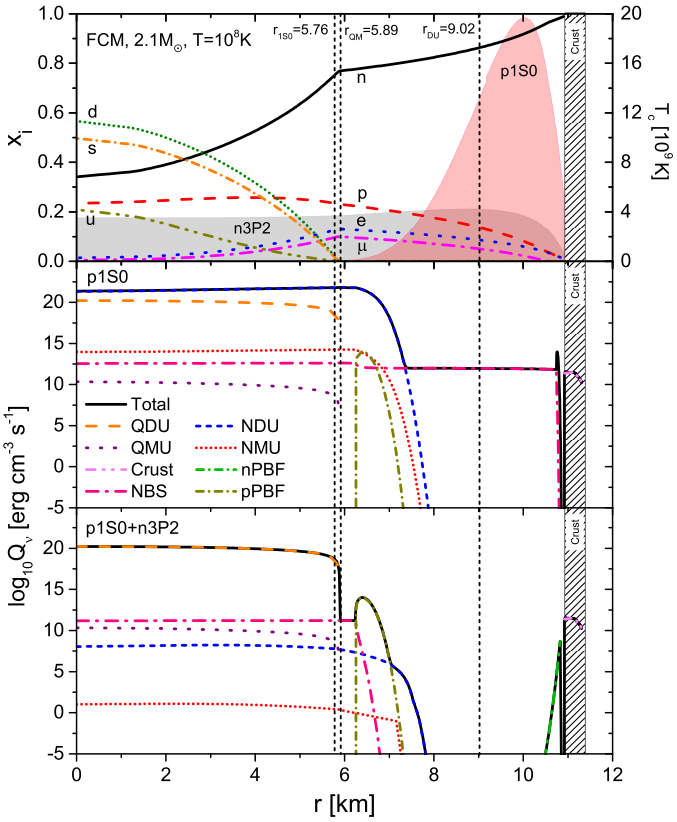

Figure 5.10: Composition and pairing gaps (upper panel) and neutrino emissivities at $T = 10^8$K (lower panels) as a function of the radial distance r for a hybrid star with mass $M = 2.1\,M_\odot$ and the FCM EOS. From Ref. [241].

has important consequences for the final luminosity vs. age plots.

We stress that emissivity plots like Fig. 5.10 depend decisively on the matter composition, i.e., the NS mass, and the value of the temperature, related to the NS age. The values $M = 2.1\,M_\odot$ and $T = 10^8$ K chosen for Fig. 5.10 provide only one particular snapshot of the cooling history. In particular the zones and magnitudes of PBF cooling inside the star depend extremely sensitively on the local temperatures, and the complete cooling history has to be integrated in order to make quantitative statements, which we investigate now.

5.2.3 Cooling diagrams with unpaired quark matter

Fig. 5.11 shows the resulting final cooling diagrams for the different models, namely the luminosity vs. age is plotted for several NS masses in the range $1.0, 1.1, ..., 2.1\, M_\odot$ (solid black curves). Eventual dashed black curves represent $M = 1.95, 2.05\, M_\odot$ for a better resolution. The dash-dotted green curves mark the NS mass $M_{\rm QM} + 0.02\, M_\odot$ at which the QDU process has just set in. Results employing only 1S0 pairing (left column) and with n3P2 pairing included (right column) are compared for the different models.

One observes the following general features: Since $M_{\rm DU} = 1.01\, M_\odot$, practically all cooling curves involve nucleonic DU cooling, which is however quenched by the p1S0 pairing active up to $M_{\rm 1S0} \approx 1.9\, M_\odot$ ($\approx 1.8\, M_\odot$ for the DS1.0 model), nearly coincident with the onset of the quark phase and the related rapid quark DU cooling. Since the quark-matter onset density is fairly large for all quark models, only high-mass NSs, $M \gtrsim 1.9\, M_\odot$ ($\gtrsim 1.6\, M_\odot$ for the DS1.0), exhibit different cooling behavior for the hybrid models. No observational data exist currently for such heavy and faint objects (lying below the dash-dotted green curves in Fig. 5.11). On the other hand, as only heavy NSs are affected by the presence of quark matter, very reasonable NS mass distributions can be deduced when confronting the theoretical curves with the available cooling data in the figure, see the results in Fig. 5.5, where the mass histograms were simply computed by counting the number of data points (error bars disregarded) lying between the two adjacent theoretical cooling curves in the luminosity vs age plot.

One common conclusion with [242, 243] can be made here, namely that quark matter has significant effects only if NDU cooling is suppressed. Therefore within the DS1.0 model, the hybrid star shows faster cooling for masses between 1.6 and $1.8\, M_\odot$, whereas for masses larger than $1.8\, M_\odot$, NDU cooling in the inner core is not quenched by the p1S0 pairing anymore, and the effect of quarks tends to be invisible. This is also the case of the other three models, since $M_{\rm QM} \approx M_{\rm 1S0}$. Compared to the results with p1S0 pairing only, all quark models could have significant effects when including n3P2 pairing that covers a large density range.

This is shown in the right column of Fig. 5.11, where we display the

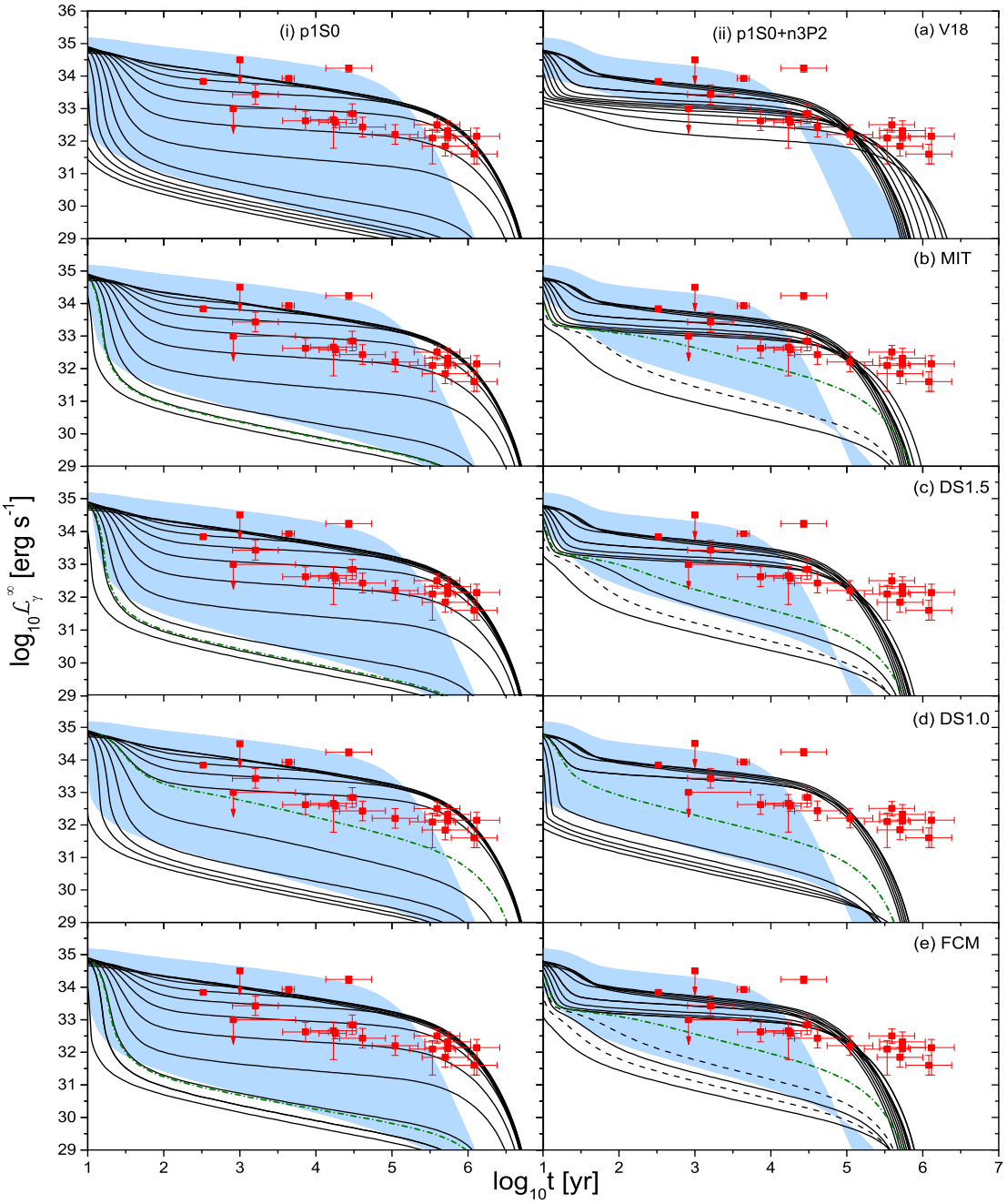

Figure 5.11: Cooling curves with/out n3P2 pairing, for different NS masses $M/M_\odot = 1.0, 1.1, \ldots, 2.1$ (decreasing solid black curves). Eventual black dashed curves indicate the $M/M_\odot = 1.95, 2.05$ results. The dash-dotted green curves mark the NS mass $M_{\rm QM} + 0.02\,M_\odot$ at which the quark DU process has just set in. The black curves are obtained with a Fe atmosphere and the shaded areas cover the same results obtained with a light-elements ($\eta = 10^{-7}$) atmosphere. From Ref. [241].

cooling curves for the case with the n3P2 gap included. As already discussed in Sec. 5.1.3, an important conclusion can be drawn regarding the nucleonic pairing: While very satisfactory results can be obtained employing only 1S0 pairing, the addition of n3P2 superfluidity leads to too fast cooling for all models considered, such that old and warm NSs cannot be reproduced by any model. Thus, as for the purely nucleonic EOSs before, we can exclude the possibility of n3P2 pairing in our approach, even allowing the existence of a phase transition to quark matter. This is because only very massive stars are affected by the latter feature. As shown in [58, 61, 62, 63, 227, 228], this conclusion remains valid even for strongly reduced n3P2 gaps, as cooling remains too fast due to the very efficient PBF process of this channel, and the luminosity of old ($\approx 10^6$yr) NSs cannot be reproduced. Thus less persistent n3P2 pairing could only be compatible with current cooling data if the n3P2 gap only existed at very high density ($\gtrsim 0.5\,\mathrm{fm}^3$ in the case of the V18 EOS) and would not affect medium-mass NSs. This would be very difficult to justify theoretically, indeed. The same conclusions were drawn by [51, 56, 62, 63, 227, 228] and other authors.

In order to better understand the too fast cooling provided by the n3P2 gap, we show in Fig. 5.12 the decomposition of the total luminosity into its various contributions for 'normal' ($M = 1.4\,M_\odot$, upper panels) and heavy ($M = 2.0\,M_\odot$, lower panels) hybrid NSs with the FCM. The core temperature is also displayed for better understanding. The main observations are:
- For normal stars (no quark matter), the eventual n3P2 PBF reaction is the dominant cooling process in panel (b) due to the fact that the core temperature remains of the order of the n3P2 critical temperature for most of the cooling history. This leads to too cold old NSs compared to the available data (see Fig. 5.11). The NDU process is completely blocked by the p1S0 gap that extends throughout the whole star in this case, and even more by the eventual additional n3P2 gap in (b). This keeps the core temperature sufficiently high to obtain warm old NSs in agreement with the data in the first panel (a). The additional n3P2 gap also suppresses the NBS (nn) reaction in (b) compared to (a), see also Fig. 5.10. This causes the cooling process in (b) at a later stage to be dominated by crust neutrino emission, which otherwise does not provide important contributions.

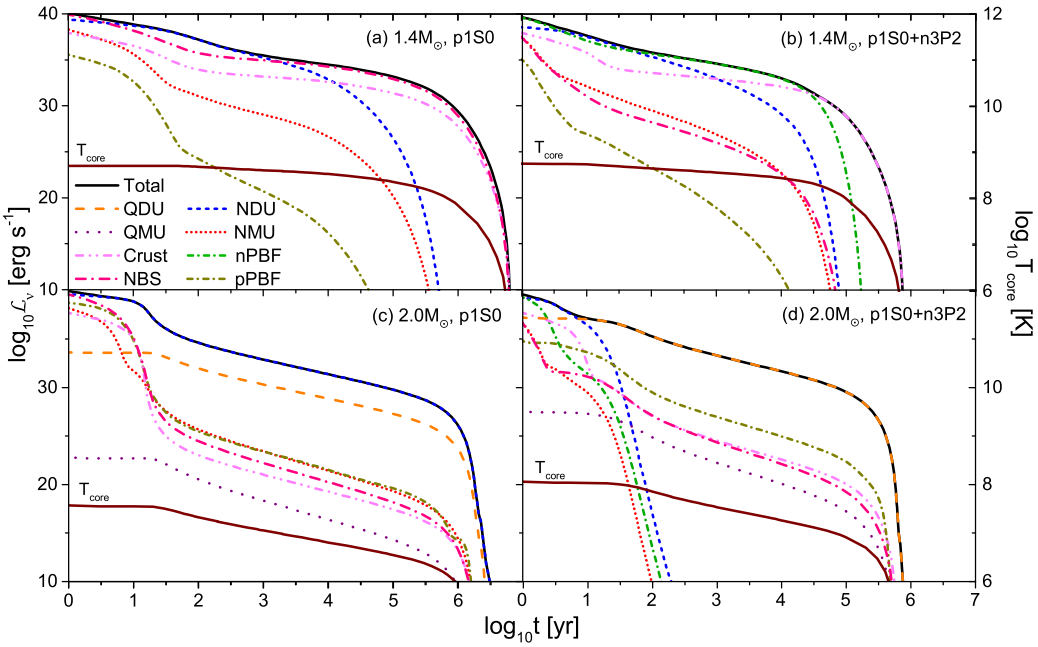

Figure 5.12: Contributions of the various cooling processes to the total luminosity as a function of time for $M = 1.4\,M_\odot$ and $2.0\,M_\odot$ NSs with the FCM EOS. Results with/out effects of the n3P2 gaps are compared. The core temperature is also shown (rhs scale). From Ref. [241].

- For heavy NSs, the NDU process is unblocked and dominant in the mixed phase when only p1S0 pairing is present in (c), but becomes completely blocked by the additional n3P2 gap in (d), see also Fig. 5.10. The strong QDU reaction is also active in both cases and dominant in (d) at any time. Therefore the PBF reactions are not decisive here and cannot compensate for the blocking of the NDU by the n3P2 gap. All this leads to much lower core temperatures compared to (a,b), but warmer stars when including the n3P2 gap and associated blocking of NDU (d) than not (c).

Conclusions

Motivated by the recent availability of experimental and observational constraints, in particular the novel constraints on the tidal deformability imposed by GW170817, we analysed the predictions of some compatible microscopic BHF EOSs and two quark-matter EOSs for the properties of NSs. Regarding the microscopic BHF EOSs, we also discussed the constraints obtained from the nuclear matter properties at saturation density. We would like to emphasize that these are not phenomenological EOSs, but they have been constructed in a microscopic way from nuclear two-body potentials and compatible three-body forces. The last issue imposed in fact strong conditions on their construction, due to which reason a perfect reproduction of all current constraints is not achieved, but was also not attempted. We stress in particular that the predicted maximum mass values $\approx 2.3\ M_\odot$ could be close to the 'true' maximum mass conjectured from the GW170817 event. The new astrophysical constraints on maximum mass and tidal deformability exclude several models with too small maximum mass and the DBHF EOS with a too large deformability. Tightening the lower limit on $\Lambda_{1.4}$ could potentially exclude several other EOSs in the future.

We concluded that among the BHF models analyzed here, the V18 and N93 could be good candidates for a realistic description of the nuclear EOS up to very high density. They satisfied nearly all current experimental and observational constraints discussed in this work. However, no novel conclusions can be drawn regarding quark matter EOSs, because similar properties of hadronic stars and hybrid stars are obtained

from the considered EOSs. As already mentioned, in this work we disregard hyperonic EOSs. If a hyperonic EOS is realistic, those constraints from NSs shall be invalid to our EOSs including only nuclear and quark matter. However, the realistic EOS remains unknown due to the theoretical uncertainties discussed in Sec. 1.4. The presence of hyperons could be suppressed or postponed by certain mechanisms, for example, by a repulsive hyperonic three-body force or an early onset of quark matter. Ultimately, to solve those uncertainties, one should rely on future observational constraints.

Furthermore, we predicted the radius of a $1.4\,M_\odot$ NS to be $11.6 \lesssim R_{1.5} \lesssim 12.9$ km with the condition of $72 \lesssim \tilde{\Lambda}_{1.4} \lesssim 720$ in the one-family scenario. This is larger than the radius measurement of accreting NS in quiescent LMXBs. This inconsistency, however, can be solved in the two-families or twin-stars scenarios. A correlation between the radius or deformability of a $M = 1.4\,M_\odot$ NS and the pressure of beta-stable matter at about twice normal density for all examined EOSs was confirmed. We found weaker correlations with the speed of sound and the compressibility of beta-stable matter at that density. On the other hand, we did not find any correlations between NS deformability and properties of symmetric or neutron matter at normal density.

We also analysed the results of the same microscopic BHF EOSs for the cooling properties of isolated NSs. All EOSs feature strong DU cooling for a wide range of masses and the presence of superfluidity is required for realistic cooling scenarios. We find that assuming absence of n3P2 pairing and employing n1S0 and p1S0 BCS gaps with possible rather generous scaling factors, a reproduction of all current cooling data for isolated NSs can be achieved with any of the proposed EOSs. A naive and straightforward analysis of the deduced NS mass distribution would exclude only the stiffest BOB EOS, which also predicts a fairly (too) large maximum mass.

We also studied the cooling of hybrid NSs, combining a realistic microscopic BHF model for the nucleonic EOS with different quark models, joined by a Gibbs phase transition. The large maximum mass of the nucleonic model is lowered to a common value of $2.1\,M_\odot$ in all hybrid scenarios, which could be close to the 'true' value. The nucleonic DU cooling process is active in all stars, but blocked by BCS p1S0 pairing

up to the onset of the quark phase. Therefore only very heavy hybrid stars, typically $M \gtrsim 1.9\,M_\odot$, exhibit rapid quark DU cooling, while reasonable smooth NS mass distributions in agreement with current data are predicted by the effect of nucleonic cooling solely.

An important conclusion can be drawn regarding n3P2 superfluidity: In all possible scenarios with and without quark matter, its presence leads to too rapid cooling of all NSs, such that the high luminosity of all currently observed old ($t \gtrsim 10^5$ yrs) stars cannot be reproduced. This seems to be a robust result of all models involving nucleonic DU cooling and confirms conclusions reached by several previous investigations within various theoretical models with and without DU cooling. This conclusion is also very unlikely to be changed by the effects of quark pairing that was disregarded here.

We have only studied a very limited set of quark-matter EOSs here, but in general it seems difficult to reconcile an early onset of quark matter with a not too large reduction of the maximum mass of the nucleonic EOS. This was confirmed by the extreme DS1.0 model we studied. Therefore only heavy NSs could be hybrid stars, and we thus expect our results to be robust with respect to changes of the quark model. In this case it would be difficult to confirm or not the appearance of quark matter in NSs from the cooling data, since the cooling pattern would the same as for pure NSs except for rare high-mass stars.

There are still various other factors that could affect the cooling scenario. So far, we only focused on unpaired quark matter and disregarded possible quark superconductivity and the size of associated gaps. Large quark gaps would suppresses the quark DU process and make quark matter 'invisible.' In our current scenario this would only affect very heavy NSs, as long as the quark matter EOS is not also strongly modified by the quark gaps. In addition, the appearance of hyperons in NSs which we disregarded in this work could also affect the cooling scenario. Hyperons, apart from strongly modifying the EOS, provide a new fast neutrino process called hyperon DU (e.g., $\Lambda \to p + e^- + \bar{\nu}_e$), which leads to a fast cooling. This could completely change the cooling diagrams. However, hyperonic pairing gaps are currently unknown. These possibilities will be studied in the future.

The combined and consistent analysis of different aspects of NS physics

will allow in the future a more and more accurate derivation of the nuclear EOS and its constraints. The simultaneous measurement of mass and radius of a NS, more accurate results of the tidal deformability, or any information on very faint objects of any age would be most valuable for such theoretical progress.

Bibliography

[1] P. Haensel, A. Y. Potekhin, and D. G. Yakovlev, *Neutron stars 1: Equation of state and structure* (Springer, New York, USA, 2007), Vol. 326.

[2] D. G. Yakovlev, A. D. Kaminker, O. Y. Gnedin, and P. Haensel, Phys. Rep. **354**, 1 (2001).

[3] B. P. Abbott et al., Phys. Rev. Lett. **119**, 161101 (2017).

[4] B. P. Abbott et al., Phys. Rev. Lett. **121**, 161101 (2018).

[5] B. P. Abbott et al., Phys. Rev. X **9**, 011001 (2019).

[6] LIGO/Virgo, O3 Public Alerts available at https://gracedb.ligo.org/superevents/public/O3/.

[7] L. Ferrario and D. Wickramasinghe, MNRAS **367**, 1323 (2006).

[8] Ren-Yu Hu and Yu-Qing Lou, MNRAS **396**, 878 (2009).

[9] F. Weber, Prog. Part. Nucl. Phys **54**, 193 (2005).

[10] W. C. G. Ho and C. O. Heinke, Nature **462**, 71 (2009).

[11] M. Servillat, C. O. Heinke, W. C. G. Ho, J. E. Grindlay, J. Hong, M. van den Berg, and S. Bogdanov, MNRAS **423**, 1556 (2012).

[12] S. Guillot, M. Servillat, N. A. Webb, and R. E. Rutledge, Astrophys. J. **772**, 7 (2013).

[13] S. Guillot and R. E. Rutledge, Astrophys. J. Lett. **796**, L3 (2014).

[14] S. Guillot, Mem. S. A. It. **87**, 521 (2016).

[15] F. Özel and P. Freire, Ann. Rev. Astron. Astrophys. **54**, 401 (2016).

[16] G. Baym, C. Pethick, and P. Sutherland, ApJ **170**, 299 (1971).

[17] X.-R. Zhou, H.-J. Schulze, E.-G. Zhao, F. Pan, and J. P. Draayer, Phys. Rev. C **70**, 048802 (2004).

[18] K. P. Levenfish and D. G. Yakovlev, Astron. Rep. **38**, 247 (1994).

[19] D. Blaschke and N. Chamel, in *The Physics and Astrophysics of Neutron Stars*, edited by L. Rezzolla, P. Pizzochero, D. I. Jones, N. Rea, and I. Vidaña (Springer International Publishing, Cham, 2018), pp. 337–400.

[20] D. G. Yakovlev, O. Y. Gnedin, M. E. Gusakov, A. D. Kaminker, K. P. Levenfish, and A. Y. Potekhin, Nucl. Phys. A **752**, 590 (2005).

[21] D. Page, U. Geppert, and F. Weber, Nucl. Phys. A **777**, 497 (2006).

[22] I. Bombaci, JPS Conf. Proc. **17**, 101002 (2017).

[23] T. A. Rijken and H.-J. Schulze, Eur. Phys. J. A **52**, 21 (2016).

[24] Z. H. Li, U. Lombardo, H.-J. Schulze, and W. Zuo, Phys. Rev. C **77**, 034316 (2008).

[25] Y. Yamamoto, T. Furumoto, N. Yasutake, and TH. A. Rijken, Phys. Rev. C **88**, 022801 (2013).

[26] Y. Yamamoto, T. Furumoto, N. Yasutake, and Th. A. Rijken, Phys. Rev. C **90**, 045805 (2014).

[27] Y. Yamamoto, T. Furumoto, N. Yasutake, and Th.A. Rijken, Eur. Phys. J. A **52**, 19 (2016).

[28] Y. Yamamoto, H. Togashi, T. Tamagawa, T. Furumoto, N. Yasutake, and Th. A. Rijken, Phys. Rev. C **96**, 065804 (2017).

[29] S. Weissenborn, D. Chatterjee, and J. Schaffner-Bielich, Phys. Rev. C **85**, 065802 (2012).

[30] M. Fortin, J. L. Zdunik, P. Haensel, and M. Bejger, Astron. Astrophys. **576**, A68 (2015).

[31] J. N. Bahcall and R. A. Wolf, Phys. Rev. **140**, B1445 (1965).

[32] D.B. Kaplan and A.E. Nelson, Phys. Lett. B **175**, 57 (1986).

[33] C. J. Pethick, T. Schaefer, and A. Schwenk, arXiv:1507.05839 (2015).

[34] F. Weber, G. A. Contrera, M. G. Orsaria, W. Spinella, and O. Zubairi, Mod. Phys. Lett. A **29**, 1430022 (2014).

[35] S. Plumari, G. F. Burgio, V. Greco, and D. Zappalà, Phys. Rev. **D88**, 083005 (2013).

[36] H. Chen, M. Baldo, G. F. Burgio, and H.-J. Schulze, Phys. Rev. D **84**, 105023 (2011).

[37] H. Chen, J.-B. Wei, M. Baldo, G. F. Burgio, and H.-J. Schulze, Phys. Rev. D **91**, 105002 (2015).

[38] F. Özel, Nature **441**, 1115 (2006).

[39] M. Alford, D. Blaschke, A. Drago, T. Klähn, G. Pagliara, and J. Schaffner-Bielich, Nature **445**, E7 (2007).

[40] E. Annala, T. Gorda, A. Kurkela, J. Nättilä, and A. Vuorinen, Nat. Phys. **16**, 907 (2020).

[41] G. F. Burgio, M. Baldo, P. K. Sahu, and H.-J. Schulze, Phys. Rev. C **66**, 025802 (2002).

[42] M. Shahrbaf, D. Blaschke, A. G. Grunfeld, and H. R. Moshfegh, Phys. Rev. C **101**, 025807 (2020).

[43] M. Shahrbaf, D. Blaschke, and S. Khanmohamadi, J. Phys. G **47**, 115201 (2020).

[44] L. Bonanno and A. Sedrakian, Astron. Astrophys. **539**, A16 (2012).

[45] E. Witten, Phys. Rev. D **30**, 272 (1984).

[46] T. Gold, Nature **218**, 731 (1968).

[47] The Australia Telescope National Facility Pulsar Catalog https://www.atnf.csiro.au/research/pulsar/psrcat/.

[48] R. D. Mellinger, F. Weber, W. Spinella, G. A. Contrera, and M. G. Orsaria, Universe **3**, 5 (2017).

[49] J. W.T. Hessels, S. M. Ransom, I. H. Stairs, P. C. C. Freire, V. M. Kaspi, and F. Camilo, Science **311**, 1901 (2006).

[50] P. Kaaret, Z. Prieskorn, J. J. M. in 't Zand, S. Brandt, N. Lund, S. Mereghetti, D. Gotz, E. Kuulkers, and J. A. Tomsick, Astrophys. J. Lett. **657**, L97 (2007).

[51] M. V. Beznogov and D. G. Yakovlev, MNRAS **447**, 1598 (2015).

[52] S. Beloin, S. Han, A. W. Steiner, and D. Page, Phys. Rev. C **97**, 015804 (2018).

[53] A. Y. Potekhin, D. A. Zyuzin, D. G. Yakovlev, M. V. Beznogov, and Y. A. Shibanov, MNRAS **496**, 5052 (2020).

[54] R. N. Manchester, in *Neutron Stars and Pulsars*, edited by W. Becker (Springer, Berlin, Heidelberg, 2009), pp. 19–39.

[55] D. Page, J. M. Lattimer, M. Prakash, and A. W. Steiner, Astrophys. J. Supplement Series **155**, 623 (2004).

[56] M. V. Beznogov and D. G. Yakovlev, MNRAS **452**, 540 (2015).

[57] M. V. Beznogov, E. Rrapaj, D. Page, and S. Reddy, Phys. Rev. C **98**, 035802 (2018).

[58] M. Fortin, G. Taranto, G. F. Burgio, P. Haensel, H.-J. Schulze, and J. L. Zdunik, MNRAS **475**, 5010 (2018).

[59] C. O. Heinke and W. C. G. Ho, Astrophys. J. **719**, L167 (2010).

[60] M.J.P. Wijngaarden et al., MNRAS **484**, 974 (2019).

[61] G. Taranto, G. F. Burgio, and H.-J. Schulze, MNRAS **456**, 1451 (2016).

[62] D. Blaschke, H. Grigorian, D. N. Voskresensky, and F. Weber, Phys. Rev. C **85**, 022802 (2012).

[63] D. Blaschke, H. Grigorian, and D. N. Voskresensky, Phys. Rev. C **88**, 065805 (2013).

[64] A. Sedrakian, Astron. Astrophys **555**, L10 (2013).

[65] A. Sedrakian, European Physical Journal A **52**, 44 (2016).

[66] B. Posselt, G. G. Pavlov, V. Suleimanov, and O. Kargaltsev, Astrophys. J. **779**, 186 (2013).

[67] B. Posselt and G. G. Pavlov, Astrophys. J. **864**, 135 (2018).

[68] M. V. Beznogov, M. Fortin, P. Haensel, D. G. Yakovlev, and J. L. Zdunik, MNRAS **463**, 1307 (2016).

[69] D. Page, M. V. Beznogov, I. Garibay, J. M. Lattimer, M. Prakash, and H. T. Janka, Astrophys. J. **898**, 125 (2020).

[70] J. M. Lattimer, Universe **5**, 159 (2019).

[71] H. T. Haniewicz et al., arXiv:2007.07565 (2020).

[72] S. E. Thorsett and D. Chakrabarty, Astrophys. J. **512**, 288 (1999).

[73] P. B. Demorest, T. Pennucci, S. M. Ransom, M. S. Roberts, and J. W. Hessels, Nature **467**, 1081 (2010).

[74] H. T. Cromartie et al., Nature Astron. **4**, 72 (2019).

[75] J. Antoniadis et al., Science **340**, 448 (2013).

[76] P. C. C. Freire, S. M. Ransom, S. Bégin, I. H. Stairs, J. W. T. Hessels, L. H. Frey, and F. Camilo, Astrophys. J. **675**, 670 (2008).

[77] R. Abbott et al., Astrophys. J. Lett. **896**, L44 (2020).

[78] E. R. Most, L. J. Papenfort, L. R. Weih, and L. Rezzolla, arXiv:2006.14601 (2020).

[79] V. Dexheimer, R.O. Gomes, T. Klähn, S. Han, and M. Salinas, arXiv:2007.08493 (2020).

[80] N.-B. Zhang and B.-A. Li, arXiv:2007.02513 (2020).

[81] J.-B. Wei, H. Chen, G. F. Burgio, and H. J Schulze, Phys. Rev. D **96**, 043008 (2017).

[82] L. Rezzolla, E. R. Most, and L. R. Weih, Astrophys. J. **852**, L25 (2018).

[83] F. Özel, D. Psaltis, T. Güver, G. Baym, C. Heinke, and S. Guillot, Astrophys. J. **820**, 28 (2016).

[84] D. Psaltis, F. Özel, and D. Chakrabarty, Astrophys. J. **787**, 136 (2014).

[85] S. Guillot, M. Kerr, P. S. Ray, and S. Bogdanov et al., Astrophys. J. **887**, L27 (2019).

[86] M. C. Miller, F. K. Lamb, and A. J. Dittmann et al., Astrophys. J. **887**, L24 (2019).

[87] T. E. Riley, A. L. Watts, and S. Bogdanov et al., Astrophys. J. **887**, L21 (2019).

[88] B. P. Abbott et al., Phys. Rev. Lett. **119**, 161101 (2017).

[89] B. P. Abbott et al., Astrophys. J. **848**, L12 (2017).

[90] D. Radice, A. Perego, F. Zappa, and S. Bernuzzi, Astrophys. J. Lett. **852**, L29 (2018).

[91] D. Radice and L. Dai, Eur. Phys. J. A **55**, 50 (2019).

[92] M. W. Coughlin, T. Dietrich, B. Margalit, and B. D. Metzger, MNRAS **489**, L91 (2019).

[93] K. Kiuchi, K. Kyutoku, M. Shibata, and K. Taniguchi, Astrophys. J. Lett. **876**, L31 (2019).

[94] Image taken from http://theor0.jinr.ru/twiki-cgi/view/NICA.

[95] M. Oertel, M. Hempel, T. Klähn, and S. Typel, Rev. Mod. Phys. **89**, 015007 (2017).

[96] A. Chodos, R. L. Jaffe, K. Johnson, C. B. Thorn, and V. F. Weisskopf, Phys. Rev. D **9**, 3471 (1974).

[97] M. Buballa, Phys. Rep **407**, 205 (2005).

[98] Yu. A. Simonov and M. A. Trusov, Phys. Lett. B **650**, 36 (2007).

[99] Yu. A. Simonov and M. A. Trusov, JETP Lett. **85**, 598 (2007).

[100] C. D. Roberts and A. G. Williams, Prog. Part. Nucl. Phys. **45**, (2000).

[101] M. Baldo, in *The Many-Body Theory of the Nuclear Equation of State* (World Scientific, Singapore, 1999), Vol. 8, pp. 1–120.

[102] R. B. Wiringa, V.G.J. Stoks, and R. Schiavilla, Phys. Rev. C **51**, 38 (1995).

[103] M. Baldo, I. Bombaci, and G. F. Burgio, Astron. Astrophys **328**, 274 (1997).

[104] Z. H. Li and H.-J. Schulze, Phys. Rev. C **78**, 028801 (2008).

[105] J.-B. Wei, J.-J. Lu, G. F. Burgio, Z. H. Li, and H.-J Schulze, Eur. Phys. J. A **56**, 63 (2020).

[106] M. Baldo, G. F. Burgio, P. Castorina, S. Plumari, and D. Zappalà, Phys. Rev. D **78**, 063009 (2008).

[107] I. Bombaci and D. Logoteta, MNRAS **433**, L79 (2013).

[108] M. G. Alford, G. F. Burgio, S. Han, G. Taranto, and D. Zappalà, Phys. Rev. D **92**, 083002 (2015).

[109] G. F. Burgio and D. Zappalà, Eur. Phys. J. A **52**, 60 (2016).

[110] A. Di Giacomo, H. G. Dosch, V. I. Shevchenko, and Yu. A. Simonov, Phys. Rept. **372**, 319 (2002).

[111] A. V. Nefediev, Yu. A. Simonov, and M. A. Trusov, Int. J. Mod. Phys. E **18**, 549 (2009).

[112] M. D'Elia, A. Di Giacomo, and E. Meggiolaro, Phys. Lett. B **408**, 315 (1997).

[113] M. D'Elia, A. Di Giacomo, and E. Meggiolaro, Phys. Rev. D **67**, 114504 (2003).

[114] R. Alkofer, P. Watson, and H. Weigel, Phys. Rev. D **65**, 094026 (2002).

[115] L. Chang and C. D. Roberts, Phys. Rev. Lett. **103**, 081601 (2009).

[116] H. Chen, J.-B. Wei, and H.-J. Schulze, Eur. Phys. J. A **52**, 291 (2016).

[117] G. Baym, T. Hatsuda, T. Kojo, P. D. Powell, Y.-F Song, and T. Takatsuka, Rept. Prog. Phys. **81**, 056902 (2018).

[118] K. Masuda, T. Hatsuda, and T. Takatsuka, Astrophys. J. **764**, 12 (2013).

[119] T. Kojo, P. D. Powell, Y.-F. Song, and G. Baym, Phys. Rev. D **91**, 045003 (2015).

[120] T. Kojo, Eur. Phys. J. A **52**, 51 (2016).

[121] T. Kojo, Universe **4**, 42 (2018).

[122] H. Heiselberg, C. J. Pethick, and E. F. Staubo, Phys. Rev. Lett. **70**, 1355 (1993).

[123] N. Yasutake, T. Maruyama, and T. Tatsumi, Phys. Rev. D **80**, 123009 (2009).

[124] X. H. Wu and H. Shen, Phys. Rev. C **96**, 025802 (2017).

[125] V. Abgaryan, D. Alvarez-Castillo, A. Ayriyan, D. Blaschke, and H. Grigorian, Universe **4**, 94 (2018).

[126] K. Maslov, N. Yasutake, D. Blaschke, A. Ayriyan, H. Grigorian, T. Maruyama, T. Tatsumi, and D. N. Voskresensky, Phys. Rev. C **100**, 025802 (2019).

[127] N. K. Glendenning, *Compact stars nuclear physics particle physics and general relativity* (Springer, New York, USA, 2000), Vol. 242.

[128] R. Machleidt, K. Holinde, and C. Elster, Phys. Rept. **149**, 1 (1987).

[129] R. Machleidt, Adv. Nucl. Phys. **19**, 189 (1989).

[130] M. M. Nagels, T. A. Rijken, and J. J. de Swart, Phys. Rev. D **17**, 768 (1978).

[131] V. G. J. Stoks, R. A. M. Klomp, C. P. F. Terheggen, and J. J. de Swart, Phys. Rev. C **49**, 2950 (1994).

[132] P. Grangé, A. Lejeune, M. Martzolff, and J.-F. Mathiot, Phys. Rev. C **40**, 1040 (1989).

[133] W. Zuo, A. Lejeune, U. Lombardo, and J. F. Mathiot, Eur. Phys. J. A **14**, 469 (2002).

[134] Z. H. Li, U. Lombardo, H.-J. Schulze, and W. Zuo, Phys. Rev. C **77**, 034316 (2008).

[135] B. S. Pudliner, V. R. Pandharipande, J. Carlson, and R. B. Wiringa, Phys. Rev. Lett. **74**, 4396 (1995).

[136] B. S. Pudliner, V. R. Pandharipande, J. Carlson, S. C. Pieper, and R. B. Wiringa, Phys. Rev. C **56**, 1720 (1997).

[137] M. Baldo, I. Bombaci, and G. F. Burgio, Astron. Astrophys. **328**, 274 (1997).

[138] G. Taranto, M. Baldo, and G. F. Burgio, Phys. Rev. C **87**, 045803 (2013).

[139] T. Hinderer, Astrophys. J. **677**, 1216 (2008).

[140] T. Hinderer, Astrophys. J. **697**, 964 (2009).

[141] T. Hinderer, B. D. Lackey, R. N. Lang, and J. S. Read, Phys. Rev. D **81**, 123016 (2010).

[142] J. M. Lattimer and M. Prakash, Phys. Rept. **442**, 109 (2007).

[143] A. Bauswein, O. Just, H.-T. Janka, and N. Stergioulas, Astrophys. J. **850**, L34 (2017).

[144] E. Annala, T. Gorda, A. Kurkela, and A. Vuorinen, Phys. Rev. Lett. **120**, 172703 (2018).

[145] J.-B. Wei, A. Figura, G. F. Burgio, H. Chen, and H.-J. Schulze, J. Phys. G **46**, 034001 (2019).

[146] A. Li, X. R. Zhou, G. F. Burgio, and H.-J. Schulze, Phys. Rev. C **81**, 025806 (2010).

[147] A. Akmal, V. R. Pandharipande, and D. G. Ravenhall, Phys. Rev. C **58**, 1804 (1998).

[148] T. Gross-Boelting, C. Fuchs, and A. Faessler, Nucl. Phys. A **648**, 105 (1999).

[149] J. M. Lattimer and F. Douglas Swesty, Nucl. Phys. A **535**, 331 (1991).

[150] A. W. Steiner, M. Hempel, and T. Fischer, Astrophys. J. **774**, 17 (2013).

[151] R. Brockmann and R. Machleidt, Phys. Rev. C **42**, 1965 (1990).

[152] G. Q. Li, R. Machleidt, and R. Brockmann, Phys. Rev. C **45**, 2782 (1992).

[153] J. Morales, V. R. Pandharipande, and D. G. Ravenhall, Phys. Rev. C **66**, 054308 (2002).

[154] H.-J. Schulze, A. Polls, A. Ramos, and I. Vidaña, Phys. Rev. C **73**, 058801 (2006).

[155] H.-J. Schulze and T. Rijken, Phys. Rev. C **84**, 035801 (2011).

[156] H. Chen, M. Baldo, G. F. Burgio, and H.-J. Schulze, Phys. Rev. D **86**, 045006 (2012).

[157] E. Fonseca et al., Astrophys. J. **832**, 167 (2016).

[158] J. Antoniadis et al., Science **340**, 6131 (2013).

[159] M. Shibata, S. Fujibayashi, K. Hotokezaka, K. Kiuchi, K. Kyutoku, Y. Sekiguchi, and M. Tanaka, Phys. Rev. D **96**, 123012 (2017).

[160] B. Margalit and B. D. Metzger, Astrophys. J. **850**, L19 (2017).

[161] E. R. Most, L. R. Weih, L. Rezzolla, and J. Schaffner-Bielich, Phys. Rev. Lett. **120**, 261103 (2018).

[162] Y. Lim and J. W. Holt, Phys. Rev. Lett. **121**, 062701 (2018).

[163] F. J. Fattoyev, J. Piekarewicz, and C. J. Horowitz, Phys. Rev. Lett. **120**, 172702 (2018).

[164] S. Abrahamyan et al., Phys. Rev. Lett. **108**, 112502 (2012).

[165] E. Pian et al., Nature **551**, 67 (2017).

[166] D. A. Coulter et al., Science **358**, 1556 (2017).

[167] P. S. Cowperthwaite et al., Astrophys. J. **848**, L17 (2017).

[168] M. Nicholl et al., Astrophys. J. **848**, L18 (2017).

[169] K. D. Alexander et al., Astrophys. J. **848**, L21 (2017).

[170] J. M. Lattimer and M. Prakash, Astrophys. J. **550**, 426 (2001).

[171] A. W. Steiner, J. M. Lattimer, and E. F. Brown, Astrophys. J. **722**, 33 (2010).

[172] A. W. Steiner, J. M. Lattimer, and E. F. Brown, Astrophys. J. Lett. **765**, L5 (2013).

[173] A. W. Steiner, C. O. Heinke, S. Bogdanov, C. K. Li, W. C. G. Ho, A. Bahramian, and S. Han, MNRAS **476**, 421 (2018).

[174] A. Drago, A. Lavagno, G. Pagliara, and D. Pigato, Phys. Rev. C **90**, 065809 (2014).

[175] S. Weissenborn, I. Sagert, G. Pagliara, M. Hempel, and J. Schaffner-Bielich, Astrophys. J. **740**, L14 (2011).

[176] G. F. Burgio, A. Drago, G. Pagliara, H.-J. Schulze, and J.-B. Wei, Astrophys. J. **860**, 139 (2018).

[177] A. Drago, A. Lavagno, and G. Pagliara, Phys. Rev. D **89**, 043014 (2014).

[178] A. Drago, A. Lavagno, G. Pagliara, and D. Pigato, Eur. Phys. J. A **52**, 40 (2016).

[179] A. Drago and G. Pagliara, Eur. Phys. J. A **52**, 41 (2016).

[180] G. Wiktorowicz, A. Drago, G. Pagliara, and S. B. Popov, Astrophys. J. **846**, 163 (2017).

[181] I. Tews, J. M. Lattimer, A. Ohnishi, and E. E. Kolomeitsev, Astrophys. J. **848**, 105 (2017).

[182] N.-B. Zhang, B.-J. Cai, B.-A. Li, William G. Newton, and J. Xu, Nucl. Sci. Tech. **28**, 181 (2017).

[183] J. Margueron, R. Hoffmann Casali, and F. Gulminelli, Phys. Rev. C **97**, 025805 (2018).

[184] S. Shlomo, V. M. Kolomietz, and G. Colò, Eur. Phys. J. A **30**, 23 (2006).

[185] J. Piekarewicz, J. Phys. G **37**, 064038 (2010).

[186] B.-A. Li and X. Han, Phys. Lett. B **727**, 276 (2013).

[187] M. B. Tsang et al., Phys. Rev. C **86**, 015803 (2012).

[188] J. M. Lattimer and Y. Lim, Astrophys. J. **771**, 51 (2013).

[189] J. M. Lattimer and A. W. Steiner, Eur. Phys. J. A **50**, 40 (2014).

[190] M. B. Tsang et al., Phys. Rev. Lett. **102**, 122701 (2009).

[191] X. Roca-Maza et al., Phys. Rev. C **92**, 064304 (2015).

[192] L.-W. Chen, C. M. Ko, B.-A. Li, and J. Xu, Phys. Rev. C **82**, 024321 (2010).

[193] P. Möller, W. D. Myers, H. Sagawa, and S. Yoshida, Phys. Rev. Lett. **108**, 052501 (2012).

[194] P. Danielewicz and J. Lee, Nucl. Phys. A **922**, 1 (2014).

[195] A. W. Steiner, J. M. Lattimer, and E. F. Brown, Astrophys. J. Lett. **765**, L5 (2013).

[196] P. Russotto et al., Phys. Rev. C **94**, 034608 (2016).

[197] P. Russotto et al., Phys. Lett. B **697**, 471 (2011).

[198] D. Miśkowiec, Phys. Rev. Lett. **72**, 3650 (1994).

[199] P. Danielewicz, R. Lacey, and W. G. Lynch, Science **298**, 1592 (2002).

[200] C. Y. Tsang, M. B. Tsang, P. Danielewicz, W. G. Lynch, and F. J. Fattoyev, arXiv:1901.07673 (2019).

[201] J. L. Ritman et al., Z. Phys. A **352**, 355 (1995).

[202] N.-B. Zhang and B.-A. Li, Astrophys. J. **879**, 99 (2019).

[203] C. Y. Tsang, M. B. Tsang, P. Danielewicz, W. G. Lynch, and F. J. Fattoyev, arXiv:1807.06571 (2018).

[204] J. M. Lattimer and M. Prakash, Phys. Rept. **333**, 121 (2000).

[205] N.-B. Zhang and B.-A. Li, Eur. Phys. J. A **55**, 39 (2019).

[206] F. J. Fattoyev, J. Carvajal, W. G. Newton, and B.-A. Li, Phys. Rev. C **87**, 015806 (2013).

[207] T. Malik et al., Phys. Rev. C **98**, 035804 (2018).

[208] L. Perot, N. Chamel, and A. Sourie, Phys. Rev. C **100**, 035801 (2019).

[209] C. Y. Tsang et al., Phys. Lett. B **796**, 1 (2019).

[210] D. Page, NSCool code available at http://www.astroscu.unam.mx/neutrones/NSCool, 2010.

[211] M. Baldo, G. F. Burgio, H.-J. Schulze, and G. Taranto, Phys. Rev. C **89**, 048801 (2014).

[212] N. Iwamoto, Ann. Phys. **141**, 1 (1982).

[213] J. M. Lattimer, C. J. Pethick, M. Prakash, and P. Haensel, Phys. Rev. Lett. **66**, 2701 (1991).

[214] R. C. Duncan, S. L. Shapiro, and I. Wasserman, Astrophys. J. **267**, 358 (1983).

[215] J.-B. Wei, G. F. Burgio, and H.-J. Schulze, MNRAS **484**, 5162 (2019).

[216] E. Fonseca et al., Astrophys. J. **832**, 167 (2016).

[217] L. Amundsen and E. Østgaard, Nucl. Phys. A **442**, 163 (1985).

[218] M. Baldo, J. Cugnon, A. Lejeune, and U. Lombardo, Nucl. Phys. A **536**, 349 (1992).

[219] T. Takatsuka and R. Tamagaki, Prog. Theor. Phys. Suppl. **112**, 27 (1993).

[220] Ø. Elgarøy, L. Engvik, M. Hjorth-Jensen, and E. Osnes, Nucl. Phys. A **607**, 425 (1996).

[221] V. A. Khodel, V. V. Khodel, and J. W. Clark, Phys. Rev. Lett. **81**, 3828 (1998).

[222] M. Baldo, Ø. Elgarøy, L. Engvik, M. Hjorth-Jensen, and H.-J. Schulze, Phys. Rev. C **58**, 1921 (1998).

[223] M. Baldo and H.-J. Schulze, Phys. Rev. C **75**, 025802 (2007).

[224] D. Page, M. Prakash, J. M. Lattimer, and A. W. Steiner, Phys. Rev. Lett. **106**, 081101 (2011).

[225] P. S. Shternin, D. G. Yakovlev, C. O. Heinke, W. C. G. Ho, and D. J. Patnaude, MNRAS **412**, L108 (2011).

[226] D. G. Yakovlev, W. C. G. Ho, P. S. Shternin, C. O. Heinke, and A. Y. Potekhin, MNRAS **411**, 1977 (2011).

[227] H. Grigorian and D. N. Voskresensky, Astron. Astrophys. **444**, 913 (2005).

[228] D. Blaschke, H. Grigorian, and D.N. Voskresensky, Astron. Astrophys. **424**, 979 (2004).

[229] D. N. Voskresensky and A. V. Senatorov, Sov. Phys. JETP Lett. **63**, 885 (1986).

[230] E. E. Kolomeitsev and D. N. Voskresensky, Phys. Rev. C **77**, 065808 (2008).

[231] H. Grigorian, D.N. Voskresensky, and D. Blaschke, Eur. Phys. J. A **52**, 67 (2016).

[232] J. Antoniadis, T. M. Tauris, F. Ozel, E. Barr, D. J. Champion, and P. C. C. Freire, arXiv:1605.01665 (2016).

[233] J. Alsing, H. O. Silva, and E. Berti, MNRAS **478**, 1377 (2018).

[234] D. Blaschke and H. Grigorian, Prog. Part. Nucl. Phys. **59**, 139 (2007).

[235] H. Grigorian, Phys. Part. Nucl. **39**, 1143 (2008).

[236] S. Popov, H. Grigorian, R. Turolla, and David Blaschke, Astron. Astrophys. **448**, 327 (2006).

[237] S. B. Popov, H. Grigorian, and D. Blaschke, Phys. Rev. C **74**, 025803 (2006).

[238] F. Özel, D. Psaltis, R. Narayan, and A. Santos Villarreal, Astrophys. J. **757**, 55 (2012).

[239] B. Kiziltan, A. Kottas, M. De Yoreo, and S. E. Thorsett, Astrophys. J. **778**, 66 (2013).

[240] J.-B. Wei, F. Burgio, and H.-J. Schulze, Universe **6**, 115 (2020).

[241] J.-B. Wei, G. F. Burgio, H.-J. Schulze, and D. Zappalà, MNRAS **498**, 344 (2020).

[242] D. Page, M. Prakash, J. M. Lattimer, and A. W. Steiner, Phys. Rev. Lett. **85**, 2048 (2000).

[243] S. M. de Carvalho, R. Negreiros, M. Orsaria, G. A. Contrera, F. Weber, and W. Spinella, Phys. Rev. C **92**, 035810 (2015).

Acknowledgements

Taking this opportunity, I would like to express sincere gratitude to my scientific supervisors, Dr. Burgio and Dr. Schulze, for their enlightening guidance and constant encouragement. With their help, I could attend and present my works in the conferences and seminars. I would not have been able to complete my PhD without them.

Secondly, I would like to thank internal supervisor, Prof. Greco, and my master supervisor, Prof. Chen, who help me got this opportunity to study in Catania. I am also very grateful to teachers and students of the physics department, in particular my friend Antonio Figura for the constant help in the PhD courses and others.

Finally, I would like to thank China Scholarship Council for the financial support (CSC No. 201706410092).